

Tensor network methods for quantum lattice systems

Von der QUEST-Leibniz-Forschungsschule der
GOTTFRIED WILHELM LEIBNIZ UNIVERSITÄT
HANNOVER

zur Erlangung des Grades

DOKTOR DER NATURWISSENSCHAFTEN
Dr. rer. nat.

genehmigte Dissertation

von

M.SC. ASHLEY MILSTED
geboren am 14.12.1985, in High Wycombe, England.

2016

REFERENT: Prof. Ph.D. Tobias J. Osborne,
Institut für Theoretische Physik, Leibniz Universität Hannover

KOREFERENT: P.D. Dr. rer. nat. Carsten Klempt,
Institut für Quantenoptik, Leibniz Universität Hannover

KOREFERENT: Prof. Dr. rer. nat. Norbert Schuch,
JARA Institut für Quanteninformation, RWTH Aachen

TAG DER PROMOTION: 09.12.2015

Acknowledgements

A doctoral thesis is the product of a single author. While this is true insofar as the thesis document was written and structured under command of a single human brain, it is unusual, albeit not impossible in an infinite universe, for such an organ to be found in isolation. Of the various environmental conditions conducive to the precipitation of a doctoral thesis, it is the many other people involved who are most deserving of thanks!

Within the scientific community I am most grateful to Tobias J. Osborne, whose attitude, knowledge and wisdom have inspired and guided me. Another person who strongly influenced my course over the last few years is Emilio Cobanera, with whom I had the pleasure to collaborate, together with Luis Searba, Ion Cosma Fulga, Michele Burrello and Carlo Beenakker, on two of the main results of this thesis. I would also like to thank Emilio and Carlo for having me at the Lorentz Centre in Leiden.

Equally as important as collaborators and coauthors are the many members of Reinhard Werner's Quantum Information Group at the Leibniz University of Hannover who, aside from being generally engaging and inspiring, have made the day to day process of research a pleasure. I am similarly indebted to Jutho Haegeman, Karel van Acoleyen, and the members of Frank Verstraete's group at the University of Gent, where I was fortunate enough to spend some of my time during the last three years.

Special thanks must go to those of my friends and colleagues kind enough to endure and offer their comments on early versions of parts of this thesis. In no particular order, I am grateful to Florian Richter, Kais Abdelkhalek, Tobias Geib, Leander Fiedler, Marius Lewerenz, Fabian Transchel, Lars Dammeier, Courtney Brell, and Cédric Bény.

Finally, some of the most important contributors to this work are my loving parents, Jean and Andy Milsted and my certifiably insane siblings Tom and Hat. It's good to know you're not the only one. The single most important person for me to thank, however, is Juliane — my partner in love, life, and whatever else there is out there. It was her encouragement that led me back into science, and it is her support that keeps me going in times of doubt.

Abstract

Tensor network states (TNS) are states of quantum lattice systems given by a network of parameter tensors that, when contracted, produces a state in which entanglement is limited by the dimensions of the tensors. In one-dimensional systems they have revolutionised numerical methods in the form of the density matrix renormalisation group (DMRG) and variational matrix product state (MPS) methods. In this thesis, we use MPS together with variational methods exploiting the MPS tangent space, to numerically study a selection of quantum lattice systems in one spatial dimension. Obtaining MPS ground states throughout the parameter space of the system in question, we produce approximate phase diagrams (phase diagram “sketches”) for the interacting Majorana fermion chain, which describes the edge of a weak topological insulator, as well as three instances of the anisotropic next-nearest-neighbour clock (ANNNC) model, which has a description in terms of parafermions (generalised Majorana fermions) and may be implemented in mesoscopic devices involving a fractional topological insulator. We find incommensurate floating phases and probable Berezinskii-Kosterlitz-Thouless transitions in most of these systems, with an unexpected commensurate gapless phase appearing in one of the ANNNC instances. Overall, we find that computing approximate phase diagrams in a systematic way using MPS techniques is an efficient way of characterising one-dimensional models, including their gapless phases. We also study the one-dimensional $O(N)$ quantum rotor model for the abelian case of $O(2)$, which represents a limiting case of the ANNNC model, and the nonabelian case of $O(4)$, which is known to be related to nonabelian lattice gauge theory. Indeed, we formulate the rotor model as a lattice gauge theory on a “Hawaiian earring” graph, using graph manipulation moves to relate it to gauge theories on a cylinder graph. We compare our numerical results for the mass gap and beta functions of the rotor model to known exact results for the weak-coupling regime, finding good agreement. We conclude that TNS methods can deliver accurate results in the case of continuous local degrees of freedom described by compact groups, where we employ a cutoff in terms of the Fourier modes of the group to obtain a finite effective Hilbert space. However, our results also indicate that the computational effort is likely to increase considerably as the continuum limit of such models are approached. This is not only due to increasing entanglement, but also due to the relevance of higher Fourier modes.

Keywords: Quantum lattice systems, tensor network states, nonabelian gauge theory.

Kurzzusammenfassung auf Deutsch

Tensornetzwerkzustände (TNS) sind Zustände von Quantengittersystemen, die die Form eines aus Tensoren bestehenden Netzwerks annehmen. Hierbei beschreibt das Netzwerk, wie die Tensoren miteinander kontrahiert werden müssen um einen Zustand zu ergeben. Eine besondere Eigenschaft dieser Zustände ist, dass die Verschränkung durch die Dimensionen der Tensoren nach oben begrenzt ist. In einer Raumdimension haben TNS-Methoden numerische Studien revolutioniert, vor allem in der Gestalt der Dichtematrix-renormierungsgruppe (DMRG) und verschiedener Variationsmethoden für Matrixproduktzustände (MPS). In dieser Arbeit werden MPS-Variationsmethoden verwendet, die den Tangentialraum von MPS ausnutzen, um eine Auswahl eindimensionaler Quantengittersysteme numerisch zu untersuchen. Im ersten Teil werden mithilfe von MPS-Grundzuständen aus dem Parameterraum des Modells approximierende Phasendiagramme erstellt. Untersucht wird eine Kette wechselwirkender Majorana-Fermionen, welche den Rand eines schwachen topologischen Isolators modelliert, sowie drei Varianten des anisotropischen Uhrmodells mit Übernächste-Nachbar-Wechselwirkung (ANNNC-Modell). Letzteres kann durch Parafermionen beschrieben werden und besitzt eine mesoskopische Implementierung mittels eines gebrochenzahligen topologischen Isolators. Es werden nicht-kommensurable «schwimmende» Phasen und Berezinskii-Kosterlitz-Thouless-Übergänge in den meisten Modellen entdeckt, sowie eine unerwartete kommensurable kritische Phase in einer Instanz des ANNNC-Modells. Insgesamt wird festgestellt, dass das Skizzieren von Phasendiagrammen mittels MPS-Methoden für die Charakterisierung eindimensionaler Systeme, inklusive kritischer Phasen, sehr gut geeignet ist. Im zweiten Teil wird das eindimensionale $O(N)$ -Modell untersucht; zum einen im abelschen Fall von $O(2)$, welches einen limitierenden Fall des ANNNC-Modells darstellt, und zum anderen nicht-abelschen Fall von $O(4)$, der mit der nicht-abelschen Gittereichtheorie verwandt ist. In der Tat kann das $O(4)$ -Modell als Gittereichtheorie auf einem «hawaiischen Ohrring-Graphen» identifiziert werden. Ferner kann es, mithilfe von Operationen, die den Graphen umformen, mit der Gittereichtheorie eines Zylinders in Verbindung gebracht werden. Die numerischen Ergebnisse für die Masse der ersten Anregung und die Beta-Funktion werden bei schwacher Kopplung mit bekannten exakten Ergebnissen verglichen. Dadurch wird gezeigt, dass die TNS-Methoden sogar im Fall von kompakten kontinuierlichen lokalen Freiheitsgraden akkurate Werte liefern können. Um die Dimensionen des lokalen Raums auf eine endliche Zahl zu verkleinern, erweist sich die Beschränkung der verfügbaren Fouriermoden als sinnvoll. Allerdings deuten die in dieser Arbeit vorgestellten Ergebnisse an, dass der Rechenaufwand bei solchen Modellen in der Nähe des Kontinuumslimites deutlich steigen wird — nicht nur wegen steigender Verschränkung, sondern auch aufgrund der steigenden Bedeutung von höheren Fouriermoden.

Schlagnworte: Quantengittersysteme, Tensornetzwerkzustände, nicht-abelsche Eichtheorie.

Contents

Acknowledgements	i
Abstract	iii
Kurzzusammenfassung auf Deutsch	v
Introduction	1
1 Block-uniform matrix product states	5
1.1 Introduction	5
1.2 Quantum lattice systems	6
1.2.1 Correlations and entanglement	6
1.3 Block-uniform matrix product states	8
1.3.1 Computing the norm	9
1.3.2 Fidelity per site	11
1.3.3 Gauge transformations	12
1.3.4 Canonical forms	12
1.3.5 Expectation values and correlation functions	12
1.3.6 Modulated correlations	14
1.3.7 Schmidt decomposition and half-chain entropy	14
1.3.8 Tangent space	16
1.4 Tangent space methods for MPS	18
1.4.1 The effective energy gradient	19
1.4.2 Improvements for large physical dimensions	22
1.4.3 Energy optimisation: Nonlinear conjugate gradient	22
1.4.4 Automatic adjustment of block length	25
1.4.5 Excitations	26
1.4.6 GPGPU acceleration of computations	26
2 Phases and phase transitions	27
2.1 Introduction	27
2.2 Types of phase transition	27
2.2.1 First order	28
2.2.2 Continuous phase transitions	28

2.2.3	Second-order phase transitions	30
2.2.4	Berezinskii-Kosterlitz-Thouless transitions	32
2.2.5	Incommensurate order	33
2.3	Sketching phase diagrams using MPS	34
2.3.1	Scanning lines in parameter space	34
2.3.2	Finite Entanglement Scaling (FES)	37
3	Majorana fermions and parafermions	39
3.1	Introduction	39
3.2	Systems of many identical particles	40
3.2.1	Quantum lattice systems and many-particle systems	43
3.2.2	Majorana fermions	44
3.2.3	Parafermions	44
3.3	The Ising model as a Majorana chain	45
3.3.1	Physical relevance of Majorana modes	46
3.4	The clock model and parafermions	46
3.4.1	Phases of the clock model	48
3.4.2	Parafermions in the clock model	48
4	Interacting Majorana chains: The Kitaev edge	51
4.1	Introduction	51
4.2	Interacting Kitaev edge model	52
4.2.1	Majorana fermion Hamiltonian	52
4.2.2	Spin Hamiltonian	53
4.2.3	Self-duality and symmetries of the model	54
4.3	Numerical study	54
4.3.1	Critical Ising phase	55
4.3.2	Floating phase	56
4.3.3	Gapped anti phase	56
4.3.4	Phase diagram	59
4.3.5	Strong interactions	59
4.4	Discussion and conclusions	60
5	Axial next nearest neighbour clock model	63
5.1	Introduction	63
5.2	The axial next-nearest-neighbour clock model	64
5.2.1	Incommensurate order	65
5.2.2	Dual nearest-neighbour model	65
5.2.3	Mesoscopic realisation	66
5.3	Numerical study	68
5.3.1	Methods	68
5.3.2	Phase diagrams	68
5.3.3	CFT scaling dimensions and entanglement spectra	74
5.4	Discussion and conclusions	78

6	Lattice gauge theory	81
6.1	Introduction	81
6.2	Gauge theories	81
6.3	Some group theory	84
6.3.1	Irreducible representations and the Peter-Weyl theorem	85
6.3.2	Lie algebra and generators of a Lie group	86
6.4	Bases for $L^2(G)$	86
6.5	Operators on $L^2(G)$	87
6.6	Operators in the momentum basis	89
6.7	Hamiltonian lattice gauge theory	91
6.7.1	Gauge transformations	93
6.7.2	Graph manipulation	93
6.7.3	Continuum limits and renormalisation	99
7	Lattice gauge theory on an earring and the $O(N)$ rotor model	103
7.1	Introduction	103
7.2	Theory	104
7.2.1	Lattice gauge theory on a Hawaiian earring	104
7.2.2	Connection to the cylinder	105
7.2.3	The quantum rotor model	109
7.2.4	Previous studies	111
7.3	Numerical methods	112
7.4	Results of numerical study	112
7.4.1	Symmetry breaking	112
7.4.2	Mass gap	114
7.4.3	Low-lying excitations	115
7.4.4	Beta functions	116
7.5	Discussion of results	118
	Concluding remarks and future directions	121
	Bibliography	123
	Curriculum vitae	139

Introduction

In recent decades, highly general techniques have arisen in condensed matter physics and quantum information that open up whole new avenues of numerical and analytical investigation. These techniques exploit tensor network states (TNS), which are efficient representations of quantum-lattice-system states with limited *entanglement*. The best-known numerical application of TNS is the density-matrix renormalisation group (DMRG) [1], which can be viewed [2] as a variational algorithm applied to a type of one-dimensional TNS known as matrix product states (MPS) [3–5]. DMRG and MPS methods have been extremely successful in condensed matter physics [2], where they are used to obtain accurate information, often at only modest computational cost, about ground states and low-lying excited states of one-dimensional quantum lattice models. There are also methods for the simulation of real-time dynamics [2, 6], where TNS methods have an inherent advantage over commonly-employed Monte Carlo methods, in that they are free of the sign problem [7]. See the introduction to Chapter 1 for more details on DMRG and MPS, especially with regard to numerical methods.

On the analytical side, MPS have been used to completely classify gapped phases in one-dimensional systems [8], whereas a variety of two-dimensional TNS, for example projected entangled pair states (PEPS) [9, 10] and the two-dimensional multiscale entanglement renormalisation ansatz (MERA) [11, 12], have been constructed that represent exotic phases of matter, such as phases with topological order [13–15]. A connection has even been proposed between the ADS/CFT correspondence result in gravity [16] and MERA-like tensor networks [17]. On a related note, there have also been efforts, increasing recently in intensity, to transfer the successes of TNS in condensed matter physics to quantum field theory, particularly with an eye towards simulating nonabelian gauge theory [18–27].

In this thesis, we apply variational MPS tangent-space techniques to examine the phase-structure of a number of related one-dimensional quantum lattice systems. We study the interacting Majorana fermion chain, or “Kitaev edge”, the axial next-nearest neighbour clock (ANNNC) model, and the abelian $O(2)$ and nonabelian $O(4)$ quantum rotor models. The interacting Majorana chain is a very interesting system from a condensed-matter perspective, since it models the edge of a weak topological insulator [28–35]. It is also closely related to the ANNNC model which, as a generalised clock model [36, 37], has an interpretation in terms of generalised Majorana fermions known as parafermions [38]. The clock model degrees of freedom are planar spins that can point in p different directions, generalising the two “up” and “down” directions of Ising spins. Because of this, the clock and ANNNC models can also be interpreted as discretised $O(2)$ rotor models [37], with

the limit $p \rightarrow \infty$ of a continuum of spin orientations resulting in the full $O(2)$ group of rotations. We study the rotor models primarily because of their connection to lattice gauge theories [39], which can be described in terms of the same local degrees of freedom. The key difference between the rotor models and lattice gauge theories is the addition of a local gauge symmetry condition for physicality in the latter case. Despite this difference, however, the physics of the nonabelian rotor model is analogous to that of nonabelian lattice gauge theory in that both models appear to have a spectral gap for all nonzero values of the coupling strength and exhibit a “crossover” regime where weak-coupling behaviour abruptly takes over from strong-coupling behaviour without the occurrence of a phase transition [40].

Each model studied poses its own challenges to TNS techniques. As we show in Chapter 4, the interacting Majorana chain, or “Kitaev edge”, contains multiple gapless (critical) phases related to its lying on a self-dual line within a broader space of theories. We locate a second-order transition between two gapless phases, identifying the central charges of each using finite-entanglement scaling [41, 42]. One of the phases features *incommensurate order*, which manifests itself in modulations of the order-parameter correlation functions, where the ratio of modulation period to lattice spacing can take on irrational values.

The ANNNC model of Chapter 5, in the $p = 2$ case of two spin positions, is a well-known prototypical example of incommensurate order [43]. At higher p we find it exhibits a rich phase structure, featuring commensurate-incommensurate transitions and Berezinskii-Kosterlitz-Thouless transitions, as well as a “disorder line” that marks the border of a region of incommensurate modulations, but is not a phase transition in the usual sense. The ANNNC model also possesses, for $p = 3$, a classically frustrated ground state (for zero external field), immediately adjacent to an apparently critical phase at small nonzero field strength. This phase may be a quantum spin liquid [44].

The rotor models of Chapter 7 feature an infinite-dimensional Hilbert space at each lattice site. For the purposes of MPS numerics, this space must be reduced (cut off) in a way that preserves the relevant physics. Particularly in the nonabelian case, this is nontrivial. We use the generalised Fourier modes of the rotation group as a basis, implementing a cutoff while maintaining rotation-invariance by restricting the available modes. Even with a cutoff, the local Hilbert space dimension remains large, requiring specific optimisations to achieve computational efficiency. Another challenge relevant for lattice quantum field theories is that of taking a continuum limit, which corresponds to approaching a critical point of the lattice model while maintaining accuracy [45]. We approach the continuum limit of the rotor model in our study, which requires a generous Fourier-mode cutoff and also a large MPS bond-dimension.

This thesis is organised as follows. In Chapter 1 we introduce block-uniform MPS alongside some necessary fundamentals concerning quantum lattice systems, before detailing the improvements made, as part of the work presented in this thesis, to the author’s *evoMPS* software package [46], which implements a number of variational algorithms for MPS. We introduce and discuss phase transitions in Chapter 2, defining key concepts, including the types of phase transition that are encountered in later chapters, as well as setting out the scheme of approximate phase-diagram “sketching” using MPS, which we employ in our numerical studies. In Chapter 3, in preparation for our investigations of the Kitaev edge

and ANNNC models, we then review the “second quantisation” formulation of systems of identical particles and define Majorana fermions and parafermions, motivating them via simple condensed matter models in which they describe edge modes. Chapters 4 and 5 document our above-mentioned studies of the interacting Kitaev edge and ANNNC models, each culminating in phase diagram sketches, which we then discuss. For the ANNNC model, we also describe a mesoscopic experimental setup that could simulate its physics. In Chapter 6 we introduce lattice gauge theory, setting out the formal framework needed for our study of the rotor model. In particular, we discuss the use of “graph-manipulation” moves in comparing the physics of differently connected spatial graph discretisations of a gauge theory. Our study of the rotor model follows in Chapter 7, in which we determine the mass gap and beta functions into the weak-coupling regime from MPS ground states and excited states. We also examine the excitation spectrum of the nonabelian $O(4)$ rotor for excitations that are physical under the interpretation of the model as a gauge theory. Finally, we offer concluding remarks and suggestions for further work.

Chapter 1

Block-uniform matrix product states

1.1 Introduction

Matrix product states (MPS) are tensor network states (TNS) for one-dimensional quantum lattice, or many-body, systems [3–5]. MPS represent a parametrisation of a quantum lattice-system Hilbert space with the key property that, for a finite number of parameters per lattice site, the *entanglement* of an MPS is restricted. MPS provide efficient representations of a huge range of physically relevant states, in particular of ground states of local Hamiltonians with a spectral gap, which have finite correlation length [47] and finite entanglement entropy for regions of arbitrary size [48, 49]. In these cases, assuming translation invariance, the number of parameters required for a representation of a given accuracy remains finite even as the system size N is taken to infinity [50, 51]. Furthermore, low-lying excited states can also be approximated well for a wide range of local Hamiltonians [52]. Even in critical systems, where the correlation length and the half-system entanglement entropy diverge [53], ground states can be approximated with an accuracy that scales polynomially in the number of parameters [54, 55].

In the form of the density matrix renormalisation group (DMRG) algorithms [1, 56], which are equivalent to variational methods applied to MPS [2], MPS methods have proved extremely successful in investigating one-dimensional condensed matter models, where their only bias as a class of states comes from the entanglement restriction, which can be adjusted as needed by changing the *bond dimension* D , where the number of parameters in the MPS representation scales as $\mathcal{O}(D^2)$. There are too many results based on DMRG and MPS to list them here. Two recent results on which the author collaborated are a study of a one-dimensional chain of anyons [57] and the development of an MPS ensemble method for simulating open systems [58]. Numerical MPS methods have also been successfully applied to lattice quantum field theories, as detailed in Chapter 7.

There have been many interesting developments in numerical algorithms for MPS since the arrival of the original DMRG algorithm, including methods for real-time evolution and the direct treatment of infinite systems [2]. The set of MPS for a given bond dimension can

also be treated as a variational class and used to implement general variational algorithms such as the time-dependent variational principle (TDVP) [6, 59], which enables both real-time and imaginary-time evolution, where the latter can be used to obtain ground states. The TDVP makes use of the tangent space of an MPS, which also provides a natural set of ansatz states for low-lying excitations [60–62]. Recently, a number of previously proposed algorithms have been understood in terms of the TDVP [63], including the DMRG method, which is related to imaginary-time evolution. For a review of MPS (and other TNS) techniques, see one or more of [2, 10, 64].

In this chapter we begin with a brief overview of key concepts needed before defining *block uniform* MPS, exploring the physical quantities that can be easily extracted. The block uniform MPS formalism is the author’s generalisation of the uniform MPS formalism used in [6, 61]. We also describe the variational algorithms used in the numerical studies of later chapters, which are implemented in the *evoMPS* software package, developed by the present author and collaborators and available under an open source licence [46]. These include the nonlinear conjugate gradient algorithm for energy minimisation [21, 65] and the tangent space [61, 66] excitations ansatz of [60].

1.2 Quantum lattice systems

Matrix product states (MPS) are states of one-dimensional lattice systems that have a Hilbert space isomorphic to

$$\mathcal{H} = \bigotimes_{n=1}^N \mathbb{C}^d, \quad (1.1)$$

where d is the dimension of the local Hilbert space at each site n . We sometimes refer to such systems as *spin chains*, because one-dimensional systems of spins have this form. *Pure states* on \mathcal{H} can be written as vectors and have the form

$$|\psi\rangle = \sum_{s_1, \dots, s_N} c_{s_1, \dots, s_N} |s_1 s_2 \dots s_N\rangle, \quad (1.2)$$

where $c_{s_1, \dots, s_N} \in \mathbb{C}$ are the coefficients in a chosen orthonormal basis

$$\langle s_1 s_2 \dots s_N | t_1 t_2 \dots t_N \rangle = \delta_{s_1 t_1} \delta_{s_2 t_2} \dots \delta_{s_N t_N}. \quad (1.3)$$

1.2.1 Correlations and entanglement

The success of the MPS representation depends on its ability to capture states accurately using a limited amount of entanglement. The key tools we use to investigate the entanglement properties of MPS are connected correlation functions, the Schmidt decomposition, and the von Neumann entropy, or entanglement entropy, which we briefly define here. For more details see, for example [67].

Entanglement is responsible for all correlations in pure quantum states. We define the spatial *connected correlation function* (which we sometimes abbreviate to “correlation function”) for operators X_n and Y_n to be

$$C_{X,Y}(n, d) = \langle X_n Y_{n+d} \rangle - \langle X_n \rangle \langle Y_{n+d} \rangle, \quad (1.4)$$

where n labels a lattice site at which the operator X_n or Y_n is localised and d is the distance in lattice sites. We take X_n and Y_n to be local in the sense that they have nontrivial support on a finite interval of the spin chain starting at site n . The angle brackets denote the expectation value for a state $|\Psi\rangle$: $\langle X_n \rangle \equiv \langle \Psi | X_n | \Psi \rangle$. If the state features no entanglement between lattice sites, such that there is only one nonzero coefficient c_{s_1, \dots, s_N} in (1.2), the correlation function is zero

$$C_{X,Y}(n, d) \stackrel{\text{no ent.}}{=} \langle X_n \rangle \langle Y_{n+d} \rangle - \langle X_n Y_{n+d} \rangle = 0. \quad (1.5)$$

In this case, the state is called a *product state*. If multiple c_{s_1, \dots, s_N} are nonzero, there is entanglement in the system with respect to some bipartite decomposition of the Hilbert space in terms of lattice sites.

We now investigate bipartite decompositions. We can always decompose the Hilbert space (1.1) of a lattice system into two subsystems A and B such that

$$\mathcal{H} = \mathcal{H}_A \otimes \mathcal{H}_B. \quad (1.6)$$

The *Schmidt decomposition* expresses any pure state $|\Psi\rangle \in \mathcal{H}$ in the form

$$|\Psi\rangle = \sum_{\alpha=1}^{\chi} \lambda_{\alpha} |\psi_A^{\alpha}\rangle \otimes |\psi_B^{\alpha}\rangle, \quad (1.7)$$

where the *Schmidt vectors* $|\psi_A^{\alpha}\rangle$ and $|\psi_B^{\alpha}\rangle$ are orthonormal bases for the subspaces of \mathcal{H}_A and \mathcal{H}_B where the state has support. The λ_{α} , which must satisfy $\sum_{\alpha=1}^{\chi} \lambda_{\alpha}^2 = 1$ for normalised $|\Psi\rangle$, are called *Schmidt coefficients* and the number of Schmidt coefficients χ needed to represent the state in the form (1.7) is called the *Schmidt rank*. If $\chi = 1$ the decomposition is trivial and there is no entanglement between subsystems A and B .

The *von Neumann entropy* or *entanglement entropy* is defined for *mixed states* ρ , which are positive semi-definite Hermitian operators on \mathcal{H} satisfying $\text{tr}(\rho) = 1$ when normalised, as

$$S(\rho) = -\text{tr}(\rho \log \rho), \quad (1.8)$$

where we use, unless otherwise stated, the base-two logarithm (in this case the matrix logarithm). The entropy is maximised for the *maximally-mixed* state $\rho = \dim(\mathcal{H})^{-1} \mathbb{I}_{\dim(\mathcal{H})}$, where we find $S = \log(\dim(\mathcal{H}))$. The entropy can also be written in terms of the eigenvalues γ_{α} of ρ as

$$S(\rho) = -\sum_{\alpha} \gamma_{\alpha} \log \gamma_{\alpha}, \quad (1.9)$$

such that pure states $\rho = |\Psi\rangle\langle\Psi|$, which have a single nonzero eigenvalue $\gamma_1 = 1$, have $S = 0$. Despite the pure state of the entire system having zero entropy, the entropy of the *reduced state* on a subsystem \mathcal{H}_A is generally nonzero. The reduced state is given by

$$\rho_A \equiv \text{tr}_B(\rho) \equiv \sum_{\alpha} (\mathbb{I}_A \otimes \langle \psi_B^{\alpha} |) \rho (\mathbb{I}_A \otimes | \psi_B^{\alpha} \rangle), \quad (1.10)$$

where $|\psi_B^\alpha\rangle$ is an orthonormal basis for the subspace of \mathcal{H}_B on which ρ has nontrivial support. Inserting the pure state $\rho = |\Psi\rangle\langle\Psi|$, and using the Schmidt vectors $|\psi_B^\alpha\rangle$ from the A, B Schmidt decomposition (1.7) as a basis for the support of ρ on \mathcal{H}_B , we find

$$S(\rho_A) = - \sum_{\alpha=1}^{\chi} \lambda_\alpha^2 \log \lambda_\alpha^2, \quad (1.11)$$

such that the reduced state on A has nonzero entropy if, and only if, $\chi > 1$. We will often refer to the *half-chain* entanglement entropy, which is (1.11) with the subsystem A equal to one half of the system: $\mathcal{H}_A = \bigotimes_{n=1}^{N/2} \mathbb{C}^d$.

1.3 Block-uniform matrix product states

Matrix product states (MPS) are states of one-dimensional lattice systems in which the coefficients for the terms of the state, in a chosen basis, are “generated” by a product of matrices, with one matrix assigned to each basis element at each site. Here, we restrict ourselves to states of infinite systems that are invariant under translations of L sites. They live in the Hilbert space (1.1) of an infinite one-dimensional system ($N \rightarrow \infty$). These states, which we call *block-uniform* MPS, are defined as

$$|\Psi[A]\rangle = \sum_{\mathbf{s}=0}^{d-1} v_L^\dagger \left[\prod_{n=-\infty}^{+\infty} A_1^{s_{(n-1)L+1}} \dots A_L^{s_{nL}} \right] v_R |\mathbf{s}\rangle, \quad (1.12)$$

where A_k^s is a $D \times D$ complex matrix of parameters, D is the *bond dimension*, and \mathbf{s} is shorthand for $s_{-\infty} \dots s_0 s_1 \dots s_{+\infty}$. Each s_n runs from 0 to $d-1$ and enumerates the chosen orthonormal basis elements $|0\rangle \dots |d-1\rangle$ on each site n in the spin chain. The boundary vectors v_L, v_R drop out of calculations as long as correlations decay to zero over an infinite distance, since the bulk is then completely decoupled from the infinitely distant boundaries. We will shortly see how to ensure this is the case.

Note that we may think of the d matrices A_k^s belonging to each site as a three-dimensional *tensor* A_k , with $d \times D \times D$ complex entries. Each A_k thus has a *physical* index s_n of dimension d in addition to the two matrix indices of dimension D , which we will sometimes refer to as *virtual* or *bond* indices. It is often convenient to represent the state (1.12) as a *tensor network*

$$|\Psi[A]\rangle = \left(\overline{v}_L \right) \text{---} \left[\begin{array}{c} \boxed{A_1} \\ \text{---} \\ \boxed{A_2} \\ \text{---} \\ \vdots \\ \boxed{A_L} \\ \text{---} \\ \boxed{A_1} \\ \text{---} \\ \boxed{A_2} \\ \text{---} \\ \vdots \\ \boxed{A_L} \end{array} \right] \text{---} \left(v_R \right), \quad (1.13)$$

where the indices of the tensors A_k are represented as “legs” and we use dashed lines to represent tensors we have left out for brevity. The two horizontal legs of each A_k represent the virtual indices, whereas the vertical leg represents the physical index. Connecting a leg from one tensor to a leg of another tensor sets the corresponding indices to be equal and sums over their value, hence the horizontal connections in (1.13) represent the matrix multiplication in (1.12). In the language of tensors, summing over a pair of indices to produce a new tensor is called *contraction*. The tensor network itself represents a tensor formed by carrying out the contractions indicated by connecting legs. The vertical indices

in (1.13) are left dangling (uncontracted): They represent the basis elements for each site in the Hilbert space. The sum over s_n in (1.12) simply assigns the physical indices of the A_k to their corresponding basis elements $|s_n\rangle$, so it need not appear in (1.13) as long as we recall that the vertical indices of the A_k “live” in the Hilbert space.

Note that we can always obtain a fully translation-invariant MPS ($L = 1$) from an MPS with $L > 1$ by combining L physical sites, each with Hilbert space \mathbb{C}^d , into a single effective site with Hilbert space $(\mathbb{C}^d)^{\otimes L} \cong \mathbb{C}^{d^L}$. We call this operation *blocking*.

1.3.1 Computing the norm

Let us use the tensor network notation to help us calculate the norm of the state (1.13). Since we use an orthonormal physical basis, $\langle \Psi[A] | \Psi[A] \rangle$ contains only a single sum over the physical indices s_n . This means we may simply connect the physical legs of the bra and ket states:

$$\langle \Psi[A] | \Psi[A] \rangle = \begin{array}{c} \overline{v}_L \text{---} \boxed{A_1} \text{---} \boxed{A_2} \text{---} \cdots \boxed{A_L} \text{---} \boxed{A_1} \text{---} \boxed{A_2} \text{---} \cdots \boxed{A_L} \text{---} v_R \\ | \\ \overline{v}_L \text{---} \boxed{\overline{A}_1} \text{---} \boxed{\overline{A}_2} \text{---} \cdots \boxed{\overline{A}_L} \text{---} \boxed{\overline{A}_1} \text{---} \boxed{\overline{A}_2} \text{---} \cdots \boxed{\overline{A}_L} \text{---} \overline{v}_R \end{array}, \quad (1.14)$$

where $\overline{A_k}$ denotes the complex conjugate. Note that this network is equal to a number, which corresponds to there being no dangling legs (all legs participate in contractions). In general, the number of dangling legs gives the number of indices (dimensions) of the tensor represented by the entire network. An important property of tensor networks is that any sub-network, formed by cutting along legs, is also a valid expression. The norm (1.14) contains the part

$$\boxed{E_k} \equiv \begin{array}{c} \boxed{A_k} \\ | \\ \boxed{\overline{A}_k} \end{array}, \quad (1.15)$$

where $k = 1 \dots L$ and on the left-hand side we have carried out the contraction of the physical indices, forming a new four-dimensional tensor E_k . If we interpret the pairs of D -dimensional indices on the left and right each as single indices of dimension D^2 , we can think of E_k as a $D^2 \times D^2$ matrix. This matrix encodes a number of important properties of the MPS and is called the *transfer matrix*. We can write it in algebraic form as

$$E_k = \sum_s A_k^s \otimes \overline{A_k^s}, \quad (1.16)$$

where the tensor product represents the combination of the two horizontal indices on each side of E_k into one. Writing (1.14) using (1.15) we get

$$\langle \Psi[A] | \Psi[A] \rangle = \begin{array}{c} \overline{v}_L \text{---} \boxed{E_1} \text{---} \boxed{E_2} \text{---} \cdots \boxed{E_L} \text{---} \boxed{E_1} \text{---} \boxed{E_2} \text{---} \cdots \boxed{E_L} \text{---} v_R \\ | \\ \overline{v}_L \text{---} \boxed{E_1} \text{---} \boxed{E_2} \text{---} \cdots \boxed{E_L} \text{---} \boxed{E_1} \text{---} \boxed{E_2} \text{---} \cdots \boxed{E_L} \text{---} \overline{v}_R \end{array}, \quad (1.17)$$

which we note now consists of an infinite matrix product between the boundary vectors. By defining the *block transfer matrix*

$$\mathbf{E}_k \equiv E_k E_{k+1} \cdots E_{k+L-1}, \quad (1.18)$$

where the sums in the subscripts use modular arithmetic, we can make the product uniform. For \mathbf{E}_k with any $k = 1 \dots L$, we find

$$\begin{aligned} \langle \Psi[A] | \Psi[A] \rangle &= \begin{array}{c} \overline{v}_L \\ \vdots \\ \mathbf{E}_k \text{---} \mathbf{E}_k \text{---} \mathbf{E}_k \text{---} \vdots \\ v_L \end{array} \begin{array}{c} v_R \\ \vdots \\ \mathbf{E}_k \text{---} \mathbf{E}_k \text{---} \mathbf{E}_k \text{---} \vdots \\ \overline{v}_R \end{array} \\ &= \langle v_L \otimes \overline{v}_L | \left(\prod_{n=-\infty}^{+\infty} \mathbf{E}_k \right) | v_R \otimes \overline{v}_R \rangle, \end{aligned} \quad (1.19)$$

which implies conditions for \mathbf{E}_k if we want the state to be normalised. Firstly, we need that the largest eigenvalues of \mathbf{E}_k have magnitude 1, which we can always achieve by scaling the A_k . Otherwise, the norm of the infinite matrix product will diverge. In the simplest case \mathbf{E}_k has only one nondegenerate eigenvalue of magnitude 1, which must then be equal to 1 due to the form of (1.16)¹, and where all other eigenvalues have magnitude smaller than 1. This implies

$$r(\mathbf{E}_k - |r_k\rangle\langle l_k|) < 1, \quad (1.20)$$

where $r(X)$ is the *spectral radius* of X and $|l_k\rangle$ and $|r_k\rangle$ are the (normalised) left and right eigenvectors of \mathbf{E}_k corresponding to the eigenvalue 1:

$$\mathbf{E}_k |r_k\rangle = |r_k\rangle, \quad \langle l_k | \mathbf{E}_k = \langle l_k |, \quad (1.21)$$

where we generalise to the block transfer matrix \mathbf{E}_k with the block starting as sites nk . In terms of diagrams, this is

$$\begin{array}{c} \overline{l}_k \\ \vdots \\ \mathbf{E}_k \\ \vdots \\ l_k \end{array} = \begin{array}{c} \overline{l}_k \\ \vdots \\ \vdots \\ \vdots \\ l_k \end{array}, \quad \begin{array}{c} \mathbf{E}_k \\ \vdots \\ \mathbf{E}_k \\ \vdots \\ \mathbf{E}_k \end{array} \begin{array}{c} r_k \\ \vdots \\ \overline{r}_k \end{array} = \begin{array}{c} \vdots \\ \vdots \\ \vdots \\ \vdots \\ r_k \end{array}. \quad (1.22)$$

With these spectral properties we have

$$\lim_{n \rightarrow \infty} (\mathbf{E}_k)^n |v_R \otimes \overline{v}_R\rangle = |r_k\rangle \quad (1.23)$$

$$\lim_{n \rightarrow \infty} \langle v_L \otimes \overline{v}_L | (\mathbf{E}_k)^n = \langle l_k |, \quad (1.24)$$

or in diagrams

$$\begin{array}{c} \overline{v}_L \text{---} \dots \text{---} [A_1] \text{---} [A_2] \text{---} \dots \text{---} [A_{k-1}] \text{---} \\ | \\ v_L \text{---} \dots \text{---} [\overline{A}_1] \text{---} [\overline{A}_2] \text{---} \dots \text{---} [\overline{A}_{k-1}] \text{---} \end{array} = \begin{array}{c} \overline{l}_k \\ \vdots \\ \vdots \\ \vdots \\ l_k \end{array}, \quad \begin{array}{c} [A_k] \text{---} \dots \text{---} [A_L] \text{---} [A_1] \text{---} \dots \text{---} v_R \\ | \\ [\overline{A}_k] \text{---} \dots \text{---} [\overline{A}_L] \text{---} [\overline{A}_1] \text{---} \dots \text{---} \overline{v}_R \end{array} = \begin{array}{c} \vdots \\ \vdots \\ \vdots \\ \vdots \\ r_k \end{array}, \quad (1.25)$$

assuming the left and right boundary vectors are not orthogonal to $|l_k\rangle$ and $|r_k\rangle$, respectively. This gives us

$$\langle \Psi[A] | \Psi[A] \rangle = \langle l_k | r_k \rangle = 1, \quad (1.26)$$

¹Without loss of generality, we may treat the $L = 1$ case. The transfer matrix $\mathbf{E}_1 = E_1 =: E$ of can be written as a single term $\tilde{A} \otimes \overline{\tilde{A}}$ acting in an enlarged $d^2 D^2 \times d^2 D^2$ space, with $[\tilde{A}]_{(s,\alpha);(t,\beta)} \equiv [A^t]_{\alpha\beta} \quad \forall s$. Furthermore, a matrix of the form $A \otimes \overline{A}$ has eigenvalues $\lambda_j \overline{\lambda}_k$, where the λ_j are the eigenvalues of A . Thus eigenvalues come in conjugate pairs and, if an eigenvalue is unique in magnitude, it must be real and positive. Taken together, these properties imply that if $E = \sum_s A^s \otimes \overline{A}^s$ has a unique eigenvalue of largest magnitude, it must also be real and positive.

where the boundary vectors no longer appear — they are “decoupled”. If we allow multiple eigenvalues of magnitude 1, in \mathbf{E}_k , or in case the eigenvalue 1 is degenerate, we must include the boundary vectors, since they will be responsible for choosing which components of the state are present. Since we will be interested in states with decaying correlations, where the bulk is not correlated with the boundary in the infinite setting, we stick to the simpler case of a single, nondegenerate largest eigenvalue. We additionally assume for the remainder that \mathbf{E}_k has full rank (no zero eigenvalues). Furthermore, we will sometime simplify notation by taking $\mathbf{E} \equiv \mathbf{E}_1$.

Note that vectors in the D^2 -dimensional space in which \mathbf{E}_k acts, such as $|l_k\rangle$ and $|r_k\rangle$, have a matrix form if we “unravel” the doubled D -dimensional virtual legs

$$\begin{aligned} \begin{array}{c} \alpha \\ \beta \end{array} \text{---} \text{---} \text{---} \text{---} x &= \alpha \text{---} \text{---} \text{---} \text{---} x \text{---} \text{---} \text{---} \beta \\ \langle \langle \alpha | \otimes \langle \beta | | x \rangle &\equiv x_{\alpha\beta} \end{aligned} \quad (1.27)$$

where $|\alpha\rangle$ and $|\beta\rangle$ are unit vectors in the D -dimensional virtual space.

1.3.2 Fidelity per site

It will be important, particularly in the context of symmetries, to compute the *fidelity* $\langle \Psi[A] | \Psi[\tilde{A}] \rangle$ of two block-uniform MPS $|\Psi[A]\rangle$ and $|\Psi[\tilde{A}]\rangle$. It is calculated precisely as the norm (1.19), except that an *overlap* transfer matrix

$$\mathbf{E}_A^{\tilde{A}} \equiv E_{A_1}^{\tilde{A}_1} \dots E_{A_L}^{\tilde{A}_L}, \quad (1.28)$$

with

$$\boxed{E_{A_k}^{\tilde{A}_k}} \equiv \begin{array}{c} \boxed{\tilde{A}_k} \\ | \\ \boxed{A_k} \end{array}, \quad (1.29)$$

takes the place of the usual transfer matrix (1.15), where we have simplified by assuming both MPS have the same block lengths $L = \tilde{L}$. In general, the two MPS can have different block lengths, in which case the overlap transfer matrix has a block length equal to the lowest common multiple of L and \tilde{L} .

The result $\langle \Psi[A] | \Psi[\tilde{A}] \rangle$ depends on the spectrum of $\mathbf{E}_A^{\tilde{A}}$. Assuming it has a non-degenerate largest eigenvalue λ_1 , which we can always make real by multiplying \tilde{A}_k by a (nonphysical) phase, we can write

$$\langle \Psi[A] | \Psi[\tilde{A}] \rangle = \lim_{n \rightarrow \infty} (|\lambda_1|)^n, \quad (1.30)$$

where the result is only well defined if $|\lambda_1| \leq 1$, which is always the case if $|\Psi[A]\rangle$ and $|\Psi[\tilde{A}]\rangle$ are normalised. Given this, if $|\lambda_1| = 1$, the fidelity is one, otherwise it is zero.

We call $|\lambda_1|$ the fidelity *per block* and $|\lambda_1|^{1/L}$ the fidelity *per site*. With numerically obtained MPS, the per-site fidelity will never exactly equal one due to limited numerical precision, such that $\langle \Psi[A] | \Psi[\tilde{A}] \rangle = 0$. We can still, however, approximately check for fidelity one by testing if the per-site fidelity is *close* to one.

1.3.3 Gauge transformations

Block-uniform matrix product states (1.12) are invariant under transformations of the parameters

$$A_k^s \mapsto g_{k-1}^{-1} A_k^s g_k, \quad (1.31)$$

where $g_0 = g_L$ and the g_k are invertible $D \times D$ matrices. It is easy to see that the state $|\Psi[A]\rangle$ is invariant under this parameter transformation, since it amounts to inserting the identity matrix between each A_k and A_{k+1} in (1.12). Note that, if we are careful not to count the trivial gauge transformation $g_k = \mathbb{I}$, and if we include changes in the norm $A_k \mapsto cA_k$ ($c \in \mathbb{C}$), there are thus $1 + D^2 - 1$ nonphysical degrees of freedom in each tensor A_k , which therefore contains

$$\dim(A_k)_{\text{phys}} = D^2(d - 1) \quad (1.32)$$

physical degrees of freedom.

We complete this brief section on gauge transformations by noting how the transfer matrix eigenvectors $|l_k\rangle$ and $|r_k\rangle$ transform, which we can see by examining (1.25). We find for the matrix forms (1.27)

$$l_k \mapsto g_{k-1}^\dagger l_k g_{k-1}, \quad r_k \mapsto g_{k-1}^{-1} r_k (g_{k-1}^{-1})^\dagger. \quad (1.33)$$

1.3.4 Canonical forms

Using gauge transformations it is always possible to bring an MPS into certain *canonical forms* in which there is no remaining gauge freedom. We specify one example here: The *right canonical form* is defined by

$$r_k = \mathbb{I} \quad \text{and} \quad [l_k]_{\alpha\beta} = \delta_{\alpha\beta} [l_k]_{\alpha\beta} \quad (1.34)$$

for all k , which we can achieve using (1.33) as long as l_k, r_k have full rank (the transformation g_{k-1} needed to achieve $r_k = \mathbb{I}$ is defined up to a unitary factor, which we then use to diagonalise l_k , thus fixing the g_{k-1} needed completely).

A canonical form is useful for numerical computations, since it is well-conditioned: It is easy to find inverses and roots of r_k, l_k in the form (1.34).

1.3.5 Expectation values and correlation functions

The spectrum of the transfer matrix carries a lot of information about correlations. To see this, let us compute a two-point correlation function (1.4) using local operators X_n and Y_n . Calculating the expectation value of a local operator is almost the same as calculating the norm. As a tensor network it is

$$\langle \Psi[A] | X_{nL} | \Psi[A] \rangle = \begin{array}{c} \overline{v}_L \text{---} \boxed{A_1} \text{---} \boxed{A_2} \text{---} \dots \text{---} \boxed{A_L} \text{---} \boxed{A_1} \text{---} \boxed{A_2} \text{---} \dots \text{---} \boxed{A_L} \text{---} v_R \\ | \\ \boxed{X} \\ | \\ \underline{v}_L \text{---} \boxed{\overline{A}_1} \text{---} \boxed{\overline{A}_2} \text{---} \dots \text{---} \boxed{\overline{A}_L} \text{---} \boxed{\overline{A}_1} \text{---} \boxed{\overline{A}_2} \text{---} \dots \text{---} \boxed{\overline{A}_L} \text{---} \overline{v}_R \end{array}, \quad (1.35)$$

where, instead of just connecting up the bra and ket legs where the operator acts, we must instead contract with the operator. In this example, X_{nL} acts on sites X_{nL} and X_{nL+1} and is represented by a tensor X with four *physical* legs, corresponding to the Hilbert space basis elements for two sites. We can write the tensor as

$$X_{(s,t),(u,v)} \equiv \langle s, t | X | u, v \rangle. \quad (1.36)$$

Using (1.25) we can simplify (1.35) to

$$\langle \Psi[A] | X_{nL} | \Psi[A] \rangle = \langle l_L | \left(\begin{array}{c} \boxed{A_L} \text{---} \boxed{A_1} \\ | \\ \boxed{X} \\ | \\ \boxed{A_L} \text{---} \boxed{A_1} \end{array} \right) | r_2 \rangle \equiv \langle l_L | E_{L,1}^X | r_2 \rangle = \langle l_L | E_{L,1}^X | r_2 \rangle, \quad (1.37)$$

where we summarise the central part as the two-site *operator transfer matrix*

$$E_{L,1}^X = \sum_{s,t,u,v} \langle s, t | X | u, v \rangle (A_L^u A_1^v) \otimes \overline{(A_L^s A_1^t)}. \quad (1.38)$$

The generalisation to expectation values of two, separated local operators is straightforward

$$\langle \Psi[A] | X_{nL} Y_{nL+d} | \Psi[A] \rangle = \langle l_L | E_{L,1}^X \left(\prod_{k=2}^{L+d-1} E_k \right) E_{L+d, L+d+1}^Y | r_{L+d+2} \rangle, \quad (1.39)$$

where we assume Y also acts on two neighbouring sites, and we again use modulo arithmetic when computing subscript indices for the E .

We now have the ingredients needed to compute (1.4). To simplify the notation, we switch to a fully translation-invariant setting $L = 1$, which we can do without loss of generality by blocking, as described in Section 1.3. Note that, for $L = 1$, $\mathbf{E}_1 = E_1 = E$. The correlation function then becomes

$$\begin{aligned} C_{X,Y}(d) &= \langle l | E^X (E)^{d-1} E^Y | r \rangle - \langle l | E^X | r \rangle \langle l | E^Y | r \rangle \\ &= \langle l | E^X (\mathbb{I} - |r\rangle\langle l|) (E)^{d-1} (\mathbb{I} - |r\rangle\langle l|) E^Y | r \rangle, \end{aligned} \quad (1.40)$$

where for the second line we have used that $(\mathbb{I} - |r\rangle\langle l|)$ is a projector that commutes with E . It projects out any components that would not decay under $(E)^{d-1}$, since the spectral radius of $(E - |r\rangle\langle l|)$ is strictly less than one (1.21). This proves that correlation functions generically decay in uniform MPS. Indeed, they decay exponentially, with asymptotic behaviour

$$C_{X,Y}(d) \stackrel{d \rightarrow \infty}{\sim} (\lambda_2)^d = e^{-d \ln \frac{1}{\lambda_2}}, \quad (1.41)$$

where λ_2 , which satisfies $|\lambda_2| < 1$, is an eigenvalue of second-largest magnitude of E , which corresponds to the slowest-decaying component of (1.40). We therefore find that the *correlation length*, the rate of decay of the slowest-decaying correlation function, is given by

$$\xi = -\ln |\lambda_2|, \quad (1.42)$$

which is positive and finite for all MPS, as we have defined them.

1.3.6 Modulated correlations

We now consider the effects of a nontrivial phase on the larger eigenvalues $\lambda_2, \lambda_3, \dots$ of E on the correlation function (1.40). Let us take a simple example in which $\lambda_2 = |\lambda_2|e^{i\phi}$, $\lambda_3 = |\lambda_3|e^{-i\phi}$ and $|\lambda_{m>3}| \ll |\lambda_2|$. We may then neglect the eigenvalues $\lambda_{m>3}$ in the correlation function, which simplifies to

$$C_{X,Y}(d) = |\lambda_2|^{d-1} \langle l|E^X \left[e^{i\phi(d-1)}|r_{\lambda_2}\rangle\langle l_{\lambda_2}| + e^{-i\phi(d-1)}|r_{\lambda_3}\rangle\langle l_{\lambda_3}| \right] E^Y|r\rangle + \mathcal{O}(|\lambda_3|), \quad (1.43)$$

where l_{λ_m} and r_{λ_m} are the left and right eigenvectors corresponding to the eigenvalue λ_m of E , which we assume to be non-degenerate. We see that the correlation function is modulated with phase ϕ . Furthermore, if $\langle l|E^X|r_{\lambda_2}\rangle\langle l_{\lambda_2}|E^Y|r\rangle = \langle l|E^X|r_{\lambda_3}\rangle\langle l_{\lambda_3}|E^Y|r\rangle$, we have a purely real modulation

$$C_{X,Y}(d) \sim 2 \cos(\phi(d-1)) |\lambda_2|^{d-1}. \quad (1.44)$$

Modulated correlation functions like this can occur with arbitrary phase ϕ in systems with incommensurate order. For more information, see Section 2.2.5.

1.3.7 Schmidt decomposition and half-chain entropy

We have seen that, in an MPS, correlations decay exponentially. Now we further examine the entanglement structure of an MPS using the Schmidt decomposition (1.7). It is easy to find an expression for a decomposition of an MPS into two semi-infinite halves. For a splitting between a site $k-1$ and the neighbouring site k we have

$$|\Psi[A]\rangle = \sum_{\alpha} |\psi_{L,k}^{\alpha}\rangle \otimes |\psi_{R,k}^{\alpha}\rangle \quad (1.45)$$

$$\equiv \sum_{\alpha} \left(\overline{v}_L \cdots \boxed{A_1} \boxed{A_2} \cdots \boxed{A_{k-1}} \right) \alpha \quad \alpha \left(\boxed{A_k} \cdots \boxed{A_1} \boxed{A_2} \cdots v_R \right).$$

However, this does not yet have the form of the Schmidt decomposition. In the Schmidt form, if we absorb the Schmidt coefficients into the left and right Schmidt vectors $|\psi_{X,k}^{\alpha}\rangle$, we have that $|\psi_{X,k}^{\alpha}\rangle$ form an orthogonal set of states for both $X = L$ and $X = R$. In this case the overlap of the $|\psi_{X,k}^{\alpha}\rangle$ with the state

$$\Lambda_{\alpha\beta}^{(k)} \equiv \left(\langle \psi_{L,k}^{\alpha} | \otimes \langle \psi_{R,k}^{\beta} | \right) |\Psi[A]\rangle, \quad (1.46)$$

is a diagonal matrix containing the squares of the Schmidt coefficients. In general, the $|\psi_{X,k}^{\alpha}\rangle$ in (1.45) do not form orthonormal sets and Λ is not diagonal. We can compute Λ with the help of tensor networks as

$$\Lambda_{\alpha\beta}^{(k)} = \begin{array}{c} \overline{v}_L \cdots \boxed{A_1} \boxed{A_2} \cdots \boxed{A_{k-1}} \cdots \boxed{A_k} \cdots \boxed{A_1} \boxed{A_2} \cdots v_R \\ v_L \cdots \boxed{\overline{A}_1} \boxed{\overline{A}_2} \cdots \boxed{\overline{A}_{k-1}} \cdots \alpha \beta \boxed{\overline{A}_k} \cdots \boxed{\overline{A}_1} \boxed{\overline{A}_2} \cdots \overline{v}_R \end{array} \quad (1.47)$$

$$= \begin{array}{c} \overbrace{l_k}^{\alpha} \quad \overbrace{r_k}^{\beta} \end{array}$$

$$= \alpha \overbrace{l_k} \quad \overbrace{r_k} \beta$$

where in the last step we have “unravelling” the network to show that we may treat the contraction as matrix multiplication from left to right

$$\Lambda_{\alpha\beta}^{(k)} = [l_k \ r_k]_{\alpha\beta}, \quad (1.48)$$

where we have used the matrix forms for $|l_k\rangle$ and $|r_k\rangle$ from (1.27).

Recalling (1.33), we now see that gauge transformations (1.31) act on Λ to give

$$\tilde{\Lambda}^{(k)} = g_{k-1}^\dagger \Lambda^{(k)} (g_{k-1}^{-1})^\dagger, \quad (1.49)$$

where we can obtain diagonal $\tilde{\Lambda}^{(k)}$ using unitary g_{k-1} . This gauge transformation modifies the vectors $|\psi_{X,k}^\alpha\rangle$ of (1.45) such that they form orthogonal (but not normalised) sets and brings the decomposition into Schmidt form, such that (1.46) contains the squares of the Schmidt coefficients λ_α :

$$(\lambda_\alpha^{(k)})^2 = [\tilde{\Lambda}^{(k)}]_{\alpha\alpha}. \quad (1.50)$$

In other words, we can find the squared Schmidt coefficients for a splitting of the chain into two semi-infinite halves between $k-1$ and k by computing the eigenvalues of the matrix $l_k \ r_k$. This immediately gives us the half-chain entanglement entropy (1.9), since the squared Schmidt coefficients are the eigenvalues of the reduced density matrix for one half of the system.

Note that the Schmidt rank of the MPS is less than or equal to the dimension of Λ , which is the bond dimension D . In this sense, the bond dimension limits the amount of entanglement in the state. This implies (see Section 1.2.1) a maximum value for the half-chain entanglement entropy

$$S_{\text{half}} \leq \log(D). \quad (1.51)$$

From these considerations it is also clear that, in the limit $D \rightarrow \infty$, any block-translation-invariant pure state in the Hilbert space \mathcal{H} can be represented as a block-uniform MPS, since then the Schmidt rank is unlimited for any bipartite decomposition.

In the case where the state $|\Psi[A]\rangle$ is invariant under a symmetry represented by a unitary transformation consisting of a product of on-site unitaries

$$\mathbf{U} = \bigotimes_{n=-\infty}^{+\infty} U, \quad (1.52)$$

there is a further interesting calculation we can perform using the Schmidt vectors $|\psi_{R,k}^\alpha\rangle$. They can have expectation values under the unitary transformation restricted to half of the chain $\langle \psi_{R,k}^\alpha | \bigotimes_{n=k}^{+\infty} U | \psi_{R,k}^\alpha \rangle$ other than 1, despite $\langle \Psi[A] | \mathbf{U} | \Psi[A] \rangle = 1$. Given that we have already performed the gauge transformation (1.49) needed to obtain the Schmidt form, we

have

$$\begin{aligned}
\langle \psi_{R,k}^\alpha | \bigotimes_{n=k}^{+\infty} U | \psi_{R,k}^\beta \rangle &= \begin{array}{c} \alpha \text{---} [A_k] \text{---} [A_1] \text{---} [A_2] \text{---} \dots \text{---} \widehat{v_R} \\ | \\ U \quad U \quad U \\ | \\ \beta \text{---} [A_k] \text{---} [A_1] \text{---} [A_2] \text{---} \dots \text{---} \widehat{\bar{v}_R} \end{array} \\
&= \begin{array}{c} \alpha \text{---} [\tilde{A}_k] \text{---} [\tilde{A}_1] \text{---} [\tilde{A}_2] \text{---} \dots \text{---} v_R \\ | \\ [\tilde{A}_k] \text{---} [\tilde{A}_1] \text{---} [\tilde{A}_2] \text{---} \dots \text{---} \bar{v}_R \end{array}, \tag{1.53}
\end{aligned}$$

where for the final line we form \tilde{A}_k by contracting A_k with U . We can formulate this expression in terms of the eigenvector $|\tilde{r}\rangle$ of the overlap transfer matrix (1.28) corresponding to the eigenvalue of largest magnitude. This eigenvalue has magnitude 1 since we are assuming $\langle \Psi[A] | \mathbf{U} | \Psi[A] \rangle = 1$, such that we can set it to equal 1 by multiplying \tilde{A}_k by a phase. We thus have

$$\frac{\langle \psi_{R,k}^\alpha | \bigotimes_{n=k}^{+\infty} U | \psi_{R,k}^\alpha \rangle}{\langle \psi_{R,k}^\alpha | \psi_{R,k}^\alpha \rangle} = \frac{\tilde{r}_{\alpha\alpha}}{r_{\alpha\alpha}}. \tag{1.54}$$

These expectation values are interesting in the context of analysing the Schmidt decomposition, which can reveal useful information about the state in certain cases. See Section 5.3.3 for more details.

1.3.8 Tangent space

Matrix product states form a differentiable manifold [61, 66]. We can find the tangent space by taking the derivative with respect to the parameters,

$$\begin{aligned}
\sum_t \sum_{\alpha\beta} [B_k^t]_{\alpha\beta} \frac{\partial}{\partial [A_k^t]_{\alpha\beta}} |\Psi[A]\rangle &= \sum_{m=-\infty}^{+\infty} \sum_{s=0}^{d-1} v_L^\dagger \left[\prod_{n=-\infty}^{m-1} A_1^{s(n-1)L+1} \dots A_L^{s_n L} \right] \times \\
&A_1^{s(m-1)L+1} \dots B_k^{s(m-1)L+k} \dots A_L^{s_m L} \times \\
&\left[\prod_{n=m+1}^{+\infty} A_1^{s(n-1)L+1} \dots A_L^{s_n L} \right] v_R |s\rangle, \tag{1.55}
\end{aligned}$$

where we have parameterised the tangent vector using tensors B_k . In case $L = 1$ this simplifies to

$$\begin{aligned}
\sum_t \sum_{\alpha\beta} [B^t]_{\alpha\beta} \frac{\partial}{\partial [A^t]_{\alpha\beta}} |\Psi(A)\rangle &= \sum_{m=-\infty}^{+\infty} \sum_{s=0}^{d-1} v_L^\dagger \left[\prod_{n=-\infty}^{m-1} A^{s_n} \right] B^{s_m} \left[\prod_{n=m+1}^{+\infty} A^{s_n} \right] v_R |s\rangle. \tag{1.56}
\end{aligned}$$

In the sequel we use the notation

$$|\Phi[A, B]\rangle \equiv \sum_{k=1}^L \sum_{t=0}^{d-1} \sum_{\alpha, \beta=0}^D [B_k^t]_{\alpha\beta} \frac{\partial}{\partial [A_k^t]_{\alpha\beta}} |\Psi[A]\rangle, \quad (1.57)$$

where in diagrams we have

$$|\Phi[A, B]\rangle = \sum_{m=-\infty}^{+\infty} \left(\overline{v}_L \text{---} \boxed{A_1} \text{---} \boxed{B_k} \text{---} \boxed{A_L} \text{---} v_R \right), \quad (1.58)$$

with the dashed lines on the left and right representing the terms in square brackets in (1.55). Due to the linearity of the tangent vectors in the parameters B , they can be added by adding their parameters

$$|\Phi[A, B]\rangle + |\Phi[A, B']\rangle = |\Phi[A, B + B']\rangle, \quad (1.59)$$

as long as they belong to the same tangent space.

Tangent vectors are invariant under infinitesimal gauge transformations (1.31). Defining

$$g_k(\epsilon) \equiv e^{\epsilon x_k} = \mathbb{I} + \epsilon x_k + \mathcal{O}(\epsilon^2), \quad (1.60)$$

where x_k is an invertible $D \times D$ matrix, an infinitesimal transformation is performed by taking the derivative of the transformed state with respect to ϵ . We find that the infinitesimally transformed state has the form of a tangent vector

$$\left. \frac{\partial}{\partial \epsilon} |\Psi[A'(\epsilon)]\rangle \right|_{\epsilon=0} = |\Phi[A, \tilde{B}]\rangle, \quad \tilde{B}_k^s = A_k^s x_k - x_{k-1} A_k^s, \quad (1.61)$$

which implies an additive gauge freedom in the tangent vector representation

$$|\Phi[A, B + \tilde{B}]\rangle = |\Phi[A, B]\rangle, \quad (1.62)$$

with \tilde{B}_k as defined in (1.61).

Thanks to this freedom, we can restrict ourselves to parameters B_k that satisfy a *gauge-fixing condition*, such as

$$E_{A_k}^{B_k} |r_{k+1}\rangle \equiv \left(\begin{array}{c} \boxed{B_k} \\ | \\ \boxed{A_k} \end{array} \right) \text{---} r_{k+1} = 0 \quad \forall k = 1 \dots L, \quad (1.63)$$

where we have defined a more general transfer matrix E_B^A . This condition additionally implies

$$\langle \Phi[A, B] | \Psi[A] \rangle = 0, \quad (1.64)$$

which is straightforward to see, since every term of $\langle \Phi[A, B] | \Psi[A] \rangle$ contains (1.63) for some value of k . To see that the gauge freedom (1.62), together with (1.64), suffices to implement (1.63), one can insert an infinitesimal gauge transformation into (1.63), using the freedom in x_k to solve the resulting system of equations. This is always possible if the matrix r_k has full rank. For more details see [6, 21, 59].

It is possible to construct B_k that satisfy (1.63), for example using the parametrisation [6]

$$B_k^s(b_k) = l_k^{-\frac{1}{2}} b_k V_k^s r_{k+1}^{-\frac{1}{2}}, \quad (1.65)$$

where b_k contains the physical parameters and has dimensions $D \times D(d-1)$, representing the number of physical degrees of freedom per site (1.32), and $[V_k^s]_{\alpha\beta}$ contains a basis for the null space of the matrix



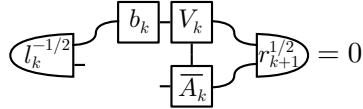
$$, \quad (1.66)$$

where we combine the two legs on the left to make one matrix index, so that



$$= 0. \quad (1.67)$$

The left leg of the V_k tensor has dimension $D(d-1)$ to match b_k . Inserting (1.65) into (1.63) we find



$$= 0 \quad (1.68)$$

due to (1.67).

With gauge fixing (1.63) using the parametrisation (1.65), the overlap of two tangent vectors has the simple form

$$\langle \Phi[A, B(b)] | \Phi[A, B(b')] \rangle = |\mathbb{Z}| \sum_{k=1}^L \text{tr}[b_k^\dagger b'_k], \quad (1.69)$$

where $|\mathbb{Z}|$ is the cardinality of integers, representing the infinite number of blocks in the chain. In practise, we scale the b_k such that $\text{tr}[b_k^\dagger b_k] = 1$ so that the tangent vectors are normalised up to a factor $L|\mathbb{Z}|$, which is the number of sites in the chain.

1.4 Tangent space methods for MPS

In this section we describe the methods used in this thesis, and implemented in the author's software package *evoMPS* [46], for finding variational ground states and low-lying excited states using block-uniform MPS. All these methods make use of the tangent space of Section 1.3.8. We also detail some improvements made to the [46] software for the purposes of the studies in this thesis.

1.4.1 The effective energy gradient

In order to minimise the energy of an MPS given a Hamiltonian H , we compute the effective energy gradient

$$\frac{\partial}{\partial [A_k^{s\dagger}]_{\alpha\beta}} \frac{\langle \Psi[A] | H | \Psi[A] \rangle}{\langle \Psi[A] | \Psi[A] \rangle}, \quad (1.70)$$

which lives in the tangent space (1.55) at $|\Psi[A]\rangle$. We use the gradient to implement two different methods in *evoMPS*:

1. The gradient descent method with small, dynamically adjusted steps and
2. the nonlinear conjugate gradient method [65].

The first method is equivalent to integrating the effective imaginary time evolution of the MPS and was first described for uniform MPS in [6]. The second method was suggested in [66] and implemented in *evoMPS* for [21].

The effective gradient (1.70) can be found by performing the minimisation

$$\min_{[b]} || |\Phi[A, B(b)]\rangle - H |\Psi[A]\rangle ||^2, \quad (1.71)$$

where we use the gauge-fixing parameterisation (1.65). The expression to minimise expands to

$$\begin{aligned} & \langle \Phi[A, B(b)] | \Phi[A, B(b)] \rangle + \langle \Psi[A] | H | \Psi[A] \rangle - \langle \Phi[A, B(b)] | H | \Psi[A] \rangle - \langle \Psi[A] | H | \Phi[A, B(b)] \rangle \\ & = |\mathbb{Z}| \sum_k \text{tr}[b_k^\dagger b_k] - \langle \Phi[A, B(b)] | H | \Psi[A] \rangle + \dots, \end{aligned} \quad (1.72)$$

where we have used (1.69) and in the second line we suppress terms that do not feature b_k^\dagger . We can find the extrema by taking the derivative with respect to b_k^\dagger . First, however, we must ensure that we can compute the overlap $\langle \Phi[A, B(b)] | H | \Psi[A] \rangle$ efficiently. The precise form is dependent on the form of the Hamiltonian. For the numerical work of this thesis, it suffices to treat Hamiltonians consisting of sums of local terms h

$$H = \sum_{n=-\infty}^{+\infty} h_n, \quad (1.73)$$

where h acts on r neighbouring sites. We find

$$\begin{aligned} \langle \Phi[A, B(b)] | h_n | \Psi[A] \rangle = |\mathbb{Z}| \sum_{k=1}^L & \left[\langle l_k | E_{B_k}^{A_k} | K_{k+1} \rangle + \langle K_k | E_{B_k}^{A_k} | r_{k+1} \rangle + \right. \\ & \left. \sum_{j=k-r+1}^k \langle l_j | \mathbf{H}_{j,k}[A, B] | r_{j+r} \rangle \right], \end{aligned} \quad (1.74)$$

where we use the generalised transfer operator from (1.63), $\langle K_k |$ and $|K_{k+1}\rangle$ contain the Hamiltonian terms h_n acting to the left and the right of k , respectively, and $\mathbf{H}_{j,k}[A, B]$

represents overlapping terms in which h_j , which acts on sites j to $j+r-1$, acts on the site k where B_k is present. The middle term with $\langle K_k |$ is zero since we are using gauge-fixed tangent vectors that fulfil (1.63).

We define, for Hamiltonian terms h that act on r adjacent sites, the generalised block transfer matrix

$$\mathbf{H}_{j,k}[A, B] \equiv \left\{ \begin{array}{c} \boxed{A_j} \cdots \boxed{A_k} \cdots \boxed{A_{j+r-1}} \\ \hline \boxed{h} \\ \hline \boxed{\bar{A}_j} \cdots \boxed{\bar{B}_k} \cdots \boxed{\bar{A}_{j+r-1}} \end{array} \right\}, \quad (1.75)$$

where we make the dependence on $[A]$ and $[B]$ explicit to emphasise the B -dependence. The effective right-side Hamiltonian $|K_k\rangle$ is

$$|K_k\rangle \equiv \left(\sum_{n=0}^{+\infty} (\mathbf{E}_k)^n \right) \left[\sum_{j=1}^L E_1 \cdots E_{j-1} \mathbf{H}_j[A] |r_{j+r}\rangle \right], \quad (1.76)$$

where

$$\mathbf{H}_j[A] \equiv \left\{ \begin{array}{c} \boxed{A_j} \cdots \boxed{A_{j+r-1}} \\ \hline \boxed{h} \\ \hline \boxed{\bar{A}_j} \cdots \boxed{\bar{A}_{j+r-1}} \end{array} \right\}. \quad (1.77)$$

Due to the spectral properties of \mathbf{E}_k (see Section 1.3.1), we can write the sum of powers of \mathbf{E}_k in (1.76) as a convergent geometric series plus a projector

$$\begin{aligned} \sum_{n=0}^{+\infty} (\mathbf{E}_k)^n &= \sum_{n=0}^{+\infty} (\mathbb{I} - |l_k\rangle\langle r_k|) (\mathbf{E}_k)^n + |l_k\rangle\langle r_k| \\ &= (\mathbb{I} - |l_k\rangle\langle r_k|) (\mathbb{I} - \mathbf{E}_k)^{\text{P}} + |l_k\rangle\langle r_k|, \end{aligned} \quad (1.78)$$

where $(\mathbb{I} - \mathbf{E}_k)^{\text{P}}$ is a pseudo inverse, needed since $(\mathbb{I} - \mathbf{E}_k)$ does not have full rank. Using this result in (1.76), we have

$$E_{B_k}^{A_k} |K_k\rangle = E_{B_k}^{A_k} (\mathbb{I} - \mathbf{E}_k)^{\text{P}} \left[\sum_{j=1}^L E_1 \cdots E_{j-1} \mathbf{H}_j[A] |r_{j+r}\rangle \right], \quad (1.79)$$

where (1.63) allows us to drop some terms.

We therefore see that the expression to minimise in (1.71) can be broken down into solving

$$\frac{\partial}{\partial b_k^\dagger} \left[\text{tr}[b_k^\dagger b_k] + \langle l_k | E_{B_k}^{A_k} |K_{k+1}\rangle + \sum_{j=k-r+1}^k \langle l_j | \mathbf{H}_{j,k}[A, B] |r_{j+r}\rangle \right] = 0 \quad (1.80)$$

for each $k = 1 \dots L$, which involves only simple linear algebra operations.

Although matrix multiplication in the D^2 -dimensional space of the transfer matrices involves $\mathcal{O}(D^6)$ operations, with matrix-vector multiplication requiring $\mathcal{O}(D^4)$, we can reduce the computational cost to $\mathcal{O}(D^3)$ by contracting the tensor networks involving matrix-vector multiplication in a different order. For example,

$$\begin{aligned}
\mathbf{H}_j[A]|r_{j+r}\rangle &= \begin{array}{c} \begin{array}{c} \boxed{A_j} \cdots \boxed{A_{j+r-1}} \\ \boxed{h} \\ \boxed{\bar{A}_j} \cdots \boxed{\bar{A}_{j+r-1}} \end{array} \end{array} |r_{j+r}\rangle \quad (1.81) \\
&\mapsto \begin{array}{c} \begin{array}{c} \boxed{A_j} \cdots \boxed{A_{j+r-1}} \\ \boxed{h} \end{array} \end{array} \begin{array}{c} \text{---} \boxed{r_{j+r}} \text{---} \\ \text{---} \boxed{\bar{A}_{j+r-1}} \text{---} \\ \text{---} \boxed{\bar{A}_j} \text{---} \end{array} \\
&= \begin{array}{c} \begin{array}{c} \boxed{A_j} \cdots \boxed{A_{j+r-1}} \\ \boxed{h} \end{array} \end{array} \begin{array}{c} \text{---} \boxed{r_{j+r}} \text{---} \\ \text{---} \boxed{A_{j+r-1}^\dagger} \text{---} \\ \text{---} \boxed{A_j^\dagger} \text{---} \end{array} \\
&= \sum_{s_1 \dots s_r=0}^{d-1} \sum_{t_1 \dots t_r=0}^{d-1} \langle s_1 \dots s_r | h | t_1 \dots t_r \rangle A_j^{t_1} \dots A_{j+r}^{t_r} r_{j+r} (A_{j+r}^{s_r})^\dagger \dots (A_j^{s_1})^\dagger,
\end{aligned}$$

where we have again used unravelling (1.27). Note that the pseudo-inversion in (1.79) cannot be reduced to matrix-vector multiplication in its exact form. As such, we must perform it indirectly, obtaining $|K_k\rangle$ as a solution of

$$(\mathbb{I} - |l_k\rangle\langle r_k|)(\mathbb{I} - \mathbf{E}_k)|K_k\rangle = (\mathbb{I} - |l_k\rangle\langle r_k|) \left[\sum_{j=1}^L E_1 \dots E_{j-1} \mathbf{H}_j[A]|r_{j+r}\rangle \right] \quad (1.82)$$

using an iterative solver. Since the right-hand side is constant, the costliest operation performed for each iteration is the matrix-vector multiplication of \mathbf{E}_k with $|K_k\rangle$, which we can do using $\mathcal{O}(D^3)$ operations after unravelling.

Using the unravelled form, we obtain each remaining term in (1.80) as a trace over a matrix expression that is linear in b_k^\dagger , resulting in a closed form for the optimal b_k that minimise (1.71), thus finally obtaining the effective energy gradient in the MPS tangent space. For more details see [6, 21, 59, 61].

It is useful for the purposes of energy minimisation to determine the norm of the effective energy gradient

$$\eta = (\langle \Phi[A, B] | \Phi[A, B] \rangle)^{\frac{1}{2}}, \quad (1.83)$$

where B_k are the optimal tangent vector parameters solving the minimisation problem (1.71).

1.4.2 Improvements for large physical dimensions

In the algorithms of [6, 59, 60] the cost of computations involving the Hamiltonian block transfer matrix (1.77) scales as $\mathcal{O}(d^{2r})$, where r is the range of the interactions in the Hamiltonian, which is clear from the unravelled form (1.81). If the local Hilbert space dimension d is large, this can be the dominant cost in implementing the algorithm, depending on the bond dimension D . This is the case in our numerical study of Chapter 7, in which we use $d \leq 55$. However, very often the Hamiltonian has a tensor product decomposition of the form

$$h = \sum_{m=1}^M \sigma_1^{(m)} \otimes \dots \otimes \sigma_r^{(m)} \quad (1.84)$$

with a small number of terms M , where $\sigma_n^{(m)}$ is an on-site operator acting on site n . Indeed, in Chapter 7 we have $M \leq 4$. By exploiting this structure we can reduce the cost of operations like (1.77) to $\mathcal{O}(Md^2)$. To see this, we rewrite the unravelled form (1.81) as

$$\mathbf{H}_j[A]|r_{j+r}\rangle \mapsto \quad (1.85)$$

where the horizontal legs on the σ operators represent the m index in (1.84). The red dashed line indicates a new way to decompose this network, given that we can decompose h . We can compute the marked inner part independently of the outer part with scaling in M and d of $\mathcal{O}(Md^2)$, resulting in an $MD \times D$ matrix which then forms a component of the next layer, which we also compute with scaling $\mathcal{O}(Md^2)$. Computing the entire network thus scales as $\mathcal{O}(rMd^2)$. The scaling in D is unchanged.

1.4.3 Energy optimisation: Nonlinear conjugate gradient

As noted in Section 1.4.1, we can use the effective energy gradient (1.70) to implement the nonlinear conjugate gradient (CG) algorithm [65, 68], which efficiently minimises functions that are approximately quadratic in their arguments, which is the case for the energy expectation value near to a minimum, where higher order terms can be neglected.

We do not present the full details of the algorithm here, for which one can consult for example [65, 68], as well as [21], which contains an overview of the theory in the appendix. However, since the publication of [21], the author has made a number of improvements to the implementation. For that reason, we first summarise the algorithm here. Starting from some point $|\Psi[A]^{(n)}\rangle$ the algorithm for the n th step is:

1. Compute the energy gradient as a tangent vector $|\Phi[A^{(n)}, B^{(n)}]\rangle$.
2. Compute the factor

$$\beta^{(n)} \equiv \frac{\langle \Phi[A^{(n)}, B^{(n)}] | \Phi[A^{(n)}, B^{(n)}] \rangle - \langle \Phi[A^{(n)}, B^{(n)}] | \Phi[A^{(n)}, B^{(n-1)}] \rangle}{\langle \Phi[A^{(n-1)}, B^{(n-1)}] | \Phi[A^{(n-1)}, B^{(n-1)}] \rangle}. \quad (1.86)$$

3. Calculate the next search direction

$$C_k^{(n)} \equiv -B_k^{(n)} + \text{Re}(\beta^{(n)})C_k^{(n-1)}. \quad (1.87)$$

4. Use a line-search in α to find the energetic minimum of $|\Psi[A^{(n)} + \alpha C^{(n)}]\rangle$.
5. Move to the new position: $A_k^{(n+1)} = A_k^{(n)} + \alpha C_k^{(n)}$.

At the first step $n = 1$ there is not enough information to complete steps 2 and 3. For this reason we further define $C_k^{(1)} \equiv -B_k^{(1)}$.

We now describe the key improvements since [21]. The first is the use of the Polak-Ribière form (1.86) for β rather than the Fletcher-Reeves form [68]. This form involves the term $\langle \Phi[A^{(n)}, B^{(n)}] | \Phi[A^{(n)}, B^{(n-1)}] \rangle$, which involves the tangent vector $|\Phi[A^{(n)}, B^{(n-1)}]\rangle$ formed by using the parameters $B^{(n-1)}$ determined for the tangent space of the previous location $A^{(n-1)}$ as parameters for the *new* tangent space at $A^{(n)}$. In general, even if $B^{(n-1)}$ represented a gauge-fixed tangent vector at $A^{(n-1)}$, it does not do so at $A^{(n)}$. As such we must compute the overlap without the simplifications of gauge fixing of $B^{(n-1)}$:

$$\begin{aligned} & \langle \Phi[A, B] | \Phi[A, B'] \rangle & (1.88) \\ & = |\mathbb{Z}| \sum_{k=1}^L \left(\langle l_k | E_{B'_k}^{B_k} | r_{k+1} \rangle + \langle l_k | E_{A_k}^{B_k} \sum_{m=0}^{+\infty} (\mathbf{E}_{k+1})^m \left[\sum_{j=k+1}^{k+L} E_{k+1} \dots E_{j-1} E_{B'_j}^{A_j} | r_{j+1} \rangle \right] \right), \end{aligned}$$

where B_k is assumed to be gauge-fixed, while B'_k is not. As for (1.76) we can replace the sum to infinity over $(\mathbf{E}_{k+1})^m$ with a pseudo-inverse term, giving

$$\begin{aligned} & \langle \Phi[A, B] | \Phi[A, B'] \rangle & (1.89) \\ & = |\mathbb{Z}| \sum_{k=1}^L \left(\langle l_k | E_{B'_k}^{B_k} | r_{k+1} \rangle + \langle l_k | E_{A_k}^{B_k} (\mathbb{I} - \mathbf{E}_{k+1})^P \left[\sum_{j=k+1}^{k+L} E_{k+1} \dots E_{j-1} E_{B'_j}^{A_j} | r_{j+1} \rangle \right] \right), \end{aligned}$$

which we can compute efficiently.

Making further use of tangent vector overlaps, we also use the gradient in the search direction to detect the minimum during the line search of step 4. At each trial value of

α , we compute the effective energy gradient $|\Phi[A(\alpha), B(\alpha)]\rangle$, where $A_k(\alpha) = A_k^{(n)} + \alpha C_k^{(n)}$, and compute its component along the search direction

$$H'(\alpha) \equiv \partial_\alpha \langle \Psi[A(\alpha)] | H | \Psi[A(\alpha)] \rangle = \langle \Phi[A(\alpha), C^{(n)}] | \Phi[A(\alpha), B(\alpha)] \rangle, \quad (1.90)$$

where we define $H(\alpha) \equiv \langle \Psi[A(\alpha)] | H | \Psi[A(\alpha)] \rangle$. $H'(\alpha)$ goes to zero at the minimum, as well as indicating in which direction the minimum lies. To compute the overlap between tangent vectors, we must again take into account that $C^{(n)}$ will no longer represent a gauge-fixed tangent vector at point $A(\alpha)$, using (1.89).

Although computing the gradient incurs additional computational costs compared to just computing the energy expectation value, it enables more reliable convergence of the line search. For the latter we use Brent's method [65, 69], a root-finding method implemented in the Scipy [70] software package that combines bisection searching and quadratic interpolation, to search for a root in the gradient (1.90). Brent's method depends on *bracketing* the solution: Finding at least one point on either side of it. For bracketing, we first ensure our starting point $\alpha = 0$ has negative gradient, taking an initial step $\alpha = \alpha_0$ and using polynomial extrapolation (up to degree 3) based on all collected data points, recursively, to locate the first point of positive gradient.

During the entire line search process, including initial bracketing, we check the Wolfe conditions [68] to determine if we have already found a *good enough* step size such that it would be beneficial to abort early. The Wolfe conditions are

$$H(\alpha) \leq H(0) + c_1 \alpha H'(0), \quad (1.91)$$

$$H'(\alpha) \geq c_2 H'(0), \quad (1.92)$$

which ensure that the energy has decreased, and that the gradient has increased, such that $H(\alpha)$ is minimised “sufficiently”. We follow [68] in using $c_1 = 10^{-4}$ and $c_2 = 0.1$ for a line search in the nonlinear conjugate gradient algorithm. Aborting the line search when the Wolfe conditions are fulfilled brings huge savings in computational efficiency, justifying computing the gradient at each point. In practise, it is often favourable to abort after the first step α_0 , for which we use the successful step length from the previous iteration, as long as it falls within reasonable bounds.

Throughout the line search process, we also store data about each visited value of α , including results of iterative parts of the algorithm used to compute the effective gradient (see Section 1.4.1). We use the latter as initial values for the same iterative parts of the algorithm when visiting nearby values of α . This provides further efficiency gains.

In theory, the nonlinear conjugate-gradient converges in a few steps along a set of “mutually conjugate” directions if the function to optimise is quadratic. In practise, higher-order corrections to the function, limited numerical precision, and early abortion of the line search due to the Wolfe conditions being satisfied, mean the search directions become less optimal with each iteration, such that one must eventually discard the previous search direction and *restart* the algorithm [65, 68]. We implement a number of triggers for a restart:

1. Value of β becomes very large ($\beta > 100$).
2. Positive energy gradient in line-search direction at $\alpha = 0$.

3. Failure to find a root of the gradient in the line search (including failure to find a valid bracket).
4. Maximum number of steps (usually 20) since last restart exceeded.

Between restarts we *do not* restore a canonical form for the MPS (see Section 1.3.4). This is because restoring a canonical form, which is achieved by means of a gauge transformation, shifts the parameter space in a way unaccounted for by the CG algorithm. We inevitably drift away from a canonical form since finite steps along tangent-vector directions in parameter space, such as those performed during the line search, generally include gauge transformations. This is because even gauge-fixed tangent vector parameters that fulfil (1.63) only fix the gauge for an infinitesimal step. However, performing a gauge transformation constitutes a “change of basis” in parameter space that damages the approximate conjugacy between successive search directions in the CG algorithm. Unfortunately, not restoring a canonical form risks poor conditioning of the l_k and r_k matrices (see Section 1.3.4), such that we must set an upper limit on the number of steps between restarts, when we may perform gauge transformations without concern, since all data on previous CG steps is discarded.

As a final note, we find that it is beneficial to precondition the state prior to starting the CG algorithm. This is especially important when beginning from a *random* state. To do this, we perform imaginary time evolution [6] by stepping along the effective energy gradient up until the norm (1.83) of the gradient has dropped below a certain threshold, say $\eta < 0.01$.

1.4.4 Automatic adjustment of block length

The block length L of a block-uniform MPS is set prior to any variational optimisation — it is not a free parameter and we must set it prior to, for example, energy minimisation. In this case, if the block length is not a multiple of the true periodicity of the ground state, one possible consequence is that the optimisation produces an approximately degenerate largest eigenvalue of the block transfer matrix \mathbf{E} , defined in (1.18). Such a degeneracy represents infinite-range correlations and invalidates the assumptions we made in Section 1.3.1, such that we can no longer neglect the infinitely distant boundaries of the system. It happens when the variational optimisation “tries” to build a superposition of translated states that restores invariance under translations by the block length L .

Fortunately, it is easy to detect this scenario by tracking the difference between the two largest eigenvalues of \mathbf{E} , increasing the block size if it falls below a threshold. At least for the case of a Hamiltonian with a spectral gap between the ground state and the first excited state, this is normally enough to avoid choosing an inappropriate block size. In gapless phases finite-entanglement effects can cause the true translation-symmetry of the ground state to be disguised in the effective energy landscape: See Section 2.3.2.

1.4.5 Excitations

We use the excitations ansatz of [60, 62] to compute low-lying excitations using the MPS tangent space at the MPS ground state. This means first finding a ground state using, say the CG algorithm described in Section 1.4.3, then using the tangent vectors (1.57) to represent small perturbations. Tangent vectors are known to accurately represent excitations that are not part of a continuous section of the energy spectrum [62].

Here, we briefly sketch the procedure: Having found an MPS ground state $|\Psi[A]\rangle$, we can write a variational Hamiltonian, using the tangent vectors as trial states, as a matrix in terms of the tangent vector parameters as

$$b^\dagger \mathbf{H} b' \equiv \langle \Phi[A, B(b)] | H | \Phi[A, B(b')] \rangle, \quad (1.93)$$

where we use the gauge-fixing parameterisation (1.65) to reduce the number of parameters and to avoid unnecessary calculations. The matrix-vector multiplication $\mathbf{H} b'$ can be computed using the methods described in Section 1.4.1 with scaling in the bond-dimension $\mathcal{O}(D^3)$. From (1.69), we know that the parameters b form an orthonormal basis for the tangent space. This means we can find variational excited states by applying a standard eigensolver to \mathbf{H} . To do this efficiently, we use a sparse eigensolver such as the Arnoldi method [70, 71] that requires only matrix-vector multiplication.

Although this excitations ansatz is generally applicable to block-uniform MPS, *evoMPS* currently only implements it for $L = 1$. This is all that is needed for the purposes of this thesis, and it is always possible, at the cost of increased local Hilbert space dimension, to use blocking to convert any block-uniform MPS into one with $L = 1$ (see Section 1.3).

1.4.6 GPGPU acceleration of computations

The majority of computational time required to execute algorithms like the CG method of Section 1.4.3 and the excitations method of Section 1.4.5 is spent performing matrix-matrix multiplication of $D \times D$ matrices, requiring $\mathcal{O}(D^3)$ floating-point arithmetic operations. This is the optimal scaling in $\mathcal{O}(D^3)$, and it is possible because the tensor networks involved in computing expectation values can be unravelled into a sum over the trace $D \times D$ matrix products, as noted in Section 1.4.1.

In recent years, producers of graphical processing units (GPUs) have produced computing hardware targeted at highly-parallel computational-science applications. These general-purpose GPUs (GPGPUs) consist of a large number of simple processing units that can work on small parts of a computation in parallel [72]. As such, they are well-suited to performing matrix-multiplication on large matrices. During the research period leading up to this thesis, the author added GPGPU versions of the iterative parts of the CG and excitations algorithms to *evoMPS* [46], which exploit GPGPUs from the manufacturer NVIDIA via the PyCUDA [73] and scikit-cuda [74] packages for Python. These were particularly useful for the numerics of Chapter 7, which involved large local Hilbert-space dimensions (d up to 55) as well as relatively large bond-dimensions D up to 256. The calculations were carried out on NVIDIA Tesla K20 GPGPU devices [72].

Chapter 2

Phases and phase transitions

2.1 Introduction

In nature, we find that the properties of substances react largely smoothly to changes in a control parameter, such as temperature, pressure or magnetic field strength. A heated gas increases in volume as a smooth, analytic function of the temperature, for example. However, we also encounter sudden, often dramatic changes in properties, such as when we reduce the temperature of water to the point where it condenses to form a solid. We call the regimes of smooth behaviour “phases” and sudden, nonanalytic changes “phase transitions”. In an ideal setting, phase transitions occur at isolated points or lines in parameter space where the nonanalyticity is present.

In order to distinguish between phases, it is often possible to define an *order parameter*, which is usually a measurable quantity that distinguishes between phases by, for example taking the value zero in one phase and a nonzero value in another. In the ferromagnetic transition, for example, the order parameter is the magnetisation [75]. Sometimes, quantities that would be very difficult to measure are used as order parameters if they are easily accessible in, say, numerical simulations.

In this chapter, we define the types of phase transition that are important for the systems studied in this thesis, describing their key characteristics. The transitions we concern ourselves with occur in quantum lattice systems and are all zero-temperature phase transitions, which in quantum mechanics have a rich theory owing to the possibility of entanglement in the ground state. We discuss their signatures in terms of quantities that can be extracted easily from a matrix product state (MPS) representation of the ground state.

2.2 Types of phase transition

Phase transitions are often divided into two main types: First-order transitions and continuous transitions (which includes Berezinskii-Kosterlitz-Thouless transitions) [75, 76]. Both involve points of nonanalyticity in a physical quantity as a function of a system parameter (this means the function cannot be written as a convergent power series at this point).

Since we are interested in zero-temperature phenomena, we follow [76] and define a phase transition as a point of nonanalyticity in the ground state energy density of a system as a function of a control parameter, such as the external magnetic field strength. However, we also discuss thermal phase transitions briefly in the following, as their physics is often intimately related to that of zero-temperature transitions.

Note that there are transitions that do not fall into the categories listed here. See for example [77].

2.2.1 First order

First-order transitions involve a discontinuous change in system properties, such as the discontinuous change in volume of (uniformly) melting ice [75]. Such transitions can occur at zero temperature in response to a change in a control parameter, and can occur in finite or infinite systems. At zero temperature, they result from a level-crossing between the ground state and the first excited state, which may have different properties to the ground state [76]. The level crossing results in a discontinuous first derivative of the ground state energy with respect to the control parameter.

The details of a first-order transition are case-dependent — they are determined by the particular properties of the states that exchange energy levels. It is usually possible to determine, for each case, an order parameter that can distinguish between the phases.

2.2.2 Continuous phase transitions

A large number of transitions, called *continuous* phase transitions, are characterised by scale-invariant fluctuations [76]. By this we mean that, at length scales significantly larger than the lattice spacing, correlation functions are invariant under spatial scaling transformations

$$x \mapsto cx, \tag{2.1}$$

where c is a scaling factor. In all the cases studied here, certain correlation functions (1.4) at continuous transitions have the asymptotic form

$$C(x) \sim x^{-\eta}, \tag{2.2}$$

which only changes by a factor under (2.1). This is usually referred to as “power-law” or “algebraic” decay of correlations. In contrast, if scale-invariance does not hold, correlations typically decay exponentially

$$C(x) \sim e^{-\frac{x}{\xi}}, \tag{2.3}$$

where ξ is the *correlation length*, which represents a natural length scale for the system. Such a scale does not exist if the system is scale-invariant, where (2.2) implies that the correlation length diverges

$$\xi \rightarrow \infty. \tag{2.4}$$

This state of affairs is called *criticality* and the points at which such phase transitions occur are called *critical points*. Since they involve correlations, continuous transitions can only occur either at nonzero temperature, where thermal fluctuations are present, or where the

spatial degrees of freedom are *entangled*. Zero-temperature continuous transitions are often called “quantum phase transitions” since, in this case, if we consider only pure quantum states, the only available correlations are due to the quantum phenomenon of entanglement. A well-known example of a *thermal* continuous transition is the ferromagnetic transition: At the Curie temperature, fluctuating magnetic domains occur at all length scales and the magnetic susceptibility diverges.

An analogous quantum phase transition occurs in the one-dimensional transverse field Ising model

$$H_{\text{Ising}} = -J \sum_{n=1}^{N-1} \sigma_n^z \sigma_{n+1}^z - h \sum_{n=1}^N \sigma_n^x, \quad (2.5)$$

which is defined for the lattice-system Hilbert space of N qubits $\mathcal{H} = \bigotimes_{n=1}^N \mathbb{C}^2$. The σ are the Pauli operators. At $|h|/J = 1$ the Ising model undergoes a continuous phase transition between a small h phase and a large h phase. We present more details on the Ising model and its transition in Section 2.2.3.

Conformal field theories

Often, the physics of a system is not only scale invariant at criticality, but is also invariant under *conformal* transformations, which are those that preserve angles locally. The system then has a description as a conformal field theory (CFT) [76, 78]. In one-dimensional quantum, or two-dimensional classical systems, the CFT is a Lorentz-invariant field theory in two spacetime dimensions. The physics of a 2D CFT is highly constrained by the conformal symmetry and a large set of such theories can be classified by a single number known as the *central charge*. This can be determined from numerical simulations, for example using matrix product states, as described in Section 2.3.2.

Conformal field theory allows many properties of low-dimensional continuous phase transitions to be determined, at least for those transitions that have conformal invariance [78].

Finite systems, the spectral gap, and entanglement

Clearly, due to (2.4) continuous phase transitions can only occur in infinite systems. In finite systems at zero temperature, they manifest themselves as “avoided” energy level crossings, where the gap between energy levels goes to zero in the limit of infinite system size [76]. Indeed, in quantum systems, scale-invariance implies the closing of the spectral gap in the system Hamiltonian, that is, the gap between the ground state and the first excited state. This is because a nonzero gap would represent a natural energy scale, breaking scale invariance. In critical systems the spectrum is continuous so that excitations with arbitrarily small energy are available. The system is then said to be *gapless*. Regions in which there is a spectral gap, called *gapped* phases, have exponentially decaying correlations as in (2.3), as proven in [47, 79]. Note that these statements refer to the low-energy spectrum of the theory. In a lattice system, the lattice will break scale-invariance at sufficiently high energies.

Another interesting property of one-dimensional quantum phase transitions described by 2D CFT’s is that, at the critical point, the entanglement entropy $S(L)$ (defined in (1.8))

of a region of the system with length L diverges as a function of L [53]. This is in contrast to gapped phases of one-dimensional systems, where S has been proven to remain finite for a large class of systems [48, 51]. In gapped phases of systems with more than one dimension, $S(L)$ generically diverges, although it obeys an “area law” in many cases (see Section 1.2.1).

Universality and the quantum-to-classical mapping

Crucially, the physics of systems in the vicinity of a continuous phase transition tends to be independent of microscopic details of the model, since it is dominated by scale-invariant effects, which can only emerge at scales far beyond the lattice spacing. As a result, transitions in models with very different microscopic details can often be described by very similar relations — a phenomenon known as *universality* [76, 78]. For example, the correlation length might obey a power law

$$\xi^{-1} \sim |\lambda_c - \lambda|^\nu \quad (2.6)$$

where λ is some system parameter, the phase transition occurs at the critical point λ_c , and the *critical exponent* ν is *universal*, that is, shared by transitions in a large class of models. Such classes are called *universality classes*. Universality can be understood in terms of *renormalisation* [76, 80], which we briefly discuss in Section 6.7.3. Note that the central charge of the CFT describing the phase transition point is, where applicable, also a universal quantity.

Intriguingly, due to universality, quantum phase transitions often fall into the same universality classes as thermal continuous phase transitions in classical systems [76]. That this should be so can be seen by comparing the path-integral expressions for quantum ground state expectation values with classical partition functions: In a number of cases, the ground state of a quantum system in d spatial dimensions can be related to a well-understood classical system in $d + 1$ spatial dimensions [76]. Roughly speaking, the time dimension of the quantum system, which is continuous, becomes an additional spatial direction when the path integral is interpreted as a partition function. By discretising this new dimension, we obtain a classical lattice system. Since the discretisation constitutes a microscopic change, it tends to be irrelevant to the long range fluctuations that dominate the physics of the transition.

A well-known example of this “quantum-to-classical mapping” maps the one-dimensional quantum Ising model in a transverse field (2.5) to the two-dimensional classical Ising model [76]. The latter has a thermal continuous phase transition, while the former has a quantum phase transition as a function of the external field strength. The transverse field of the quantum system plays an analogous role to the temperature in the classical system, as both serve to introduce fluctuations in the magnetisation. See [76, 81] for more details on quantum-to-classical mappings.

2.2.3 Second-order phase transitions

Often, in the context of phase transitions “second-order phase transition” is used as a synonym for “continuous phase-transition”. In this thesis, we use “second-order” to refer to

the type of continuous phase transition for which the correlation length ξ diverges according to a power law as in (2.6).

In the thermal case, second-order transitions often involve a divergence in the second derivative of the free energy density (the specific heat) [75, 78]. In quantum transitions that are related to classical transitions via a quantum-to-classical mapping, the free energy density corresponds to the ground state energy density [76]. As such, we expect the second derivative of the ground state energy density to diverge in these cases. Notably, this does not occur for the BKT transitions described in Section 2.2.4. We may use the signature of such a divergence to locate second-order transitions, as described in Section 2.3.

Symmetry breaking, order parameters and Landau theory

Since continuous phase transitions are insensitive to the microscopic details of a system, the “sudden changes” in system properties associated with them must occur in macroscopic observable quantities. The best-known examples involve a global *symmetry* of the system [76], which is a transformation that acts on the entire system simultaneously, such as “flipping all spins” in a spin system. Under this symmetry transformation, the physics of one phase, known as the *symmetric* phase, is invariant, while that of the other *symmetry-broken* phase is not. Such a transition is called a *symmetry-breaking* transition. The order parameter for a symmetry-breaking transition involving a global symmetry can be chosen to be *local*, meaning that only a small region of the system need be measured to determine the phase. For example, measuring the magnetisation in a small region is sufficient to determine if symmetry is broken in a uniform magnetic system.

In case of a quantum system we can represent a symmetry as a unitary operator $U = U^\dagger$ that commutes with the Hamiltonian

$$[H, U] = 0. \quad (2.7)$$

We ignore for our purposes the possibility of antiunitary symmetries, such as time reversal. Importantly, that H is invariant under U does not imply that all eigenstates are invariant. Let us take the one-dimensional quantum Ising model, whose Hamiltonian (2.5) commutes with a global spin flip

$$U = \bigotimes_{n=1}^N \sigma_n^x. \quad (2.8)$$

In the absence of an external field ($h = 0$), the ferromagnetic nearest-neighbour interaction in (2.5), $-J \sum_n \sigma_n^z \sigma_{n+1}^z$ (with $J > 0$), leaves two orthogonal possibilities for the ground state

$$|\psi\rangle_\uparrow \equiv |\dots \uparrow\uparrow\uparrow \dots\rangle \quad \text{or} \quad |\psi\rangle_\downarrow \equiv |\dots \downarrow\downarrow\downarrow \dots\rangle, \quad (2.9)$$

where $|\uparrow\rangle$ and $|\downarrow\rangle$ form the orthonormal eigenbasis for σ^z , and it is easy to check that $H_{\text{Ising}}(h = 0)|\psi\rangle_{\uparrow,\downarrow} = -J|\psi\rangle_{\uparrow,\downarrow}$. We find that these ground states are not individually invariant under U

$$U|\psi\rangle_\uparrow = |\psi\rangle_\downarrow, \quad (2.10)$$

although the *space* of ground states is invariant, since the basis states transform into each other. This degenerate eigenvector subspace is characteristic of a *symmetry-broken* phase

and is indeed the only way eigenstates of H can break the symmetry, given (2.7). Note that the ground-state degeneracy is equal to the dimension of the symmetry group, which is \mathbb{Z}_2 for a spin-flip, and has dimension 2. This is also a generic feature of symmetry-broken phases.

In the limit $h \rightarrow \infty$ of infinite field strength, the Ising model has a unique ground state

$$|\psi\rangle_+ = |\cdots + + + \cdots\rangle, \quad (2.11)$$

where $|+\rangle \equiv \frac{1}{\sqrt{2}}(|\uparrow\rangle + |\downarrow\rangle)$ is the eigenstate of σ^x with eigenvalue 1, so that $H_{\text{Ising}}(h \rightarrow \infty)|\psi\rangle_{\uparrow\downarrow} = -h|\psi\rangle_{\uparrow\downarrow}$. We find

$$U|\psi\rangle_+ = \left(\bigotimes_{n=1}^N \sigma_n^x \right) |\cdots + + + \cdots\rangle = |\psi\rangle_+, \quad (2.12)$$

which is characteristic of a *symmetric* phase.

Some kind of phase transition must exist between these two limits, as the ground state degeneracy can only change discontinuously. Indeed, the Ising model undergoes a second-order quantum phase transition at the critical point $|h|/J = 1$ [76].

An approximate theory of continuous, symmetry-breaking phase transitions of classical systems was developed by Landau in the 1930's [82, 83]. Landau theory has been instrumental in understanding this phenomenon, helping to explain universality and successfully predicting critical exponents in many cases. Many results carry over, via the quantum-to-classical mapping, to quantum systems. However, the “mean-field” approximation made by Landau, which ignores fluctuations, can lead to false predictions [76]. Landau theory also assumes a global symmetry and a local order parameter. At least in the quantum case, not all symmetry-breaking transitions have corresponding local order parameters. In Chapter 5 we provide examples of systems with nonlocal, string order parameters that are related, via a unitary *duality* transformation, to systems with local order parameters that fit the Landau paradigm.

2.2.4 Berezinskii-Kosterlitz-Thouless transitions

There is another important kind of continuous phase transition, which occurs in one-dimensional quantum (two-dimensional classical) models with a *continuous* symmetry. It has been proven quite generally, that these systems cannot undergo symmetry breaking (a ground state cannot break the continuous symmetry) in the presence of fluctuations, either quantum or thermal [84, 85]. However, such systems may still possess a continuous transition, as discovered by Kosterlitz and Thouless, as well as Berezinskii, in the early 70's [86, 87]. They found a type of transition in which the correlation length diverges *exponentially* as

$$\xi \sim \exp \left[b \left(\frac{\lambda - \lambda_c}{\lambda_c} \right)^{-1/2} \right], \quad (2.13)$$

where λ_c marks the phase transition point between a phase with a spectral gap (a “gapped” phase) and a *gapless phase* — a phase in which the system remains critical, in the sense

that the correlation length stays infinite and the spectral gap is always closed. The entirety of this phase is described by a CFT. We call such a transition a Berezinskii-Kosterlitz-Thouless (BKT) transition. BKT transitions are also peculiar in that the nonanalyticity in the ground state energy density is expected to be an essential singularity [87], so that no derivative of the energy diverges. Hence, BKT transitions are sometimes called “infinite order”.

A prototypical model with a BKT transition is the 2D classical XY model [88], but there is also good evidence for its occurrence in the p -clock model (3.46) for $p \geq 5$ and it has been found in other models possessing a $U(1)$ symmetry [76]. We study the 1D quantum versions of both models, related to the classical models via a quantum-to-classical mapping [76], in this thesis: The ANNNC model of Chapter 5 is a generalisation of the clock model and the $O(2)$ rotor model of Chapter 7 is, in its classical variant, equivalent to the XY model.

2.2.5 Incommensurate order

Another interesting type of continuous phase transition, which we encounter in Chapters 5 and 4, is the commensurate-incommensurate (C-IC) transition between phases in which the order parameter correlation function oscillates in space with a period that is commensurate with the underlying lattice, and phases in which correlation functions oscillate with a period that can be incommensurate with the lattice. The term “incommensurate” refers to the spatial periodicity taking irrational values when expressed as multiples of the lattice spacing a , implying that the pattern never repeats on a lattice site. For a review of incommensurate order, see [89].

In the cases we study, the C-IC transition is a second-order quantum phase transition of a one-dimensional system. It separates a commensurate gapped phase from an incommensurate gapless phase in which the order parameter correlation function takes the form

$$C(x) \sim x^{-\eta} \cos(kx + \phi), \quad (2.14)$$

where ϕ is a phase shift and the modulation wavevector k varies continuously as a function of the control parameters, thus also taking on irrational values. This gapless phase is called a “floating” phase, referring to the intuition that, in such a phase, spatial structures must be effectively “detached” from the lattice so that they are no longer constrained by its period. One can imagine these structures “floating above” a lattice potential. It is then also natural to suppose that the continuum of excitations making up the spectrum corresponds to arbitrarily-sized translations of these floating spatial structures.

A prototypical model exhibiting a C-IC transition is the axial next-nearest-neighbour Ising (ANNNI) model (5.5), which is a special case of the “ANNNC” model studied in Chapter 5. The ANNNI model possesses a gapped incommensurate phase, sometimes called a liquid phase, adjoining the gapless, floating phase. The transition between these two phases is a BKT transition [43, 90].

2.3 Sketching phase diagrams using MPS

Being able to easily obtain an approximate phase diagram for a quantum system is of great utility. It forms a basis for more detailed investigations of a model, or may be used as a prediction for experiments. Certain phases of matter are also potentially of great practical value, such as superconducting phases.

In this section, we discuss our employment of numerical matrix product state (MPS) methods for “sketching” phase diagrams for one-dimensional quantum systems. This involves computing approximate ground states in block-uniform MPS form, using the variational method described in Section 1.4.3, along lines in the parameter space of the model in question. We then examine a number of quantities that are easily obtainable from the MPS (see Section 1.3), as a function of the parameters, for indications of phase transitions. This allows us to locate transitions, after which we attempt to characterise the phases found. We mitigate errors due to finite entanglement effects by looking for consistency between different transition indicators and plausibility of the emerging phase diagram structure. As well as line scans, we also make limited use of *finite entanglement scaling* (FES) to separate gapped and gapless phases, which further aids consistency checks. We apply these techniques in Chapters 4, 5 and, to a lesser extent, Chapter 7.

2.3.1 Scanning lines in parameter space

We build up a phase diagram sketch from *line scans*. That is, we visit, in order, a finite number of points belonging to an interval of interest along a line in parameter space, finding an MPS ground state at each point, with a fixed bond-dimension D , and recording the values of various quantities of interest. In a parameter space with two or more dimensions, we scan many lines to build up a grid of approximate ground states. We converge each state past some threshold value of η , the norm of the effective energy gradient (1.83).

To efficiently find MPS ground states along a line, we make use of the ground state from the previous point as an initial state for the next point along the line. Within a single phase, this speeds up the scan immensely, since the previous state is usually similar to the next. However, this recycling of states can also cause hysteresis effects because there are cases where the previous state is, at least approximately, a stationary point in the effective energy landscape that is not the ground state. We cannot distinguish such a state from the ground state because η is close to zero in both cases. This is clearly a possibility at a first-order transition, where ground states and first excited states cross over: When passing the transition, the previous ground state approximates the new first excited state well, and may be a local energetic minimum due to finite entanglement effects (see Section 1.4.1). We can thus end up “stuck” in the excited state until we reach a point where the gradient increases beyond our convergence threshold. To mitigate hysteresis effects, we scan along lines in both directions, taking the lowest energy result at each point as the better approximation to the ground state.

The quantities of interest we record for each ground state are the energy density and its derivatives with respect to the line parameter, the half-chain entanglement entropy, the correlation length and, if known, the expectation value and correlation functions of

order parameters for indications of a phase transition. These tend to exhibit discontinuous or nonanalytic behaviour near a phase transition in a way that approximates the exact behaviour of these quantities.

Note that, in fixing the MPS bond dimension D for a line scan, we are neglecting correlations that may be important for a good approximation to the ground state (see Section 1.3.7). This is analogous to the mean-field approximation, in which correlations are also neglected [76]. In the 1D quantum setting, mean-field theory corresponds to using MPS with $D = 1$, which prevents any quantum correlations, as implied by (1.51). Since we generally use $8 \leq D \leq 32$ for our line scans, our approximate phase diagrams can be much more accurate than those obtained using mean-field theory. Indeed, in principle we are able to adjust the amount of entanglement available in the MPS by altering D as needed to obtain the required level of accuracy. This also opens up the possibility of examining how quantities scale with D , which can reveal more information about phases than a line scan. This is known as *finite entanglement scaling* (FES), and is discussed in Section 2.3.2.

Despite the ability to increase entanglement as needed, it is important for the interpretation of line-scan data to consider what kind of effects a fixed, finite D can have on the behaviour of quantities near phase transitions. In fact, in uniform MPS at fixed D , nonanalytic behaviour can occur not only due to the presence of a genuine phase transition of the system, but also purely as an artifact of finite entanglement. Indeed, such effects can shift the apparent location of a phase transition away from its physical location in parameter space [21, 41] or lead to nonphysical symmetry-breaking in a gapless phase [91–93]. For this reason, we refer to nonanalytic behaviour in finite- D uniform MPS as a *pseudo-transition*, which may or may not correspond to a true transition in the model. That finite entanglement effects can lead to pseudo-transitions seems natural when we consider that they modify the effective energy landscape — the effective ground state for MPS with a particular D is generally not the exact ground state, and can differ from it in unexpected ways. For example, a lower energy state from one symmetry sector may become inaccessible due to finite entanglement, such that a state with less entanglement from another symmetry sector is favoured [21]. By using FES together with line scans, looking for consistency of pseudo-transitions in different physical quantities as well as in the data from neighbouring line scans, and by judging the plausibility of the emerging phase structure on physical grounds, we hope to avoid being misled by finite entanglement artifacts.

We now describe in more detail the various phase-transition indicators we use to obtain transition locations from line scans.

Energy density and derivatives

Given that our MPS effective ground states are close to the true ground state, the ground state energy density $\langle h \rangle$ is one of the best-approximated quantities available: The energy converges to the minimum of the finite- D *effective* energy landscape quadratically in η , the norm of the effective energy gradient (see Section 1.4.1), since near the minimum higher order terms in the Taylor expansion of the energy become irrelevant. This implies that errors due to poor convergence of the MPS ground state are less important here. The same is not true, however, for any error due to insufficient entanglement in the approximation.

First-order phase-transitions can be detected by looking for discontinuities in the first derivative with respect to the line-scan parameter (see Section 2.2.1), after eliminating hysteresis effects. The first derivative can be obtained from the state directly due to the so-called Hellmann-Feynmann theorem (see, for example [94]), which states that $\frac{d}{dg}\langle\psi|H|\psi\rangle$ can be computed as an expectation value of $\frac{d}{dg}H$ for eigenstates $|\psi\rangle$ of H , or of the effective, variational Hamiltonian. Since first-order transitions between gapped phases do not involve an increase in entanglement near the transition, we can often obtain their location to high precision using MPS.

Second-order transitions (see Section 2.2.3) can be detected by examining the second derivative of $\langle h\rangle$, which we approximate using finite-differences of the first derivative. In the Ising case, as well as others, this diverges at the transition, and we expect signs of divergence to show up in finite- D MPS, such as a clear cusp minimum. We confirm this expectation by testing on models, such as the Ising model or the three-state Potts model (see Figure 5.7), where the location of a second-order transition is known.

Half-chain entanglement entropy

As described in Section 2.2.2, the half-chain entanglement entropy S_{half} is finite in gapped phases and diverges on approaching criticality. As such, it is a good indicator of phase transitions involving at least one gapped phase in one-dimensional systems. However, it is also strongly impacted by the restriction to finite- D MPS (see Section 1.3). Nevertheless, S_{half} will be small when the exact ground state is close to a product state and large when the system is critical, as the MPS attempts to approximate a state with $S_{\text{half}} \rightarrow \infty$. As such, a finite- D plot of S_{half} in parameter space provides a useful outline of the possible location of gapped and gapless regions. Like the second energy derivative, it shows signs of divergence at a second-order transition between gapped phases, exhibiting a cusp peak in known cases (for the Potts model, see the $p = 3$ case of Figure 5.7).

Interestingly, in known cases of BKT transitions from gapped into gapless phases (the clock model — see Section 5.3.2), we observe that S_{half} also sometimes shows a peak (see Figure 5.7). This peak appears to coincide with the (presumably nonphysical) occurrence of symmetry-breaking.

Correlation length

The correlation length ξ is another useful indicator of transitions that is easy to obtain for a uniform MPS (see Section 1.3.5). We consider its inverse $1/\xi$, the exact value of which goes to zero at criticality (see Section 2.2.2). The finite- D MPS approximation prevents our numerical value of $1/\xi$ from becoming zero but, it tends to show signatures of nonanalyticity at second-order phase transitions, where it typically hits a cusp minimum (again, see Figure 5.7).

At BKT transitions $1/\xi$ is still useful as an indicator of where the gapless phase is located but, due to its exponential behaviour in the absence of approximations (see Section 2.2.2), it is less useful for locating the transition point. To fit the expected scaling using numerical

data in such a way as to obtain a good estimate of the transition location would require performing FES for a large number of points.

Modulation wavevector

Since we can obtain the wavevector of dominant correlation functions from the MPS transfer matrix (see Section 1.3.6), we may use the appearance and disappearance of modulations to indicate a change of phase. At a C-IC transition (see Section 2.2.5) the modulation wavevector of the order parameter correlation function exhibits a power-law behaviour as a function of the system parameter [89] which can be observed in the MPS approximation. For examples of this, see Figures 5.4 and 5.5.

Order parameter

If we know, or can identify, an order parameter for a particular transition, its expectation value can also be used to locate it. How easy it is to precisely locate the transition depends to some extent on the order parameter critical exponent [21], but for a phase-diagram sketch this is less important, where we make use of it together with other indicators in order to build up evidence for a transition. Since it is typically zero in one phase and nonzero in another, one does not need excessive precision to distinguish those phases using its MPS approximation.

2.3.2 Finite Entanglement Scaling (FES)

Finite entanglement scaling describes how physical quantities scale with respect to an “entanglement cutoff”, such as the MPS bond dimension D , which limits the half-chain entropy as in (1.51). Since the MPS ground state tends towards the true ground state as $D \rightarrow \infty$, we expect any physical quantity to tend towards its exact value as we increase D (although there is also some error from imperfect convergence of the energy minimisation). Furthermore, in the case where the exact ground state is described by a CFT (see Section 2.2.2) there is a simple prediction for the scaling of the correlation length ξ and the half-chain entropy S_{half} with the bond dimension, which allows us to extract the central charge of the CFT from a set of ground states with varying D .

The result in question, due to Calabrese and Cardy [53, 95], is a prediction for the half-chain entropy “near” a critical point described by a CFT

$$S_{\text{half}} \sim \frac{c}{6} \log \xi, \tag{2.15}$$

where ξ is the correlation length and c is the central charge. The underlying assumption is that the state is sufficiently close to the CFT ground state so that it can still be described by a relativistic (massive) quantum field theory. It is also assumed that ξ is large compared to the lattice spacing a . It is natural to ask whether a uniform MPS approximation to the ground state fulfils these criteria sufficiently well. Indeed, this relation has recently been tested with MPS (and DMRG) data [41, 42] on models where the CFT describing the critical system is known, finding good agreement.

Since, in the kind of systems we examine, gapless points, lines and phases tend to be described by a CFT, testing (2.15) is a useful way of checking for gaplessness. In a gapped phase, both ξ and S_{half} will show saturation as D is increased as they both tend towards their exact, finite values (see Section 2.2.2) and will fail to obey (2.15). Because (2.15) can only be fulfilled for arbitrary D if S_{half} and ξ diverge as $D \rightarrow \infty$, such fulfilment is a sufficient condition for gaplessness. For this reason, we examine the scaling of S_{half} and ξ as a function of D at chosen test points in the parameter space of a model. If the scaling suggests a CFT description of the system, we count this as evidence that the region containing that point is gapless. In these cases we also obtain an estimate for the CFT central charge c . Of course, it is possible that we misidentify a plateau in S or ξ as a sign of a gapped phase when it is merely an low- D artifact such that CFT scaling is resumed asymptotically. Such risks always remain when using inexact methods and we can only attempt to avoid them by testing to sufficiently large values of D , as well as looking for consistency with other quantities.

Another way in which we use FES is to detect significant D -dependent shifts in the location of phase transitions. We scan lines in parameter space in at least two bond dimensions with $D \geq 8$, going to larger D if we detect a significant shift in a transition. Since we are only attempting to sketch the phase diagram, we are satisfied if the shift drops below a few percent of the size of the sketched region of parameter space.

Note that we use the dynamical bond-dimension expansion scheme described in [61] in order to obtain an initial MPS with a larger D from an MPS with a smaller D . This improves the computational efficiency of calculations with large bond dimensions and also helps to ensure, in the case of broken symmetries, that we remain in the same degenerate eigenstate, rather than jumping into another. This is particularly important for broken translation symmetry and the half-chain entropy: We must take the entropy for a splitting of the chain at the same location within the translation-invariant block when performing FES.

Chapter 3

Majorana fermions and parafermions

3.1 Introduction

It is usual for quantum lattice systems (see Section 1.2), which consist of distinguishable parts (localised spins in a magnet, for example), to have modes of excitation that obey the statistics of identical quantum particles. These *quasiparticles* may be bosons or fermions, but there are also other possible emergent degrees of freedom. In this chapter we describe the emergence of *Majorana fermions* and their generalisation, parafermions, as *edge modes* in simple one-dimensional quantum lattice systems.

In experiment, the first realisations of Majorana and parafermion modes have occurred, or are likely to occur, in naturally fermionic systems, such as superconducting devices. Recently, there has been a great deal of interest [96, 97] in realising these exotic fermion-like degrees of freedom, which is largely due to their potential uses in quantum information processing [98], where they may prove useful for performing quantum computations. They could also be used to build quantum memories [99]. In the last few years, there has been some experimental evidence of the presence of Majorana edge modes in superconducting wires [100–103] and there are a number of proposals for the isolation of parafermion modes [104–107] in superconducting systems.

Since Majorana and parafermion modes are expected to occur in superconductors, one might ask why we approach the subject via spin systems. One simple reason is that spin systems are easy to treat numerically, for example using the tensor network techniques of Chapter 1. Indeed, this is what we do in Chapters 4 and 5.

We begin the chapter with a review of the “second-quantisation” description of systems of identical particles before introducing Majorana fermions and parafermions. We then show how they emerge as localised degrees of freedom in the Ising model and the clock model, respectively.

3.2 Systems of many identical particles

Here we briefly review the theory of bosons and fermions. This section is partly based on lecture notes by Eduardo Fradkin. For further reference see the (German) lecture notes by Reinhard Werner as well as [108–110].

Bosons and fermions are two kinds of quantum particle distinguished by their statistics or, equivalently, the behaviour of the quantum state of many such identical particles under their *exchange*: Bosonic wavefunctions are *symmetric* under particle exchange and fermionic wavefunctions are *antisymmetric*. We may describe a system of many identical particles using the formalism of “second quantisation”.

Since the particles are assumed to be identical, a physical many-particle state can be specified by the number of particles occupying each possible single-particle state, where the single-particle states might be positions in a lattice, or positions and spins for fermionic particles that have spin (they need not, in a nonrelativistic setting), or Fourier modes, for example. We will generally refer to single-particle states as *modes*. We use the notation

$$|\psi\rangle = |n_1 n_2 \dots n_K\rangle \quad (3.1)$$

to denote a many-particle state in which n_k particles occupy the mode $|k\rangle$ and there are K possible single-particle modes. Many-particle states of the form $|\psi\rangle$ are called *Fock states* and live in *Fock space*, which is the Hilbert space built from the direct sum of spaces of each possible particle number

$$\mathcal{F}_\pm(\mathcal{H}) \equiv \overline{\bigoplus_{N=0}^{\infty} S_\pm \mathcal{H}^{\otimes N}}, \quad (3.2)$$

where S_\pm is the symmetrising (+) or antisymmetrising (-) operator that restricts each N -particle space $\mathcal{H}^{\otimes N}$ to the space of valid bosonic or fermionic states, respectively. The (anti)symmetrising is with respect to the N factors of \mathcal{H} in $\mathcal{H}^{\otimes N}$, each of which represents one particle. The assignment of a particular factor to each particle constitutes a *labelling* of particles, making them *distinguishable* by their position in the tensor product. This would result in particle statistics of *nonidentical* particles. To avoid this, S_\pm makes the particles indistinguishable by applying all possible permutations of the tensor factors, creating a superposition

$$S_\pm(|k_1\rangle \otimes |k_2\rangle \otimes \dots \otimes |k_N\rangle) \equiv \frac{1}{\sqrt{N!}} \sum_P (\pm 1)^{\text{odd}(P)} |k_{P(1)}\rangle \otimes |k_{P(2)}\rangle \otimes \dots \otimes |k_{P(N)}\rangle, \quad (3.3)$$

where each $|k_n\rangle$ represents a single particle in mode k_n and we sum over all $N!$ permutations P of N particles. The function $\text{odd}(P)$ is 1 for odd permutations and 0 for even. Assuming $|1\rangle, \dots, |K\rangle$ form an orthonormal basis, we note that the state is only normalised if each mode only occurs once (if each particle is in a state orthogonal to the rest). This is intentional and we will take care of normalisation in the final notation.

The ordering of the $|k_n\rangle$ in the state on the left-hand side of (3.3) represents an initial, unavoidable labelling prior to symmetrisation. This initial labelling is of no consequence for

S_+ , but is a nontrivial choice for S_- , where it determines which terms in the sum receive a minus sign. This is important since it implies for example

$$S_{\pm}(|j\rangle \otimes |k\rangle) = \pm S_{\pm}(|k\rangle \otimes |j\rangle), \quad (3.4)$$

where j and k can be equal. As such, we must include the choice of initial labelling in the Fock-state notation of (3.1). To do this, we will define the Fock states to have a particular choice of initial labelling

$$|n_1 n_2 \dots n_K\rangle \equiv \frac{1}{\sqrt{n_1! n_2! \dots n_K!}} S_{\pm}(|1\rangle^{\otimes n_1} \otimes |2\rangle^{\otimes n_2} \otimes \dots \otimes |K\rangle^{\otimes n_K}), \quad (3.5)$$

where the additional coefficient ensures the states are normalised for all possible values of n_k , assuming that the modes $|1\rangle \dots |K\rangle$ form an orthonormal basis. Since states of differing overall particle number N are orthogonal by definition (3.2), the Fock states (3.5) themselves form an orthonormal basis of Fock space:

$$\langle n_1 \dots n_K | m_1 \dots m_K \rangle = \delta_{n_1 m_1} \dots \delta_{n_K m_K}. \quad (3.6)$$

The full structure of the bosonic and fermionic Fock spaces are captured by *creation* and *annihilation* operators a_j^\dagger and a_j . The creation operator adds a new particle, in mode $j = 1 \dots K$, to a many-particle state:

$$a_j^\dagger S_{\pm}(|k_1\rangle \otimes |k_2\rangle \otimes \dots \otimes |k_N\rangle) \equiv S_{\pm}(|j\rangle \otimes |k_1\rangle \otimes |k_2\rangle \otimes \dots \otimes |k_N\rangle). \quad (3.7)$$

Beginning with the *vacuum state* of zero particles $|\Omega\rangle$, we can write any (anti)symmetrised state of N particles using creation operators

$$a_{k_1}^\dagger a_{k_2}^\dagger \dots a_{k_N}^\dagger |\Omega\rangle = S_{\pm}(|k_1\rangle \otimes |k_2\rangle \otimes \dots \otimes |k_N\rangle), \quad (3.8)$$

where the ordering of the a_k^\dagger now represents the initial labelling choice. Note that the various $k_n = 1, \dots, K$ can take the same values, for example $k_1 = k_2 = 5$, in which case more than one particle in state 5 is created. We can now rewrite (3.5) using the creation operators

$$|n_1 n_2 \dots n_K\rangle \equiv \frac{1}{\sqrt{n_1! n_2! \dots n_K!}} (a_1^\dagger)^{n_1} (a_2^\dagger)^{n_2} \dots (a_K^\dagger)^{n_K} |\Omega\rangle, \quad (3.9)$$

which suggests writing the vacuum state as

$$|\Omega\rangle = |0_1 0_2 \dots 0_K\rangle. \quad (3.10)$$

From (3.9) we see that, for a state with particles occupying only one mode j ,

$$a_j^\dagger |n_j\rangle = \sqrt{n_j + 1} |n_j + 1\rangle. \quad (3.11)$$

As for the annihilation operator, from (3.9) and (3.6) we find

$$\langle n_j | a_j | m_j \rangle = \sqrt{n_j + 1} \delta_{n_j+1, m_j} = \sqrt{m_j} \delta_{n_j, m_j-1} = \sqrt{m_j} \langle n_j | m_j - 1 \rangle, \quad (3.12)$$

showing that the annihilation operator acts as

$$a_j|m_j\rangle = \sqrt{m_j}|m_j - 1\rangle, \quad (3.13)$$

where we see that a_j indeed annihilates a particle in state j . We also have the special case

$$a_j|0_j\rangle = 0, \quad (3.14)$$

which is consistent with $|0_j\rangle$ being the state containing no particles in state j .

To determine how the creation and annihilation operators act in the general case of multiple occupied modes, we must first learn how they behave under commutation. Let us investigate their algebraic properties. We can rewrite (3.4) as

$$a_j^\dagger a_k^\dagger |\Omega\rangle = \pm a_k^\dagger a_j^\dagger |\Omega\rangle, \quad (3.15)$$

which implies the commutation relations

$$[a_j^\dagger, a_k^\dagger] \equiv a_j^\dagger a_k^\dagger - a_k^\dagger a_j^\dagger = 0 \quad \text{for bosons and} \quad (3.16)$$

$$\{a_j^\dagger, a_k^\dagger\} \equiv a_j^\dagger a_k^\dagger + a_k^\dagger a_j^\dagger = 0 \quad \text{for fermions,} \quad (3.17)$$

where the relations for the annihilation operators are obtained by taking the complex conjugate. Summarised in words: Bosonic operators commute and fermionic operators *anti-commute*. As a direct consequence of (3.17), we find for fermions

$$a_j^\dagger a_j^\dagger = -a_j^\dagger a_j^\dagger \iff (a_j^\dagger)^2 = 0, \quad (3.18)$$

which implies, together with (3.9), that all fermionic states have either zero or one fermion in any given mode j : $n_j \in \{0, 1\}$. This is Pauli's exclusion principle. Taking the complex conjugate gives us $(a_j)^2 = 0$, implying again that the annihilation operator takes the vacuum state to zero: $(a_j)^2|1_j\rangle = a_j|0_j\rangle = 0$.

We now define the *number operator*

$$\hat{n}_j \equiv a_j^\dagger a_j, \quad (3.19)$$

where we use a hat to distinguish the number n_j from the operator, which acts on Fock states as

$$\hat{n}_j|n_j\rangle = \sqrt{n_j}a_j^\dagger|n-1_j\rangle = n_j|n_j\rangle, \quad (3.20)$$

as is easy to verify using (3.11) and (3.13). The number operator can be defined in terms of a_j and a_j^\dagger because we defined them in terms of unnormalised states in (3.7). We can now easily compute the behaviour of a_j and a_j^\dagger under commutation. This is easiest to do separately for bosons and fermions. For bosonic operators of the same mode we have

$$a_j a_j^\dagger |n_j\rangle = (n_j + 1)|n_j\rangle = (\hat{n}_j + 1)|n_j\rangle = (a_j^\dagger a_j + 1)|n_j\rangle \quad (3.21)$$

and for different states

$$a_j a_k^\dagger |n_j n_k\rangle = \sqrt{n_j} \sqrt{n_k + 1} |n_j n_k\rangle = a_k^\dagger a_j |n_j n_k\rangle, \quad (3.22)$$

where we use (3.16) for the first equality. Together these imply

$$[a_j, a_k^\dagger] = \delta_{jk} \mathbb{I}. \quad (3.23)$$

In the case of fermions $n_j \in \{0, 1\}$ and it is easy to just try out the action of operators on the possible states. First, we have

$$\begin{aligned} a_j a_j^\dagger |0_j\rangle &= |0_j\rangle, & a_j a_j^\dagger |1_j\rangle &= 0, & a_j^\dagger a_j |0_j\rangle &= 0, & a_j^\dagger a_j |1_j\rangle &= |1_j\rangle, \\ \implies \{a_j, a_j^\dagger\} |n_j\rangle &= |n_j\rangle, \end{aligned} \quad (3.24)$$

where we have used (3.18) and the fact that $a_j |0_j\rangle = 0$. Using this result and (3.17), we find

$$\begin{aligned} a_1 a_2^\dagger |0_1 0_2\rangle &= 0, & a_1 a_2^\dagger |0_1 1_2\rangle &= 0, & a_1 a_2^\dagger |1_1 0_2\rangle &= -|0_1 1_2\rangle, & a_1 a_2^\dagger |1_1 1_2\rangle &= 0, \\ a_2^\dagger a_1 |0_1 0_2\rangle &= 0, & a_2^\dagger a_1 |0_1 1_2\rangle &= 0, & a_2^\dagger a_1 |1_1 0_2\rangle &= +|0_1 1_2\rangle, & a_2^\dagger a_1 |1_1 1_2\rangle &= 0. \end{aligned} \quad (3.25)$$

Together these results give us

$$\{a_j, a_k^\dagger\} = \delta_{jk} \mathbb{I}. \quad (3.26)$$

We now have a complete specification of the bosonic and fermionic creation/annihilation operator algebras. For bosons, (3.16) and (3.23) are the bosonic ‘‘canonical commutation relations’’ (CCR) while for fermions, the relations (3.17) and (3.26) are known as ‘‘canonical anticommutation relations’’ (CAR).

3.2.1 Quantum lattice systems and many-particle systems

Perhaps surprisingly, it is generally possible to translate between systems of identical particles and quantum lattice systems (see Section 1.2). For bosons, this is very straightforward since we can simply map single-particle states (modes) to lattice sites, giving the lattice-site Hilbert space infinite dimensions to allow all possible boson occupation numbers

$$\mathcal{H}_{\text{MB}} = \bigotimes_{k=1}^K \mathbb{C}^{n_{\text{max}}}, \quad (3.27)$$

where we take $n_{\text{max}} \rightarrow \infty$. Since bosonic creation and annihilation operators for different modes commute, we can implement them as on-site operators in the lattice system.

In the case of fermions, due to the CAR (3.17) and (3.26), things are not as simple. There is however a standard way of implementing fermionic creation and annihilation operators that fulfil the CAR in lattice systems known as the Jordan-Wigner transformation [111]. We describe it using an example in Section 3.3.

3.2.2 Majorana fermions

We are now in a position to define Majorana fermions. They are named after Ettore Majorana, who proposed a solution to the Dirac equation in terms of neutral particles that are their own antiparticles [112]. In particle physics it has been proposed, although not yet tested conclusively, that neutrinos are Majorana fermions [113]. In this Chapter, we focus on their emergence in condensed matter systems.

Majorana fermions are fermion-like modes that can be built from normal, “Dirac” fermionic modes. Strictly speaking, they do not themselves have a consistent interpretation as *particles* [114] — for example, they lack a number operator — but can nevertheless occur as emergent degrees of freedom in certain systems, as we show in Section 3.3.

We can define Majorana operators in terms of Dirac fermion creators a_j^\dagger and annihilators a_j . For each Dirac fermionic mode, we obtain two Majorana fermionic modes

$$\gamma_{j,1} \equiv a_j^\dagger + a_j \quad (3.28)$$

$$\gamma_{j,2} \equiv i(a_j - a_j^\dagger), \quad (3.29)$$

where we note that these operators are Hermitian. We can easily check that they obey

$$\{\gamma_x, \gamma_y\} = 2\delta_{xy}\mathbb{I}, \quad (3.30)$$

where x and y refer to (j, m) with $j = 1, \dots, K$ and $m = 1, 2$. Majorana operators thus describe fermion-like modes, with similar CAR. They even obey something like an exclusion principle

$$(\gamma_x)^2 = \mathbb{I}. \quad (3.31)$$

This result, however, also excludes the naive number operator $\gamma^\dagger\gamma = \mathbb{I}$. Indeed, as noted above, there is no appropriate number operator: Majorana fermions should not be thought of as particles [114]. It is, however, the property (3.31) that leads to Majorana fermions “being their own antiparticles”: If we imagine for a moment that γ_x^\dagger actually creates a particles in mode x , the creation of a further particle in the same mode annihilates the first, leaving behind the vacuum.

3.2.3 Parafermions

Parafermions are, in a sense, generalisations of Majorana fermions. They have been proposed in the past as possible descriptions of fundamental particles [115], much like Majorana fermions, but were later rejected for these purposes [116]. They differ from Majorana fermions in that they cannot generally be constructed from Dirac fermions. To define them, we specify a parafermionic operator algebra (see for example [114])

$$\Gamma_x\Gamma_y = \omega\Gamma_y\Gamma_x \quad \text{for } x < y, \quad (3.32)$$

$$(\Gamma_x)^p = \mathbb{I}, \quad (\Gamma_x)^{p-1} = \Gamma_x^\dagger, \quad (3.33)$$

where

$$\omega \equiv e^{i\frac{2\pi}{p}} \quad p \in 2, 3, 4, \dots \quad (3.34)$$

and the Γ_x are not generally Hermitian. For $p = 2$, we recover the algebra of Majorana fermions (3.30), (3.31). For higher p , the parafermion exchange relations depend on the initial labelling, which defines the order of the modes and determines whether $x < y$. This property is best understood in terms of the emergence of these particles in spin systems, as described in Section 3.4.2.

Note that the Γ obey a modified ‘‘exclusion principle’’ (3.33), in which p such objects lead to mutual annihilation. We stress again, however, that the parafermionic operators defined here do not represent particles, as was the case for Majorana fermions. Indeed, the connection to systems of particles seems to have disappeared for $p > 2$, since we can no longer define parafermion modes in terms of Dirac fermions. Nevertheless, it is possible to define new varieties of identical quantum particle that can support parafermions, similarly to how Dirac fermions can support Majorana modes. A proposal for such a parafermionic Fock space is detailed in [114].

3.3 The Ising model as a Majorana chain

The one-dimensional quantum Ising model (with a transverse field)

$$H_{\text{Ising}} = -J \sum_{n=1}^{N-1} \sigma_n^z \sigma_{n+1}^z - h \sum_{n=1}^N \sigma_n^x, \quad (3.35)$$

where the σ are Pauli matrices operating on the site Hilbert spaces $\mathcal{H}_n = \mathbb{C}^2$, is equivalent to a one-dimensional model of free, spinless fermions. Indeed, relating it to such a system is one way of solving the model [117]. That fermions emerge as the natural degrees of freedom in this spin system can be seen by performing a series of transformations, one of which, often called a Jordan-Wigner transformation [111], translates between spin operators and fermionic creation and annihilation operators. Here, we perform a similar transformation, obtaining a system of Majorana fermions from (3.35) (see for example [118]).

To construct anticommuting operators from the Pauli operators of (3.35), which commute for different sites, we must abandon locality. We define the *string* operators

$$\gamma_{n,1} \equiv \left(\prod_{m=1}^{n-1} \sigma_m^x \right) \sigma_n^z \quad \text{and} \quad \gamma_{n,2} \equiv \left(\prod_{m=1}^{n-1} \sigma_m^x \right) \sigma_n^z \sigma_n^x = \gamma_{n,1} \sigma_n^x, \quad (3.36)$$

which, we can easily check, fulfil the CAR relations of Majorana fermions (3.30). We may thus use (3.36) to rewrite the Ising Hamiltonian (3.35) in terms of Majorana modes:

$$H_{\text{Ising}} = -J \sum_{n=1}^{N-1} \gamma_{n,2} \gamma_{n+1,1} - h \sum_{n=1}^N \gamma_{n,1} \gamma_{n,2}, \quad (3.37)$$

where we need only insert (3.36) and recall that $(\sigma_n^{x/z})^2 = \mathbb{I}$ to check the equivalence.

We may construct Dirac fermionic operators from the Majorana operators as

$$c_n^\dagger \equiv \frac{1}{2} (\gamma_{n,1} + i\gamma_{n,2}), \quad (3.38)$$

for which we can confirm the Dirac fermionic CAR (3.17) and (3.26). If we rewrite (3.37) in terms of the c_n , we would find terms like $c_n^\dagger c_{n+1}^\dagger$, which creates a ‘‘Cooper pair’’. Indeed, (3.37) describes a one-dimensional superconducting system, as studied by Kitaev in [99] in an attempt to find a system with physical Majorana modes.

3.3.1 Physical relevance of Majorana modes

The Majorana fermion picture of the Ising model (or of the superconducting model studied in [99]) is interesting, since it gives a new interpretation of the two phases discussed in Section 2.2.2. For $h \gg J$ we can neglect the J term in (3.37), and we are left with a sum over pairs of coupled Majorana modes $\gamma_{n,1}\gamma_{n,2}$, where the pairs are not coupled to each other. For $J \gg h$ we can neglect the h term and we see that, on an open, finite chain, the Majorana modes $\gamma_{1,1}$ and $\gamma_{N,2}$ do not appear in the Hamiltonian and, because the Hamiltonian is quadratic in the other γ operators, actually commute with it.

These Majorana modes, located at the edges of the chain, represent a degeneracy in the entire spectrum of $H_{\text{Ising}}(h = 0)$, and are hence known as *edge zero modes*. To see this, consider that we can build a Dirac fermionic mode from the two Majorana edge modes

$$c_{\text{edges}}^\dagger \equiv \frac{1}{2} (\gamma_{n,1} + i\gamma_{N,2}), \quad (3.39)$$

which can either be occupied or unoccupied. Since this fermion is acted upon trivially by $H_{\text{Ising}}(h = 0)$, we can modify its occupation without changing the energy. As such each energy eigenvalue has an extra twofold degeneracy due to the edge modes. This is a physical manifestation of Majorana fermions. Indeed, it is possible to show that the zero modes persist as edge-localised modes at nonzero h [99, 118]. Since this degeneracy involves a *nonlocal* fermionic mode, split across two sites that are separated by the length of the system, it may be robust against local noise (say, a disturbance that affects neighbouring lattice sites) in an experimental setup. This suggests its use as a storage medium for quantum information [99].

As noted in the introduction, there is now experimental evidence that Majorana zero modes exist at the end of superconducting wires [100–103]. There are also various other proposals for their realisation in superconducting systems [96, 97].

3.4 The clock model and parafermions

One way to generalise the Ising model (3.35) is to introduce additional spin ‘‘positions’’. The Ising model can be thought of as a simple magnet in which spins can point either up or down, and where alignment of spins is energetically favourable. We could alternatively

allow spins to point in one of p directions within a plane. If the directions are equally spaced, we can then model a spin as taking values ω^k in the group of p th roots of unity

$$\{\omega^k \mid \omega = e^{i2\pi/p}, \quad p \in \mathbb{Z}, \quad k = 0 \dots (p-1)\}. \quad (3.40)$$

Such spins are clearly cyclic, in the sense that $\omega^p = \omega^0 = 1$, and such models are often called *clock* models, drawing an analogy with the discrete positions of hours and minutes on a clock. They have also been called planar (or vector) Potts models [119]. The clock model has a global \mathbb{Z}_p symmetry under shifts of the clock position, a reflection of the dependence of the energy only on the alignment of spins and not on their absolute positions (in the absence of an external field).

Clock models can also be thought of as discretised $O(2)$ rotor models, which we study directly in Chapter 7. The rotor allows spins to point in any direction in the plane, which we can achieve in the clock model by sending $p \rightarrow \infty$.

We can implement the one-dimensional quantum p -clock model on $\mathcal{H} = \bigotimes_{n=1}^N \mathbb{C}^p$ using the operators

$$U = \sum_{k=0}^{p-1} \omega^k |k\rangle\langle k| \quad \text{and} \quad V = \sum_{k=0}^{p-2} |k+1 \bmod p\rangle\langle k|, \quad (3.41)$$

where $|k\rangle$ form an orthonormal basis for \mathbb{C}^p . We note that

$$UV = \omega VU \quad \text{and} \quad (3.42)$$

$$U^p = V^p = \mathbb{I}. \quad (3.43)$$

The operator U can be thought of as the clock “position” operator

$$U|k\rangle = \omega^k |k\rangle, \quad (3.44)$$

with V shifting the position by one

$$V|k\rangle = |k+1 \bmod p\rangle. \quad (3.45)$$

Note that, for $p = 2$ we have $U = \sigma^z$ and $V = \sigma^x$. This suggests the straightforward generalisation of the Ising Hamiltonian (3.35)

$$H_{\text{clock}} = -\frac{1}{2} \left[J \sum_{n=1}^{N-1} U_n U_{n+1}^\dagger + h \sum_{n=1}^N V_n \right] + h.c., \quad (3.46)$$

which is equal to (3.35) for $p = 2$. The Hamiltonian is invariant under global shifts

$$\mathbf{V} \equiv \prod_{n=1}^N V_n, \quad (3.47)$$

corresponding to the promised \mathbb{Z}_p symmetry.

3.4.1 Phases of the clock model

The phase diagram of the clock model (3.46) is known to vary quite significantly with p [36, 37]. Note that many known results are for the classical two-dimensional model, which we may carry over to the quantum one-dimensional case via the quantum-to-classical mapping (see Section 2.2.2), in which the classical temperature maps onto the field strength. For all finite p , there is a low field $h \ll J$ ferromagnetic phase in which spins are aligned with their neighbours and the \mathbb{Z}_p symmetry is broken by each of the p ground states (see Section 2.2.2). At sufficiently high field strength $h \gg J$ the system is in a paramagnetic phase in which spins are disordered and the \mathbb{Z}_p symmetry is restored. Between these phases is either a second-order phase transition at $h/J = 1$ for $p \leq 4$ or a critical (gapless) phase bordered by two continuous transitions, thought to be of the BKT type (see 2.2.2). The critical phase grows in extent with p , eventually taking up the entire low-field part of the phase diagram as $p \rightarrow \infty$ and we recover the rotor model [36, 37].

Only the Ising case of $p = 2$, as well as the $p = 4$ case, which can be shown to be equivalent to two decoupled Ising models [36, 37], are exactly solvable. In these cases it is known that the critical point at $|h|/J = 1$ is described by a CFT with central charge $c = 1/2$ [78]. The case $p = 3$ is known as the three-state Potts model. It can be solved at its critical point $h/J = 1$, where it is described by a CFT with central charge $c = 4/5$ [78]. At higher p , the gapless phase is described by a CFT with $c = 1$, matching the known value for the XY model [78].

For higher p , the occurrence of BKT transitions at intermediate field strength makes a certain amount of intuitive sense: At intermediate field strength fluctuations are strongest as paramagnetic and ferromagnetic orders compete. One might imagine that they at some point become strong enough to “smear out” the discrete clock positions into an effective continuum. This would constitute an *emergent* $O(2)$ symmetry, making the model behave like the $O(2)$ rotor model in this regime, which is known to have a BKT transition.

3.4.2 Parafermions in the clock model

It is known that the clock model can be viewed as a system of parafermions [38]. To show this, we carry out a generalised Jordan-Wigner transformation in a procedure exactly analogous to that performed on the Ising model in Section 3.3. We first define string operators

$$\Gamma_{n,1} \equiv \left(\prod_{m=1}^{n-1} V_m \right) U_n \quad \text{and} \quad \Gamma_{n,2} \equiv \left(\prod_{m=1}^{n-1} V_m \right) U_n V_n = \Gamma_{n,1} V_n, \quad (3.48)$$

finding that they obey the parafermionic exchange relations (3.32) and (3.33) from Section 3.2.3. Rewriting (3.46), we get

$$H_{\text{clock}} = -\frac{1}{2} \left[J \sum_{n=1}^{N-1} \bar{\omega} \Gamma_{n+1,1}^\dagger \Gamma_{n,2} + h \sum_{n=1}^N \Gamma_{n,2}^\dagger \Gamma_{n,1} \right] + h.c., \quad (3.49)$$

where we see that, as for the Ising model in Section 3.3.1, the operators $\Gamma_{1,1}$ and $\Gamma_{N,2}$ do not appear in the Hamiltonian for $h = 0$ and in fact commute with the remaining terms.

This means, as in the fermionic case, that the spectrum of $H_{\text{clock}}(h = 0)$ has zero modes, which are this time parafermionic.

The question of whether these modes persist for the entire low field phase of the clock model is harder to answer than in the Ising/Majorana case, since the clock model has not been solved. Fendley has shown in [118] that the *chiral* clock model at $p = 3$, which introduces an additional phase on the parameters of (3.49), can have robust parafermionic edge modes. Also, Bondesan and Quella, as well as Motruk et al., have recently presented classifications of gapped phases of \mathbb{Z}_p -symmetric quantum spin chains, including phases with parafermionic edge zero modes [120, 121].

Chapter 4

Interacting Majorana chains: The Kitaev edge

4.1 Introduction

In Chapter 3 the transverse field Ising model was shown to be equivalent to a model of free Majorana fermions. Physically relevant Majorana modes, like the edge modes discussed in 3.3, should emerge in superconductors with triplet pairing symmetry or semiconductor structures brought into tunnelling contact with ordinary “s-wave” superconductors [96, 97]. In the latter case, experimental evidence of the existence of Majorana edge modes in one-dimensional “wire” structures is amassing [100, 101, 122–124]. One intriguing application of these “nanowires” [99] is to build a two-dimensional array out of them, as illustrated in Figure 4.1. In such an array, the Majorana modes localised at the edges of the nanowires

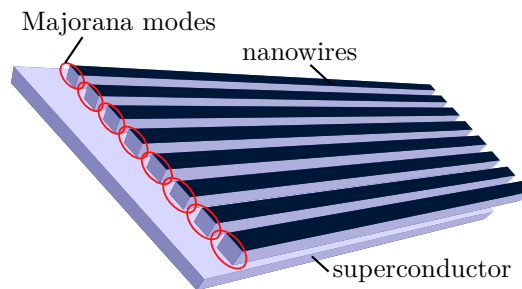


Figure 4.1: Majorana edge modes localised at the ends of semiconducting nanowires in proximity interaction with a superconductor. The result is a two-dimensional weak topological insulator (TI), the edge of which is described by a chain of interacting Majorana fermions.

can interact leading to an effective one-dimensional edge theory of the two-dimensional array, without a spectral gap [125–129]. This is an example of a topological insulator (TI) [130, 131], which is a system in which the boundary is gapless despite the bulk being gapped (see Chapter 2). The best known example of a TI is the quantum Hall insulator [132], which can support fractional charges on its boundary in the presence of interactions

[133]. In the absence of interactions, possible types of TI have been classified according to the symmetries they obey [134, 135]. However, investigating the properties of interacting systems is significantly more difficult [136–141].

An array of nanowires is an clearly anisotropic, with the Majorana edge modes existing only on the edges perpendicular to the nanowires. Such a system is an example of a “weak” TI [28–35], in which the gapless edges exist only in the presence of translation symmetry of the bulk. Given translation invariance in the bulk, the one-dimensional edge theory of the nanowire array is a translation-invariant theory of Majorana modes, which maps to the one-dimensional Ising model at its critical point (see Sections 3.3 and 2.2.3). In this chapter, most of which was published in [142], we use the matrix product state techniques of Chapter 1 to investigate the effects of an additional, translation-invariant interaction term on this edge theory. We find that the chain remains gapless in the presence of strong attractive interactions, staying in the same phase as the non-interacting chain, which is described by an Ising-type CFT with central charge $c = 1/2$. However, repulsive interactions can “gap out” the system or place the system in a second gapless phase with incommensurate order, described by a CFT with central charge $c = 3/2$.

The numerical results of this chapter were obtained by the author as part of a collaboration with Emilio Cobanera, Luis Searba, Ion Cosma Fulga and Carlo W. J. Beenakker. We note that the same model was simultaneously studied by Rahmani et al. [143, 144], whose results were obtained using different techniques and serve to confirm our own. The published numerical study of the present author [142] additionally includes numerics by Luis Searba for the *disordered* case in which the parameters of the Hamiltonian are allowed to vary randomly. This constitutes an important check of the effects of statistical translation-invariance on the interacting weak TI.

4.2 Interacting Kitaev edge model

4.2.1 Majorana fermion Hamiltonian

The translation-invariant chain of Majorana fermions is called the “Kitaev edge” because it is a natural candidate description (see, for example [129]) of the edge of an array of Kitaev wires [99] (Majorana chains). We study the *interacting* Kitaev edge numerically by mapping it to a spin chain, in the same way as the Kitaev wire is mapped to the Ising model in Section 3.3. Its Hamiltonian, in terms of Majorana fermions, is

$$H = -i \sum_s \alpha \gamma_s \gamma_{s+1} - \sum_s \kappa \gamma_s \gamma_{s+1} \gamma_{s+2} \gamma_{s+3}, \quad (4.1)$$

where $\{\gamma_s, \gamma_t\} = 2\delta_{st}$ and $\gamma_s = \gamma_s^\dagger$ and s labels the Kitaev wires that make up the 2D array. With $\kappa = 0$ we recover the Kitaev wire, or Majorana chain (3.37) of Section 3.3 at its critical point, placing the system in a gapless phase corresponding to the critical point of the Ising model (see Section 2.2.3).

We choose the interaction term, governed by κ , to be the simplest translation-invariant interaction term of Majorana modes. If we switch to Dirac fermionic modes

$$\gamma_{2s-1} = c_{2s} + c_{2s}^\dagger, \quad i\gamma_{2s} = c_{2s} - c_{2s}^\dagger, \quad (4.2)$$

for which we must distinguish between odd and even Majorana modes, we find that the interaction term has the form

$$-\gamma_s \gamma_{s+1} \gamma_{s+2} \gamma_{s+3} = (2n_{s+1} - 1)(2n_{s+3} - 1), \quad (4.3)$$

for odd s , where $n_s \equiv c_s^\dagger c_s$ is the number operator, and

$$-\gamma_s \gamma_{s+1} \gamma_{s+2} \gamma_{s+3} = (c_s - c_s^\dagger)(2n_{s+2} - 1)(c_{s+4} + c_{s+4}^\dagger) \quad (4.4)$$

for even s . Since we can properly interpret the Dirac fermionic modes as particles (see Section 3.2.2), the Dirac fermion picture allows us to better interpret the physical processes involved in the Majorana fermion interaction. We see that (4.3) has the form of a density-density interaction, such that $\kappa > 0$ results in a *repulsive* interaction between Dirac fermions and $\kappa < 0$ results in an *attractive* interaction. The even term (4.4) is required for translation-invariance in the Majorana picture. Although these Dirac fermions do not directly represent the microscopic degrees of freedom in a realistic, 2D device, they do represent the emergent effective modes that are relevant for the interaction in the edge theory. Note that, since we have translation invariance, we could just as well have chosen the Dirac fermionic modes such that (4.3) is the even term and (4.4) is the odd term.

4.2.2 Spin Hamiltonian

We now obtain a spin Hamiltonian using a Jordan-Wigner transformation similar to that used in Section 3.3:

$$\gamma_{2s} = \left(\prod_{j=1}^{s-1} \sigma_j^x \right) \sigma_s^y, \quad \gamma_{2s-1} = \left(\prod_{j=1}^{s-1} \sigma_j^x \right) \sigma_s^z, \quad (4.5)$$

where we again make a distinction between odd and even Majoranas, which is nonphysical when the system is translation-invariant. The model (4.1) becomes

$$\begin{aligned} H = & - \sum_j \alpha_o \sigma_j^x - \sum_j \alpha_e \sigma_j^z \sigma_{j+1}^z \\ & + \sum_j \kappa_o \sigma_j^x \sigma_{j+1}^x + \sum_j \kappa_e \sigma_j^z \sigma_{j+2}^z, \end{aligned} \quad (4.6)$$

where the α_o and κ_o terms originate from the odd terms in (4.1), and the α_e and κ_e terms come from the even terms in (4.1). We differentiate between the even and odd parameters in the spin model because it is sometimes useful to understand the translation-invariant case of $\alpha_o = \alpha_e$ and $\kappa_o = \kappa_e$ model as a special case within a larger space of theories. The α terms are exactly the Ising Hamiltonian, as expected from the Kitaev wire case (3.37). Ignoring the κ_o term, the full Hamiltonian is the ANNNI model (5.5) discussed in Chapter 5. The phase diagram of the ANNNI model has been studied in this context before [145, 146], however the κ_o term, needed for translation invariance of the physical, Majorana system, is new and significantly alters the phase diagram.

4.2.3 Self-duality and symmetries of the model

A translation of one site in terms of Majoranas $\gamma_s \rightarrow \gamma_{s+1}$ is, due to (4.5), nontrivial in terms of spins. Indeed it must transform the odd and even terms of (4.6) into each other. This translation is a *duality* transformation [147] that sends $\alpha_e \rightarrow \alpha_o$ and $\kappa_e \rightarrow \kappa_o$, with the physical case of full translation invariance $\kappa_e = \kappa_o \equiv \kappa$ and $\alpha_e = \alpha_o \equiv \alpha$ representing the *self-dual* point, that is the point invariant under the duality transformation. The transformation is

$$\begin{aligned} \sigma_j^z &\mapsto \prod_{k=1}^j \sigma_k^x \quad j = 1, \dots, N, \\ \sigma_j^x &\mapsto \sigma_j^z \sigma_{j+1}^z, \quad j = 1, \dots, N-1, \quad \text{and} \quad \sigma_N^x \mapsto \sigma_N^z, \end{aligned} \quad (4.7)$$

where we may neglect the boundary terms as they do not affect bulk physics in the thermodynamic limit. In the Ising case of $\kappa = 0$, this duality is well known. Indeed, it determines the location of the phase transition (see Section 2.2.3) of the Ising model [148]. This is because transitions survive the duality transformation, which is unitary, and thus preserves the spectrum of H . As such, a transition at $H(\alpha_o, \alpha_e)$ has a companion at $H(\alpha_e, \alpha_o)$ so that, if the number of transitions is known to be odd, one of them must occur at the self-dual point $H(\alpha, \alpha)$. In the ANNNI case $\kappa_e = 0$, $\kappa_o \neq 0$, the duality transformation (4.7) is the same one discussed in Section 5.2.2, so that $\kappa_o = 0$, $\kappa_e \neq 0$ represents the dual ANNNI model.

There is a further unitary transformation

$$\sigma_j^x \mapsto -\sigma_j^x, \quad \sigma_j^y \mapsto (-1)^j \sigma_j^y, \quad \sigma_j^z \mapsto (-1)^{j+1} \sigma_j^z, \quad (4.8)$$

which flips the sign on α , as can be seen by applying the transformation to (4.6) or (4.5). The κ interaction term is left invariant. This implies that we may restrict to $\alpha \geq 0$, when determining the phase diagram of the model since, again, phase transitions are preserved by unitary transformations. To see that the transformation is unitary it suffices to consider the signs, which leave the Pauli commutation relations $[\sigma^a, \sigma^b] = 2i \sum_c \epsilon^{abc} \sigma^c$ unchanged.

Another interesting symmetry of the model exists only at $\alpha = 0$. Here, the unitary transformation

$$U_c = \left(\prod_k \sigma_{2k}^z \right) \left(\prod_k \sigma_{4k}^x \sigma_{4k+1}^x \right) \quad (4.9)$$

acts on the Hamiltonian as $U_c H(\alpha = 0) U_c^\dagger = -H(\alpha = 0)$. A unitary that anticommutes with H is sometimes called a *chiral* symmetry [149]. It implies that the spectrum of $H(\alpha = 0)$, which is bounded from below, is symmetric about zero, which in turn implies that any transition occurring at $\alpha = 0$, for positive κ also occurs at $\alpha = 0$ for negative κ .

4.3 Numerical study

We wish to determine the phase diagram of Kitaev edge model (4.1) by simulating the equivalent spin model (4.6), using matrix product states (MPS) (see Chapter 1) and the phase-diagram-sketching techniques of Section 2.3. In particular we are interested in whether the

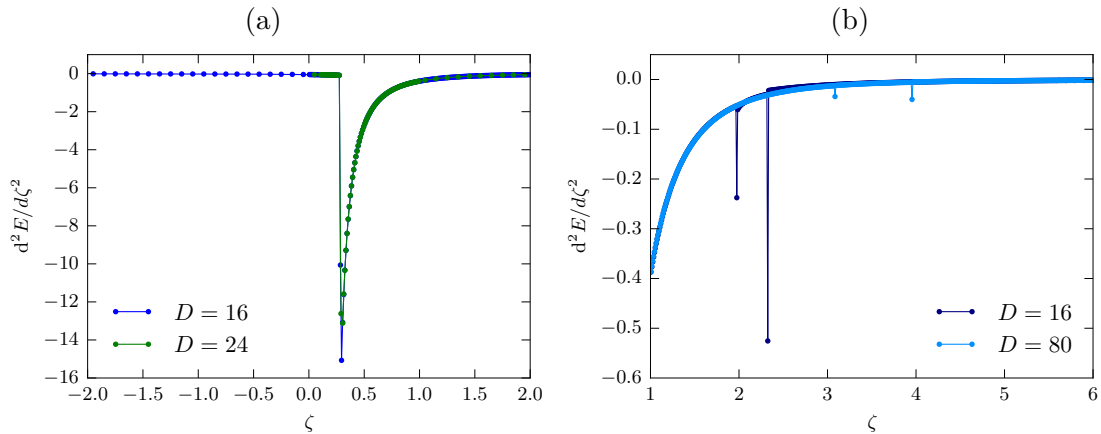


Figure 4.2: The second derivative of the ground state energy E , with respect to ζ . **(a)**: An apparent second-order transition at $\zeta \approx 0.3$ marking the upper boundary (in ζ) of the Ising phase. The location of the transition does not appear to be dependent on the bond dimension D . **(b)**: Smaller jumps in the region $1 < \zeta < 6$. Although Figure 4.6 provides evidence of a transition ending the floating phase here, there is no evidence of a second order transition in the energy data. The jumps may indicate the presence of a higher order singularity, or may be a finite-entanglement artifact. The second jump occurs at the wavevector locking location of Figure 4.6 (a).

interactions ($\kappa \neq 0$) can open up a spectral gap (“gap-out”) the system, or lead us into a gapless phase that is distinct from the Ising phase of the noninteracting chain.

For most of the numerical study, we restrict to the physically relevant case of the translation-invariant (self-dual) model. Since we need only treat the $\alpha > 0$ case (see Section 4.2.3), we can explore the system in terms of the dimensionless parameter

$$\zeta \equiv \kappa/\alpha, \quad (4.10)$$

where the sign on ζ matches the sign on κ .

Before beginning, we can already make some predictions about the phase diagram. For $\zeta = 0$, (4.6) we know we have an Ising critical point, which may be part of a larger Ising phase unless turning on the interactions immediately destroys it. We may also expect a floating incommensurate phase (see Section 2.2.5) to be present for $\zeta > 0$, due to the the close relationship with the ANNNI model (5.5), which is a prototypical example of a system with such a phase.

Throughout the present study, we use MPS ground states converged up to $\eta \leq 10^{-8}$, where η is the norm of the effective energy gradient vector (1.83).

4.3.1 Critical Ising phase

Using initial line scans in ζ , starting at $\zeta = 0$ and with bond-dimensions $D = 16$ and $D = 24$, we find clear indications of a phase transition at $\zeta \approx 0.3$, as is apparent from the second derivative of the ground state energy shown in Figure 4.2 (a). Since the second derivative appears to diverge, we classify this transition as second order (see Section 2.3).

We find no evidence of further transitions for $-10 \leq \zeta < 0.3$, which includes the critical Ising point $\zeta = 0$. We may thus conclude that this entire region constitutes a gapless, critical Ising phase. We check for CFT scaling (2.15) of ξ with S , finding scaling consistent with the Ising value of the central charge $c = 1/2$ at several values of ζ in the region, as shown in Figure 4.3 (a).

4.3.2 Floating phase

For $\zeta > 0.3$ we find a second gapless region with a central charge $c = 3/2$, a somewhat unusual value (see Figure 4.3 (b)). We also find nontrivial complex phases on the larger eigenvalues of the MPS transfer matrix, representing modulation wavevectors of connected correlation functions (see Section 1.3.6). By also examining correlation functions of likely order parameters, we find that the correlation functions C_{σ^z, σ^z} and C_{σ^x, σ^x} (defined in (1.4)), shown in Figure 4.5 (a) are both modulated in this region, with the wavevector for σ^x being roughly twice that of σ^z . These wavevectors appear to vary continuously as a function of ζ , starting from zero at $\zeta = 0.3$ and ending at a nonzero commensurate value for a larger value of ζ . The $c = 3/2$ phase is thus a floating, incommensurate phase (see Section 2.2.5). We plot the larger of the two relevant wavevectors, corresponding to the modulation of σ^x , in Figure 4.6 (a).

We find the *locking location* $\zeta_l > 0.3$, at which the wavevector becomes fixed at a commensurate value, to be highly dependent on the MPS bond dimension D . To determine whether the wavevector locks at finite ζ_l in the exact ground state, we use finite-entanglement scaling (FES) in attempt to extrapolate the exact result (see Section 2.3.2). In Figure 4.6 (b), using data from MPS with D up to 256, we extrapolate ζ_l to infinite bond-dimension, finding $\zeta_l \approx 5$. The locking of the wavevectors likely constitutes a phase transition out of the $c = 3/2$ phase. Indeed, Section 4.3.3 provides evidence that the spectrum is gapped beyond this point. Note that it is possible that the extrapolation is misleading and that more points would change this picture, so that the exact value of ζ_l is larger.

Interestingly, the second derivative of the energy, shown in Figure 4.2 (b), is smooth except for some small jumps, which may be artifacts of finite entanglement. This suggests that this transition is not second order in our sense (see Section 2.2.3). Since the first derivative also appears to be continuous, and we do not observe power-law scaling of the wavevector or the order parameters σ^x or σ^z , we hypothesise that this transition is of higher order, and is possibly of BKT type.

4.3.3 Gapped anti phase

For $\zeta > 5$, we observe a breakdown in CFT scaling of S with ξ , indicating the appearance of a spectral gap, this is shown for $\zeta = 10$ on the left of Figure 4.4 (a). MPS ground states in this phase have a block size of $L = 4$, and we find ground state expectation values for σ^x and σ^z that oscillate with wavevectors π and $\pi/2$, respectively. Corresponding oscillations in the correlation functions are shown in Figure 4.5 (b). We call this phase an “anti phase” as σ^z has the same up-up-down-down pattern of expectation values as in the anti phase of

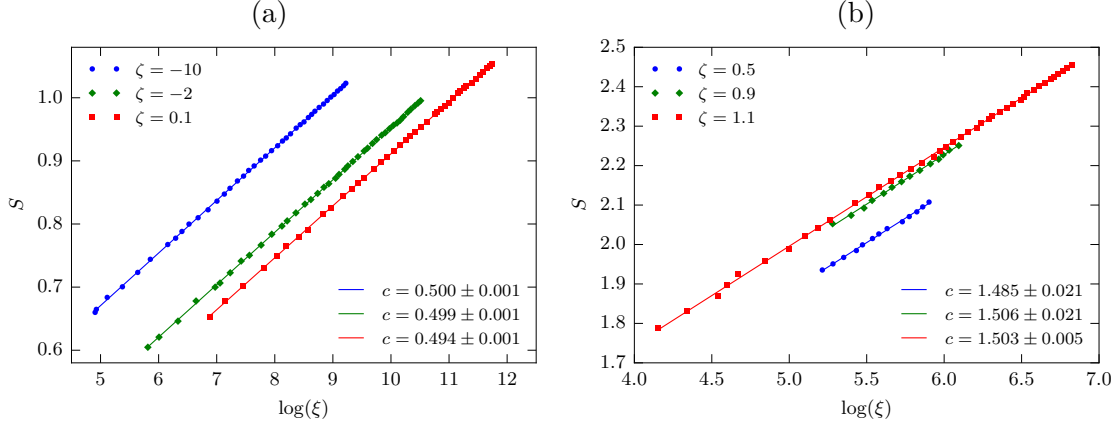


Figure 4.3: Finite entanglement scaling plots showing the entanglement entropy $S(D)$ against the correlation length $\xi(D)$ in the regions $-10 \leq \zeta \leq 0.3$ using $16 \leq D \leq 96$ **(a)** and $0.3 < \zeta < 5$ using $18 \leq D \leq 102$ **(b)**. We observe the linear behaviour (2.15) predicted for a CFT, consistent with central charges of $c = 1/2$ for $\zeta < 0.3$ and $c = 3/2$ for $0.3 < \zeta < 5$. These two regions likely belong to different phases. In the $c = 3/2$ region, at larger values of ζ than those plotted, lower bond dimensions lead to a nonphysical pseudo-transition, such that testing the scaling for these values becomes more difficult.

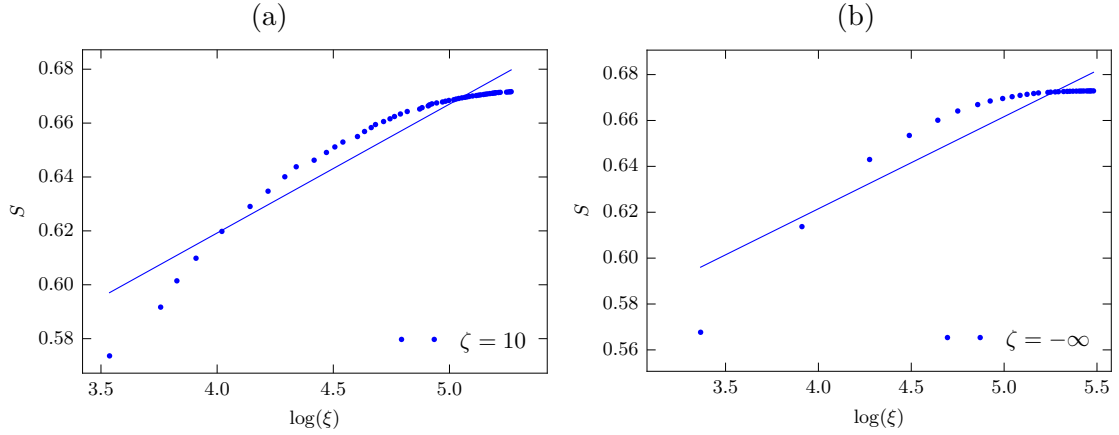


Figure 4.4: Finite entanglement scaling plots of the entanglement entropy $S(D)$ against the correlation length $\xi(D)$ showing evidence of a spectral gap at **(a)** $\zeta = 10$ ($18 \leq D \leq 128$) and **(b)** $\zeta = -\infty$ ($16 \leq D \leq 256$). These plots suggest a spectral gap because they show a breakdown of linear CFT scaling (2.15), with $S(D)$ and $\xi(D)$ saturating at higher D . The straight lines are least-squares fits to the plotted data points.

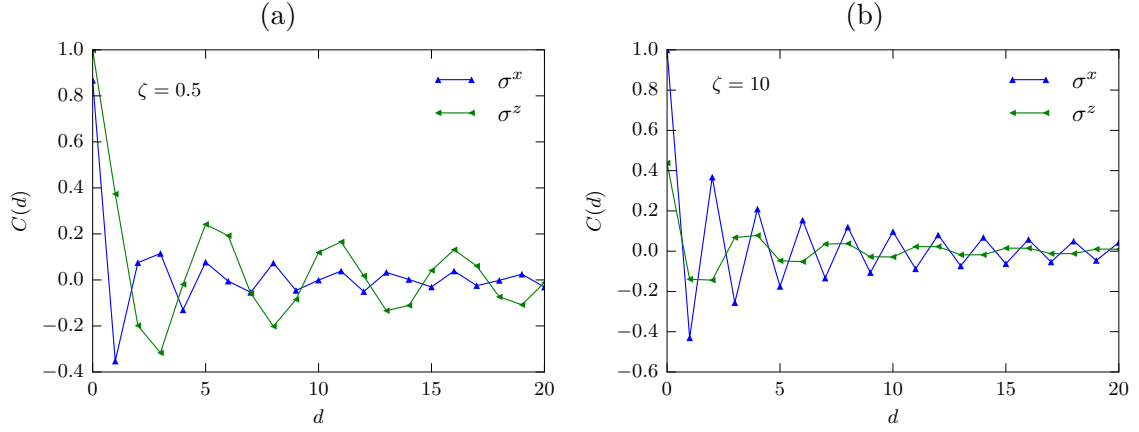


Figure 4.5: Connected correlation functions for σ^x and σ^z in the floating incommensurate phase (a) and in the anti phase (b), clearly showing modulation, with σ^x oscillating twice as fast as σ^z . The wavevector clearly takes a commensurate value in the anti phase, whereas the oscillation is not obviously commensurate in the floating phase.

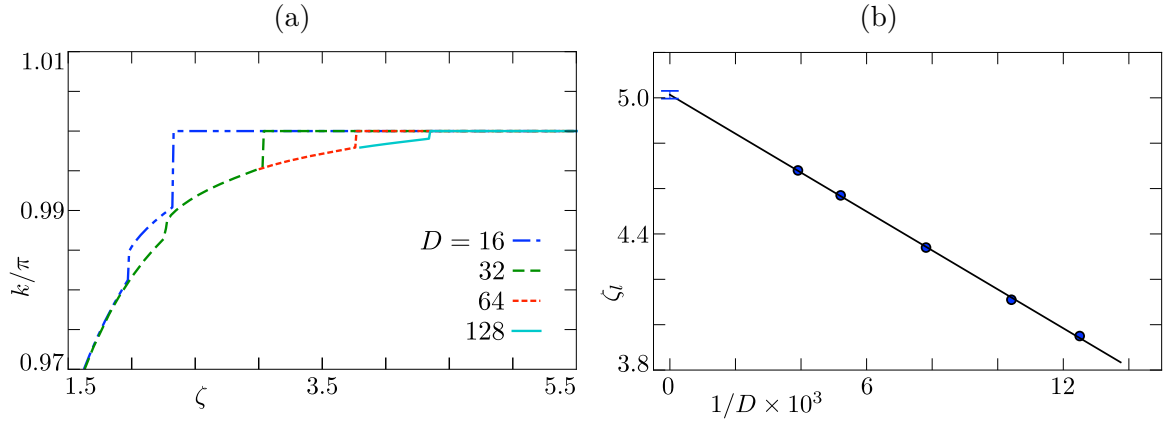


Figure 4.6: (a): The wavevector associated with the σ^z - σ^z correlation function, showing locking at $k = \pi$, which marks the end of the floating phase. We plot the wavevector for several values of the bond dimension D , showing its strong influence on the locking location ζ_l . (b): Extrapolation of ζ_l to infinite D using a maximum D of 256. The results appear to show convergence towards a finite value of $\zeta_l \approx 5$.

the ANNNI [43]. This gapped phase extends at least to $\zeta = 10$, probably to $\zeta = +\infty$, as argued in Section 4.3.5.

4.3.4 Phase diagram

For smaller values of $|\zeta|$, we now have sufficient data to sketch the phase diagram in Figure 4.7. We have seen that the system remains critical for very strong attractive interactions $\zeta < 0$, whilst repulsive interactions $\zeta > 0$ fairly quickly drive a transition into a phase with $c = 3/2$ and incommensurate structure, which soon ends in a gapped phase.

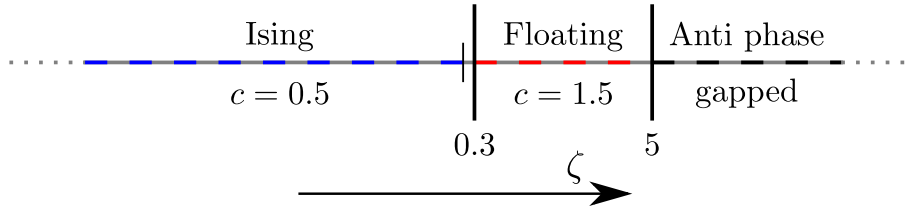


Figure 4.7: Numerically obtained phase diagram of the Kitaev edge model at lower interaction strengths ζ . The transition at $\zeta \approx 0.3$ appears to be second order in light of the behaviour of the energy in its vicinity shown in Figure 4.2. The transition at $\zeta \approx 5$ seems to be a higher order transition, possibly of BKT type. The gapped phase likely continues uninterrupted as $\zeta \rightarrow +\infty$, while there is evidence [144] that the Ising phase ends at $\zeta \approx -250$.

4.3.5 Strong interactions

By studying the bare interaction term $\alpha = 0$, we can determine the phase at $\zeta = \pm\infty$. Due to the chiral symmetry (4.9) at $\alpha = 0$, we know that $H(\zeta = +\infty)$ shares the same spectral properties as $H(\zeta = -\infty)$: In particular, they have the same mass gap. The $\zeta = +\infty$ case has modulations similar to those of the $\zeta > 5$ anti phase, with the same four-site periodicity in expectation values, while the $\zeta = -\infty$ case has full translation invariance, making it computationally easier to reach higher bond dimensions with the latter choice. We find that both cases exhibit the same kind of breakdown in CFT scaling (see Section 2.3.2) as seen in the anti phase, indicating a gap. We also numerically estimated the mass gap directly for the more efficient $\zeta = -\infty$ case, using the MPS excitations ansatz described in Section 1.4.5. An extrapolation to infinite D (see Figure 4.8) leads to a nonzero, albeit small value, providing more evidence for a spectral gap.

As further confirmation, we also examine the energy landscape for indications of a second order transition that would indicate criticality. To do this, we leave the self-dual point, fixing $\kappa_e = -1$ and varying κ_o about -1 (with $\alpha = 0$). We indeed find evidence of a transition, as shown in Figure 4.9, but the discontinuity of the first energy derivative indicates it to be of the first-order variety, consistent with a spectral gap at the self-dual point. Interestingly, the second derivative suggests a nearby second order transition, which could explain why relatively large bond dimensions must be reached before the breakdown in CFT scaling becomes apparent.

We conclude due to the gap and similar ground state structure, that the anti phase likely extends from $\zeta \approx 5$ to $\zeta = +\infty$. That the $\zeta = -\infty$ case is also gapped implies the presence of a phase transition ending the critical Ising phase at some finite negative value of ζ . Indeed, the authors of [144], who worked on the same model simultaneously with our work, locate a transition at very large interaction strength $\zeta \approx -250$.

4.4 Discussion and conclusions

According to our numerical results, the interacting Kitaev edge remains in the gapless “Ising critical” phase of the noninteracting system, with central charge $c = 1/2$, for very strong attractive interactions $\zeta < 0$. Eventually, our evidence shows, it must enter a gapped phase, since the $\zeta = -\infty$ point appears to be gapped. Repulsive interactions $\zeta > 0$, in contrast, already introduce a gap at $\zeta \approx 5$, meaning that the 2D nanowire array leaves the weak-TI phase.

Interestingly, we find a distinct gapless phase with central charge $c = 3/2$ intervening between the Ising phase and the gapped phase. The $c = 3/2$ phase appears to be an incommensurate floating phase, where the modulated order parameters are σ^x and σ^z in the spin system. Since σ^x corresponds to the odd $\gamma_{2s-1} \gamma_{2s}$ interaction in the Majorana picture, which in terms of our choice (4.2) of Dirac fermions is $\gamma_{2s-1} \gamma_{2s} = 2n_s - \mathbb{I}$, these modulated structures can be interpreted as (incommensurate) charge-density waves.

We find that the transition between the floating phase and the gapped antiphase at $\zeta \approx 5$ undergoes a strong shift in position in the finite- D MPS approximation due to finite entanglement effects: The value $\zeta \approx 5$ come from a finite-entanglement scaling (FES) extrapolation. Although we are confident that the FES results are accurate, it is of course possible that they are mistaken, perhaps due to imperfect convergence of the MPS ground state. Also, going to still-higher bond dimensions might uncover further shifts towards higher ζ . One intriguing alternative hypothesis is that locking of the incommensurate wavevector never occurs at finite ζ , such that the wavevector comes ever-closer to a commensurate value, never reaching it. Such values of the wavevector, when rational, represent extremely high correlation-function periodicities, which in turn require very large correlation lengths, making them difficult to represent in MPS form. For experimental purposes, however, the distinction is likely to be moot since, as shown in [142], disorder tends to destroy the floating phase, such that its extent will at least be diminished in a real experimental setup. Furthermore, the finite length of the edge of an experimental device puts an upper limit on the possible periodicity of correlation functions.

If the floating phase does survive to some extent in experiments, it should be distinguishable from the Ising phase via *thermal conductivity* measurements. This is because the central charge of the CFT describing the gapless phase determines the thermal conductivity of the edge [150–153]. The central charge $3/2$ of the floating phase is, furthermore, itself quite interesting. It may result from a sum of the central charges of two decoupled theories: A fermionic theory with $c = 1/2$ and a bosonic theory with $c = 1$ (see [78]). This interpretation would fit the conclusions of [144], in which they find that the gapped antiphase should be *supersymmetric*, possessing a bosonic counterpart to fermionic excitations.

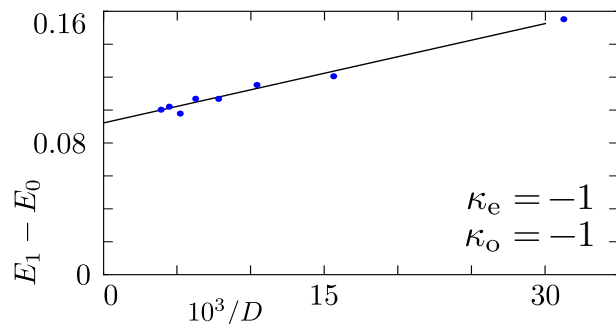


Figure 4.8: Scaling of the spectral gap $E_1 - E_0$ with the bond dimension D at the self-dual point $\kappa_e = \kappa_o$ of the the pure interaction term ($\alpha = 0 \implies \zeta = -\infty$), indicating a finite gap at infinite D .

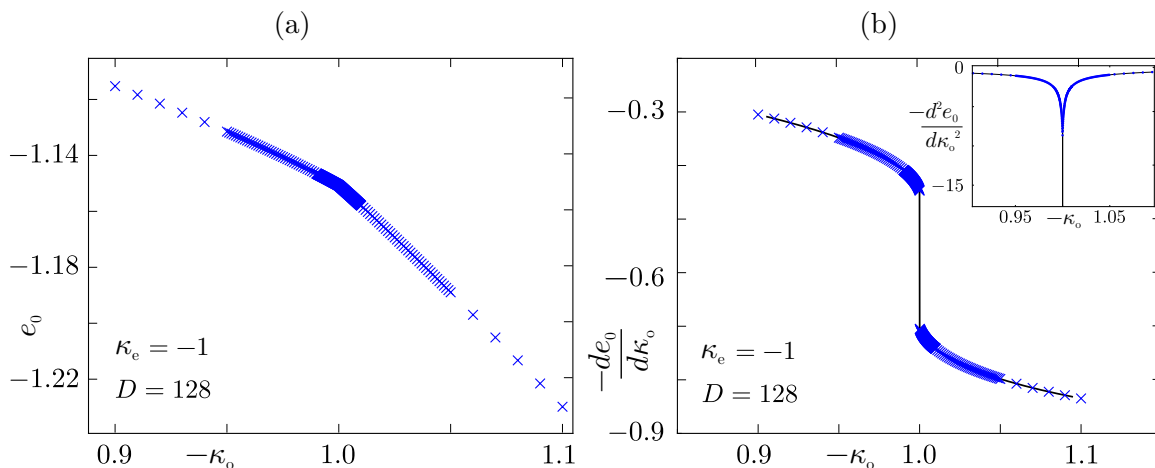


Figure 4.9: Evidence of a first-order transition at the self-dual point $\kappa_e = \kappa_o = -1$ of the pure interaction term ($\alpha = 0 \implies \zeta = -\infty$). **(a)**: Ground-state energy density e_0 for $D = 128$, with the form consistent with a first-order transition. **(b)**: First and second (inset) derivatives of the ground-state energy density. The first derivative shows a clear jump, indicating a first-order transition, although the second-derivative shows a strong cusp minimum, which we would otherwise interpret as indicating a second-order transition. We conclude that the transition is first order, with a nearby second-order transition.

Chapter 5

Axial next nearest neighbour clock model

5.1 Introduction

In this chapter we numerically determine phase diagrams for the axial next-nearest-neighbour clock (ANNNC) model, a generalisation of the clock model of Chapter 3 including a next-nearest-neighbour interaction with a ground state that conflicts with that of the nearest-neighbour term of the clock model, introducing *frustration* [154] to the system. The case with $p = 2$ clock positions is known as the axial next-nearest-neighbour Ising (ANNNI) model [43] which, in addition to the Ising model phases, possesses a Beresinskii-Kosterlitz-Thouless (BKT) transition [87] and a floating incommensurate phase [43, 89] in which correlations are spatially modulated with a modulation wavevector that varies continuously in parameter space (see Section 2.2.2). Most previous investigations of the ANNNI model have treated the classical, two-dimensional case, although it has been recently studied in the one-dimensional quantum setting [90] using DMRG techniques. As such, we skip this case of the ANNNC model here, focusing on the $p > 2$ quantum model.

A question one might ask of the $p > 2$ ANNNC model is how the additional clock positions alter the phase structure seen in the $p = 2$ ANNNI case. This is of academic interest in itself, but also connects to experiment, since it appears possible to implement a model dual to the ANNNC model, which we refer to as the ANNNC-D model, in the low-energy physics of a mesoscopic device involving a fractional topological insulator. The proposed device involves parafermion modes (see Chapter 3) and can simulate the ANNNC model for even numbers of clock positions $p = 2m$ for integer m . It was devised by Michele Burrello and Emilio Cobanera, who collaborated with the present author on [155].

An interesting feature of the ANNNC-D model is that the order parameter for the incommensurate-commensurate transitions, assuming these occur similarly to those of the ANNNI case, is a nonlocal *string* operator. As such, its phases are not characterised by the Landau theory of phase transitions, which only treats local order parameters (see Section 2.2.2).

The numerical study described in this chapter was conducted by the present author as

part of a collaboration with Emilio Cobanera, Michele Burrello, and Gerardo Ortiz. The results for $p = 6$ were published in [155], while the results for $p = 3$ and $p = 5$ are planned for later publication.

5.2 The axial next-nearest-neighbour clock model

The ANNNC model is a generalisation of the clock model (3.46). Its Hamiltonian is

$$H_{\text{ANNNC}} = -\frac{1}{2} \left[h \sum_{i=1}^N V_i + J \sum_{i=1}^{N-1} U_i U_{i+1}^\dagger - \Delta \sum_{i=1}^{N-2} U_i U_{i+2}^\dagger \right] + h.c., \quad (5.1)$$

where U and V are the operators (3.41) used in defining the clock model, satisfying $UV = \omega VU$ and $U^p = V^p = \mathbb{I}$ for $\omega = e^{i2\pi/p}$. Operators on different sites commute

$$[U_j, V_{k \neq j}] = 0. \quad (5.2)$$

This model differs from the clock model (3.46) in the additional next-nearest-neighbour interaction term, parametrised by Δ . The word ‘‘axial’’ in the name refers to the fact that the nearest and next-nearest-neighbour terms commute, and can be thought of as classical spins restricted to a common plane, sharing an ‘‘axis’’.

Just like the clock model, the ANNNC Hamiltonian (5.1) commutes with the unitary operator

$$\mathbf{V} \equiv \prod_{i=1}^N V_i, \quad (5.3)$$

which performs a global shift by one spin position. This represents a \mathbb{Z}_p symmetry of the system which may be spontaneously broken. The local order parameter for this symmetry is

$$\Omega_{\mathbf{V}}(J, \Delta, h) \equiv \langle U_i \rangle_{\Psi(J, \Delta, h)} \quad \forall i \in 1 \dots N, \quad (5.4)$$

where $|\Psi(J, \Delta, h)\rangle$ is the ground state of $H_{\text{ANNNC}}(J, \Delta, h)$.

At $\Delta = 0$, the ANNNC model is just the clock model (3.46) and has an ordered phase with broken \mathbb{Z}_p symmetry at low h and a disordered symmetric phase at high h . For $p \leq 4$ these are separated by a second order phase transition and a critical point. For $p \geq 5$ they are separated by a critical phase between two BKT transitions. See Section 3.4.1 for details. Turning on Δ leads to a richer set of phases.

At $h = 0$ the ANNNC model consists of commuting terms and is thus purely classical. Note that, with $J > 0$ and $\Delta > 0$, the J term favours aligned nearest-neighbour spins (ferromagnetic ordering), whereas the Δ term favours anti-aligned (or anti-aligned as far as possible in the case of odd p) next-nearest-neighbour spins. Clearly, no single state is the ground state of both terms taken individually and the terms can be considered as competing with each other. This is an example of (classical) *frustration*, which can lead to complicated spatial structures, or to ground state degeneracies that diverge in the system size [154, 156].

5.2.1 Incommensurate order

The case $p = 2$ of the ANNNC model is known as the axial next nearest-neighbour Ising (ANNNI) model. We may write its Hamiltonian using Pauli matrices as

$$H_{\text{ANNNI}} = - \left[h \sum_{i=1}^N \sigma_i^x + J \sum_{i=1}^{N-1} \sigma_i^z \sigma_{i+1}^z - \Delta \sum_{i=1}^{N-2} \sigma_i^z \sigma_{i+2}^z \right]. \quad (5.5)$$

This model has received a lot of attention in the past because it exhibits, despite its simplicity, a rich phase structure including a commensurate-incommensurate transition and a BKT transition (see Section 2.2.2) as a result of the Δ interaction, which competes with the J term. It has mainly been studied in its classical, two-dimensional variant, which is related to the present one-dimensional quantum model by the quantum classical mapping described in Section 2.2.2. For a review of results for the classical ANNNI model, see [43]. The quantum ANNNI model (5.5) has been studied [90] using DMRG techniques (see Section 1.3) and is found to have a similar phase diagram to the classical model.

One of the most interesting features of the ANNNI model, expected to carry over to the more general ANNNC cases, is the presence of *incommensurate* order, which we define in Section 2.2.5. In the (1+1)D quantum ANNNI model, the incommensurately modulated quantity is the order parameter correlation function (see Section 1.2) which, in the ANNNC model formulation, is

$$C_{U,U^\dagger}(i, d) = \langle U_i U_{i+d}^\dagger \rangle - \langle U_i \rangle \langle U_{i+d}^\dagger \rangle, \quad (5.6)$$

where the disconnected contributions $\langle U_i \rangle$ are zero if the \mathbb{Z}_p symmetry is not broken. We expect to see similar phenomena in the ANNNC model for more general p , since the frustration responsible for the incommensurate order in the ANNNI model is also present for general p .

5.2.2 Dual nearest-neighbour model

A duality transformation, described for the clock model in [37] and for the ANNNI model in, for example [89], can also be applied to the ANNNC model (5.1). It is defined by

$$U_i \mapsto \prod_{j=1}^i V_j \quad i = 1, \dots, N, \quad (5.7)$$

$$V_i \mapsto U_i^\dagger U_{i+1}, \quad i = 1, \dots, N-1 \quad \text{and} \quad V_N \mapsto U_N, \quad (5.8)$$

where we can easily check that the exchange relation $UV = \omega VU$ is preserved

$$\left(\prod_{j=1}^i V_j \right) U_i^\dagger U_{i+1} = \omega U_i^\dagger U_{i+1} \left(\prod_{j=1}^i V_j \right), \quad (5.9)$$

and the new operators still commute for different sites as the old ones did. We further find $U_{i+1}^\dagger U_i \rightarrow V_i^\dagger$ for $i = 1, \dots, N-1$ such that, under the transformation, (5.1) becomes

$$H_{\text{ANNNC-D}} = -\frac{1}{2} \left[\sum_{i=1}^{N-1} (J V_i + h U_i U_{i+1}^\dagger) - \Delta \sum_{i=1}^{N-2} V_i V_{i+1} + \frac{h}{2} U_N \right] + h.c., \quad (5.10)$$

where we can check that the new Hamiltonian terms obey the same commutation relations as the old ones. We neglect the boundary term U_N since it is irrelevant in the thermodynamic limit $N \rightarrow \infty$. We refer to this model as the dual ANNNC model, or “ANNNC-D”. This nearest-neighbour model is interesting for two reasons: One is that it can be simulated more efficiently than the ANNNC model using MPS, where computational cost scales with the range of the terms in the Hamiltonian. Another is that this model describes the low energy physics of a potentially realisable mesoscopic device.

A key property of the ANNNC-D model is that the order parameter for the \mathbb{Z}_p symmetry of the ANNNC model transforms to the *string* operator

$$U_i \mapsto \prod_{j=1}^i V_j. \quad (5.11)$$

In the $p = 2$ ANNNI-D case, the incommensurate quantity of the floating phase is thus

$$C_{U,U^\dagger}(i, d) \mapsto \langle \prod_{j=i+1}^{i+d} V_j^\dagger \rangle - \langle \prod_{j=1}^i V_j \rangle \langle \prod_{j=1}^{i+d} V_j^\dagger \rangle, \quad (5.12)$$

which consists of expectation values of string operators. The commensurate-incommensurate transition is thus characterised by a nonlocal order parameter in the ANNNC-D model. This is interesting because it falls outside the domain of the Landau theory of symmetry-breaking transitions, which assumes a local order parameter (see Section 2.2.2).

5.2.3 Mesoscopic realisation

While the detailed physics of mesoscopic superconducting devices is beyond the scope of this thesis, we briefly sketch the principles of such a realisation of the ANNNC-D model (5.10) for even p , as it represents a connection between the ANNNC model and real systems with emergent parafermion modes. This proposal is the work of Michele Burrello and Emilio Cobanera, who collaborated with the present author on [155], and builds on earlier work on realising parafermionic degrees of freedom [104–107, 157].

A key ingredient is a theoretically predicted, but not yet experimentally observed form of condensed matter — the fractional topological insulator (FTI) [158]. A topological insulator is a solid phase with a spectral gap in the bulk, but an effective edge theory that hosts gapless modes (see also Chapter 4). Its bulk is thus an insulator, while its surface, or edge, is a conductor. The edge theories of topological insulators can involve exotic modes such as Majorana fermions [159] or, in the fractional case, parafermions [104] (see Chapter 3).

An FTI may host parafermion zero modes at interfaces produced between regions in proximity interaction with superconducting islands and regions in contact with insulating ferromagnets [104, 106], as illustrated in Figure 5.1. By alternating ferromagnets and superconducting islands, we may engineer two parafermionic modes per island i , $\Gamma_{i,1}$ and $\Gamma_{i,2}$, which obey the commutation relations of Section 3.2.3, except that we include a factor i in $\Gamma_{i,2}$ so that $(\Gamma_{i,2})^p = -\mathbb{I}$. We are limited in this setup to parafermions with an exchange phase

$$\omega = e^{i\frac{\pi}{m}}, \quad (5.13)$$

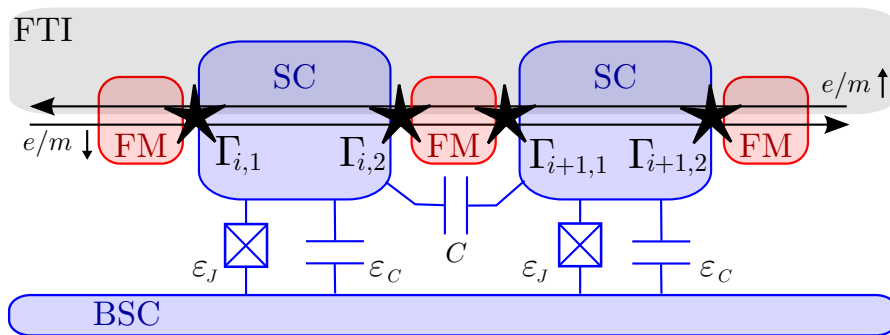


Figure 5.1: Sketch (by Michele Burrello) of a proposal for a mesoscopic implementation of the ANNNC-D model (5.10). The Γ represent parafermionic modes localised at the interfaces (stars) between ferromagnets (FM) and superconducting islands (SC) in proximity interaction with a fractional topological insulator (FTI), which supports fractionally charged (e/m for odd m), helical, gapless edge modes [158]. The SC's interact with each other via fractional Josephson tunnelling, as well as via an inter-island capacitance C . They are also coupled via a Josephson junction of strength ε_J and a capacitance ε_C to a background superconductor (BSC).

where m is odd, implying even $p = 2m$ in the notation of Section 3.2.3. The odd number m represents the fractional charge e/m of the edge modes of the FTI, with $m = 3$ ($p = 6$) being the first nontrivial case.

The parafermion modes are coupled via a fractional Josephson effect [105, 106] and receive an energy-level splitting via charging interactions of the islands [157], which are induced by coupling to a background superconductor via (strong) normal Josephson junctions and via a capacitance. A further capacitive coupling between neighbouring islands leads to an interaction between all four involved parafermion modes. For further details see [155] as well as [104, 106]. The effective low-energy Hamiltonian of the resulting system, with appropriate tuning, is

$$H_{\text{meso}} = -\frac{1}{2} \sum_{i=1}^L \left[h \Gamma_{i+1,1} \Gamma_{i,2}^\dagger + J \Gamma_{i,1}^\dagger \Gamma_{i,2} - \Delta \Gamma_{i,1}^\dagger \Gamma_{i,2} \Gamma_{i+1,1}^\dagger \Gamma_{i+1,2} \right] + h.c., \quad (5.14)$$

where h governs the tunnelling of fractional charges between islands, J the charging of islands with respect to the background superconductor, and Δ the inter-island capacitive interaction. L is the number of superconducting islands in the device. This Hamiltonian is related to (5.10) via a generalised Jordan-Wigner transformation

$$U_i = \Gamma_{i,1} \prod_{j=1}^{i-1} \Gamma_{j,2}^\dagger \Gamma_{j,1}, \quad (5.15)$$

$$V_i = \Gamma_{i,1}^\dagger \Gamma_{i,2}, \quad (5.16)$$

where, for even p , U_i and V_i are clock operators (3.41).

5.3 Numerical study

5.3.1 Methods

We sketch phase diagrams as described in Section 2.3, using block-uniform matrix product states (MPS), with block length L , as a variational class of states and finding effective ground states using the nonlinear conjugate gradient method. Setting $L > 1$ is necessary in this study, which includes antiferromagnet-like phases. We converge MPS ground states up to an effective energy gradient norm (1.83) of $< 10^{-6}$. For details of the algorithms, see Section 1.3. Note that the locations of phase transitions determined in this study are intended as a rough estimate.

We afford particular attention to the modulation wavevectors of correlation functions (5.6) and (5.12), since these are order parameters for the commensurate-incommensurate (C-IC) transitions observed in the $p = 2$ ANNNI model case. The wavevectors can be determined by fitting correlation functions using

$$f(d, k_0, A, \phi) \equiv Ae^{-d\lambda} \cos(k_0 d + \phi), \quad (5.17)$$

where the exponential decay need only be approximately reproduced in order to fit the wavevector k_0 accurately. Alternatively, since correlation functions are determined by the spectrum of the MPS transfer operator, we may obtain the wavevector of the slowest-decaying correlations from the complex phases of the largest eigenvalues (excluding the largest, which we require to be equal to one). See Section 1.3 for details.

5.3.2 Phase diagrams

We perform a preliminary scan of the (Δ, h) plane (with $J = 1$) in order to determine a rough phase structure, collecting more data to resolve areas that appear to contain finer features.

For $p = 3, 5, 6$ we generically find that turning on Δ draws out the clock model critical point ($p = 3$) or critical line ($p = 5, 6$) into a line or narrow critical phase, respectively, which appears to end in a point at a small value of Δ . After this point new phases open up, including a gapped commensurate phase at low h (except in the case of $p = 3$), a critical phase, and a disordered modulated phase at high h .

The disordered phases at low Δ also acquires modulated correlation functions of $U-U^\dagger$ above a certain value of h dependent on Δ . This line, known as a *disorder line* [160] coincides with a cusp maximum in the inverse correlation length ξ^{-1} , which we mark on the phase diagrams despite it not being a phase transition in the normal sense — the MPS ground state energy remains continuous and there is no indication of a higher order transition, which are accompanied by long-range correlations.

The structure is broadly similar to that observed for the ANNNI model [90], with the most significant differences observed for $p = 3$.

Phases for $p = 3$

Figure 5.2 represents our estimated phase diagram for the $p = 3$ case. At $\Delta = 0$ we confirm the known clock model phases, finding a symmetry-breaking transition at $h = 1$ corresponding to the global \mathbb{Z}_3 symmetry with order parameter U for the ANNNC model. A fit to the finite-entanglement scaling of ξ and S at the critical point (using $33 \leq D \leq 64$) estimates the central charge to be $c = 0.786(7)$, consistent with the exact result of $c = 4/5$, particularly considering that imperfect ground state convergence can alter the estimated c value.

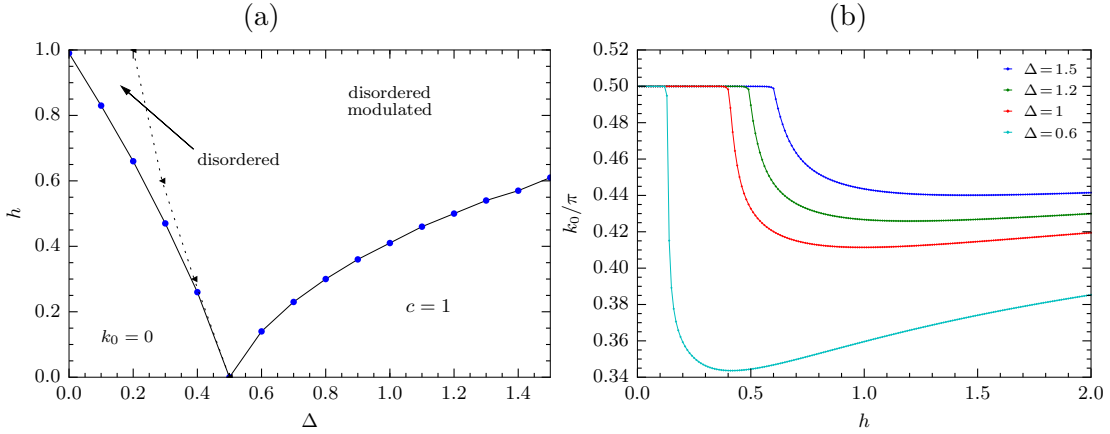


Figure 5.2: **(a)**: Phase diagram of the ANNNC(-D) model for $p = 3$. In the phase diagram, the black left-facing triangles are local cusp maxima (in the Δ direction) of the inverse correlation length $1/\xi$ of the ANNNC-D MPS ground state at $D = 9$. They mark the beginning of modulations in the correlation functions. The blue dots are cusp maxima (in the h direction) of the entanglement entropy S of the ANNNC-D MPS ground state at $D = 24$. The solid lines represent hypothesised phase transition lines, based on the numerical data. The low h phase for $\Delta > 0.5$ appears to be critical with central charge $c = 1$, separated from the high h phase by a second-order transition. See the main text for details of the numerical evidence. **(b)**: Order parameter modulation wavevectors k_0 along lines of h at selected $\Delta > 0.5$ for the ANNNC-D model at $D = 24$. The commensurate plateaus at $k_0 = \pi/2$ correspond to the critical $c = 1$ phase. The wavevector breaks away and begins to vary at the transition into the disordered modulated phase.

For $0 < \Delta < 0.5$ we find clear signatures of a second-order transition line extending the critical point of the clock model down towards $h = 0$ at $\Delta = 0.5$. At fixed D , these include a cusp maximum in the entanglement entropy $S(h)$ which coincides with a cusp minimum of the second energy derivative and a cusp minimum of the inverse correlation length ξ^{-1} . We find no evidence of further phase transitions for $0 < \Delta < 0.5$: The energy appears continuous throughout and there are no indications of further higher-order transitions (for example, $S(h)$ away from the critical point appears to fall off monotonically). See Figure 5.7 for example plots.

For $\Delta > 0.5$, we also observe a single second-order transition along a line emanating from the $h = 0, \Delta = 0.5$ point. In contrast to the $\Delta < 0.5$ structure, we find the low h phase to be gapless, with $S(D), \xi(D)$ scaling consistent with a CFT of central charge $c = 1$: We

fitted values at 6 different points $\Delta = -2, h = 0.1, 0.2, \dots, 0.6$ (each with 49 different bond-dimensions in the range $16 \leq D \leq 64$) with an average result of $c = 0.991(5)$. See Figure 5.8 for plots showing transition indicators. Within this critical phase, MPS correlation functions are modulated with fixed *commensurate* wavevector, in contrast to the high Δ critical phase of the ANNNI model, in which the wavevector varies continuously. This is shown in the wavevector plot of Figure 5.2. The high h phase beyond the second-order transition is the same incommensurate modulated disordered phase observed for $\Delta > 0.5$ beyond the disorder line.

That the entire low h region appears critical for $\Delta > 0.5$, and that the critical phase does *not* appear to be a floating incommensurate phase, sets the $p = 3$ case apart not only from the ANNNI model, but also from the $p = 5, 6$ cases, as shown below. Since this result appears exceptional, and since we are limited to small block sizes in the uniform MPS ansatz which may affect the ability to reproduce physical modulation behaviour, we also perform MPS simulations with open boundary conditions on a finite chain as a cross-check, using a one-site DMRG method in variational MPS formulation [2] together with imaginary time evolution [6, 63], both implemented in *evoMPS* [46], finding an entropy distribution consistent with a CFT of central charge $c = 1$, thus confirming the uniform MPS result. We also perform an extrapolation of $1/\xi$ to infinite D using the uniform MPS data, finding it to be consistent with $1/\xi \rightarrow 0$. Both results are shown in Figure 5.3.

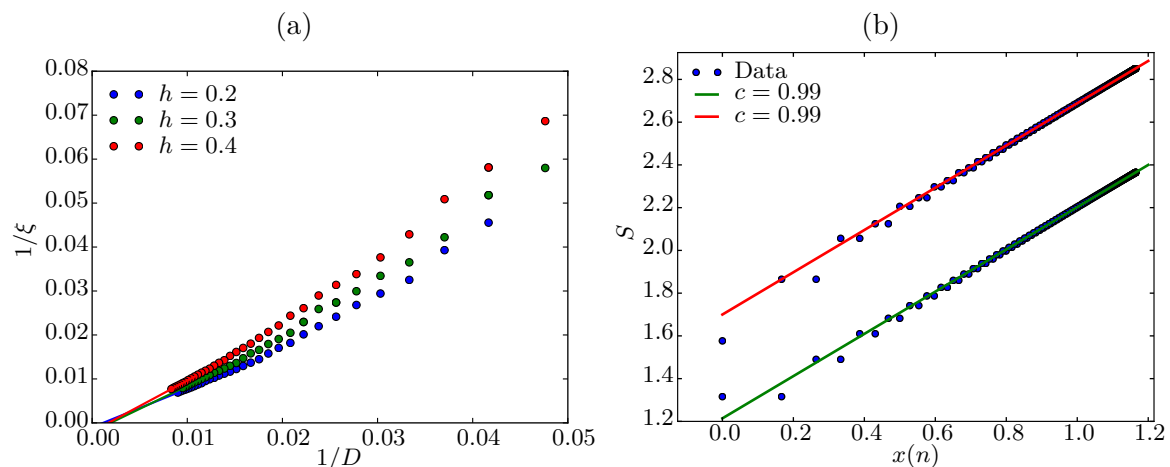


Figure 5.3: As further confirmation of the criticality of the low h , high Δ phase for $p = 3$, we plot in (a) the infinite- D linear extrapolation of the inverse correlation length $1/\xi$ for three different values of h at $\Delta = 1.5$, finding it to be consistent with $\xi \rightarrow 0$ as $D \rightarrow \infty$. In (b) we fit the spatially resolved entanglement entropy S for an open chain using the CFT prediction (2.15), finding it to be compatible with a CFT of central charge $c = 1$ for the even and odd sites separately. The open chain ground state was obtained for $D \leq 256$ and a chain length of 400 sites at $\Delta = 2, h = 0.1$. Fitted values of c are rounded to 2 decimal places. The x axis is a function of the site number n given by $x(n) \equiv 1/6 \log(N/\pi \sin(n\pi/N))$.

Phases for $p = 5, 6$

The $p = 5$ and $p = 6$ cases are very similar to each other. Like the $p = 3$ ANNNC model, the clock model phases persist for Δ below some small value. The clock model BKT transitions, however, are difficult to locate precisely since the energy second derivative does not diverge. BKT transitions are otherwise characterised by exponential scaling of the correlation length near the phase transition [87], but this is difficult to observe numerically, in this case due to finite-entanglement corrections. A more precise analysis using finite-entanglement scaling could be performed at the cost of additional computational time required to obtain data for many D along a line near the transition. One can also use the scaling of the entropy S together with the CFT prediction for ξ given $c = 1$ as in [90]. However, since we merely aim for a rough estimate of the transition location, this would be beyond the scope of this work. Instead we rely on fixed- D pseudo transitions as evidence which, combined with finite-entanglement scaling at isolated points to confirm or refute criticality, is enough to build up a convincing estimate of the phase diagram.

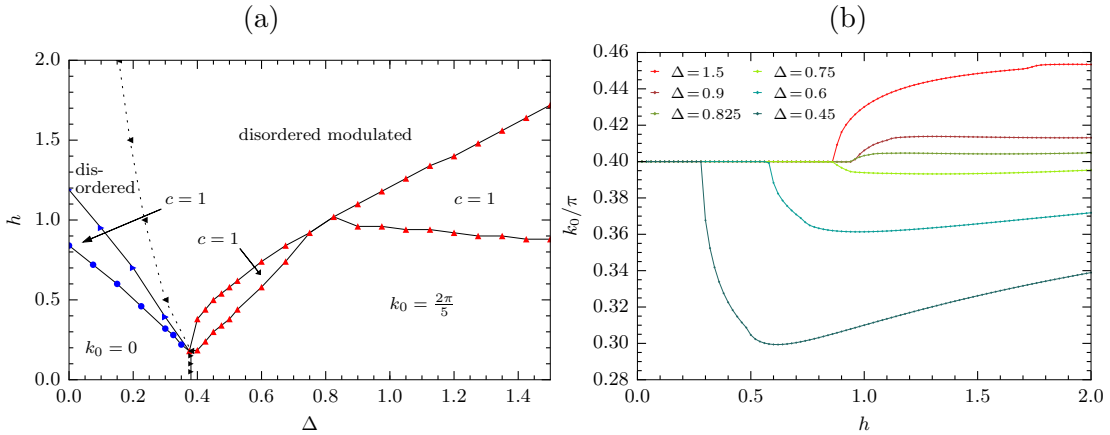


Figure 5.4: **(a)**: Phase diagram of the ANNNC(-D) model for $p = 5$. The blue dots and the blue right-facing triangles are maxima of the entanglement entropy S taken from the ANNNC-D model at $D = 20$ and the ordinary ANNNC model at $D = 16$, respectively. All further data is taken from the ANNNC-D model at $D = 20$. The red, up-facing triangles are local minima of the energy second derivative. The dashed “disorder line” is obtained from local maxima in the inverse correlation length $1/\xi$, as in Figure 5.2. The black, right-facing triangles mark discontinuities in the energy, the signature of a first-order phase transition. The solid lines represent hypothesised phase transition lines, based on the numerical data. The low h gapped phases are marked with their order parameter modulation wavevectors k_0 . Finite-entanglement scaling suggests the regions marked with $c = 1$ are critical and described by a CFT of central charge $c = 1$. See the main text for details. **(b)**: Order parameter modulation wavevectors k_0 along lines in h at selected $\Delta > 0.35$, taken from the ANNNC-D model at $D = 20$. The plateaus at low h represent the gapped $k_0 = 2\pi/5$ phase. The change in direction of the wavevector away from the commensurate value $2\pi/5$ appears to coincide with the narrowing of the high Δ critical phases to a line (or more likely a point, given enough resolution). This behaviour of the wavevector implies that there is a line of commensurate, locked modulation running from the $k_0 = 2\pi/5$ phase off to $h \rightarrow \infty$. Presumably the pinch point between the critical phases lies on this line.

For fixed D , we observe a cusp maximum in S corresponding to a finite-entanglement pseudo transition, marking one of the borders of a region of flat, and small inverse correlation length, as shown in Figure 5.7 for $\Delta = 0$. The region of flat ξ^{-1} exhibits CFT scaling with D consistent with a central charge of $c = 1$, which breaks down for lower and higher h as expected for the gapped ordered and disordered phases. This is consistent with the clock model critical phase. For $p = 5$, we obtain an average $c = 1.014(5)$ with five h values ($0.95 \leq h \leq 1.05$) and $17 \leq D \leq 64$. For $p = 6$, a set of five h values ($h = 0.9, 1.0, \dots, 1.3$) with $16 \leq D \leq 64$ gives $c = 1.006(8)$.

Interestingly, the maximum in S occurs on the low h side of the critical region for the ANNNC model, and on the high h side for the ANNNC-D model, such that we can use the entropy to approximately locate both transitions by simulating both models. We observe that the cusp maximum in S coincides with global symmetry-breaking, where the order parameter is U in both the ANNNC model and the ANNNC-D model. Note that the local maximum in S is a non-physical finite-entanglement effect — the physical value of S must diverge in the critical phase. It is also difficult to draw conclusions as to the symmetries of the true ground state in the critical phase from finite- D ground states, since it is also possible for non-physical symmetry breaking to take place if breaking a physical symmetry is an economical way of reducing the entanglement needed to approximate the state. This is more likely to happen if D is significantly lower than needed for an accurate representation of the state, which is always the case in a critical phase.

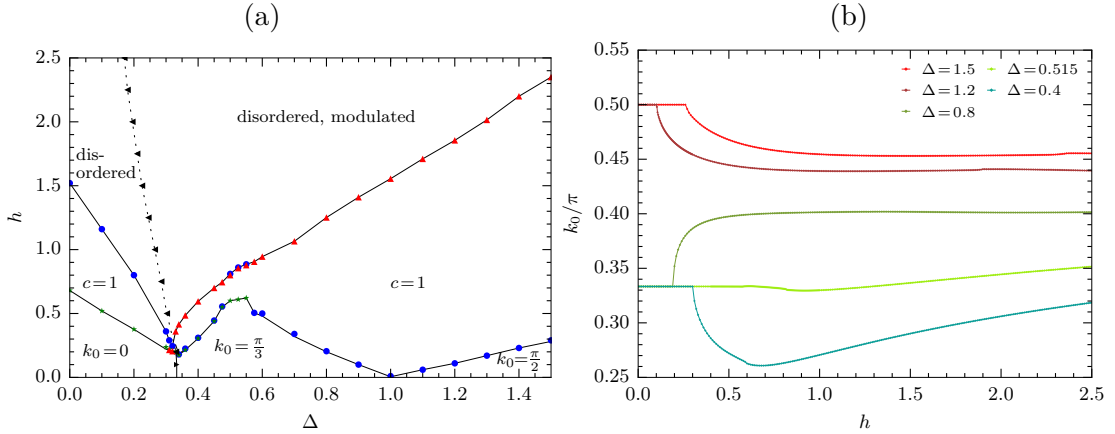


Figure 5.5: **(a)**: Phase diagram of the ANNNC-D model for $p = 6$. The markers are as in Figure 5.4, except for the addition of the green stars, which represent local maxima of the first derivative of $S(h)$. All data is from the ANNNC model at either $D = 16$ or $D = 24$. See the main text for details. **(b)**: Order parameter modulation wavevectors from the ANNNC-D model at $D = 24$. As in Figure 5.4, the crossing of the wavevector lines of the commensurate values $\pi/3$ coincides with a bottleneck of the high Δ critical phase(s) in the phase diagram. The bottleneck in the phase diagram does not appear to shrink to a point (or a line), at least in the finite- D MPS approximation.

For high Δ we see new gapped phases at low h , as observed for the ANNNI model. The first of these (in Δ) is separated from the ordered, ferromagnetic phase by a first order transition, as indicated by a discontinuous ground state energy. This transition line appears

to run from $h = 0$ up to a point where the clock phases all end. For $p = 5$ there is only one new gapped phase in the studied region, possessing a commensurate modulation of the order parameter expectation values with wavevector $k_0 = 2\pi/5$. The modulation pattern is helical in the complex plane. For $p = 6$ there is also a helically modulated phase for $\Delta < 1$, this time with $k_0 = \pi/3$, but also an $\uparrow\uparrow\downarrow\downarrow$ “antiphase” (where \uparrow represents one of the p spin directions ω^k and \downarrow represents its conjugate ω^{-k}) with $k_0 = \pi/2$ at $\Delta > 1$: See Figure 5.6.

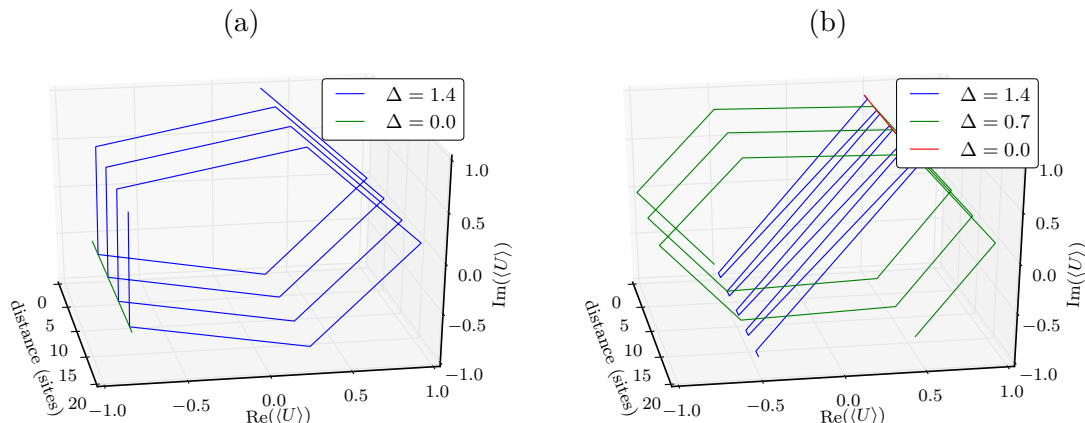


Figure 5.6: Ground state expectation values of the ANNNC order parameter at low field, $h = 0.05$, showing no modulation, or commensurate modulation, in the various gapped phases of **(a)** $p = 5$ and **(b)** $p = 6$. We observe helical modulation for $p = 5$, $\Delta = 1.4$ and $p = 6$, $\Delta = 0.7$ as well as “antiphase” modulation for $p = 6$, $\Delta = 1.4$. The case $\Delta = 0$ represents ferromagnetic ordering. Note that the data is discrete, with data points occurring at the bends in the lines.

At intermediate h we observe critical, floating phases in which the modulation wavevector of the order-parameter correlator varies continuously. The scaling of S and ξ with D is consistent with a central charge $c = 1$: For $p = 5$ a set of 8 fitted central charges in the high Δ critical region, along the interval $1.3 \leq \Delta \leq 2.0$ at $h = 1.2$, (using between 32 and 57 bond dimensions, $16 \leq D \leq 80$) give $c = 1.027(9)$. An additional fit in the intermediate critical region at $h = 0.66$, $\Delta = 0.6$ (with 25 points in $16 \leq D \leq 64$) gives $c = 1.029(5)$. For $p = 6$ we obtain central charge estimates along the interval $0.8 \leq \Delta \leq 1.5$ at $h = 0.75$ using 8 points with at least 32 bond dimensions each ($16 \leq D \leq 80$) finding $c = 1.028(7)$. A further fit at $h = 0.5$, $\Delta = 0.4$ (23 points, $16 \leq D \leq 60$) gives $c = 1.032(5)$. Note that the error noted is merely the uncertainty of the least-squares fit and does not include the error due to imperfect convergence of the approximate MPS ground state.

These phases differ significantly in extent between $p = 5$ and $p = 6$, but share an interesting bottleneck feature, which coincides with a sign flip in $k_0 - k_{0,c}$ within the floating phase, where $k_{0,c}$ is the commensurate wavevector of the low h phase and k_0 is the wavevector in the floating phase for the same value of Δ . This is clearly visible in the wavevector plots of Figures 5.4 and 5.5. It is unclear from the data collected, whether the bottleneck is a narrowing to a point or if the width of the critical phase remains finite. We expect the former, where the point would be located along a line of “accidentally commensurate” values of the wavevector connecting the commensurate low h phase with the disordered phase at

high h . In the $p = 6$ case of Figure 5.5 the lower h transition becomes less apparent near the bottleneck, making it more difficult to determine the precise phase diagram in this region.

We classify the low h transition between the commensurate phase(s) and the floating phase(s) to be second order, as indicated by a strong minimum of the second energy derivative. The high h transition is less clear, as for the BKT transitions of the clock model. The energy derivative for constant D does show some discontinuities, from which we take the one at largest h as a rough indicator of the transition location. This also corresponds to an increase in ξ^{-1} . See Figure 5.8. That there must be a transition is clear from the CFT scaling of S and ξ , which is present in the proposed critical region, but breaks down at high h .

5.3.3 CFT scaling dimensions and entanglement spectra

We have determined numerically, with a good degree of confidence, that the floating phases of the $p = 5$ and $p = 6$ ANNNC models are described by conformal field theories (CFT's) with central charge $c = 1$. There have been recent attempts to use DMRG/MPS approximate ground states to extract more details. In particular the *entanglement spectrum* has been investigated [161, 162] in several one-dimensional models, including the Bose-Hubbard chain and the XXZ model, which also have phases with $c = 1$, finding matches of the entanglement spectrum with the spectrum of the CFT describing these critical phases.

“Entanglement spectrum” is essentially another name for the singular values, or Schmidt coefficients, corresponding to a bipartite decomposition of a system. It is defined by

$$\Gamma_\alpha \equiv -\ln(\lambda_\alpha^2), \quad (5.18)$$

where λ_α are the Schmidt coefficients for the decomposition $|\psi\rangle = \sum_\alpha \lambda_\alpha |\phi_A^\alpha\rangle \otimes |\phi_B^\alpha\rangle$. The name comes from its interpretation as the spectrum of an “entanglement Hamiltonian” given by

$$\rho_A = e^{-H_\Gamma}, \quad (5.19)$$

where ρ_A is the reduced state on part A of the system, which can be diagonalised as $\rho_{\alpha\beta} = \delta_{\alpha\beta} \lambda_\alpha^2$. In the case of a CFT, the entanglement Hamiltonian has a simple expression in terms of the stress-energy tensor (see, for example [163]) and could reveal much about the CFT in question.

Following the approach of Läuchli in [161], we plot the entanglement spectrum for MPS approximate ground states from the floating phases of the $p = 5$ and $p = 6$ ANNNC models (5.1), resolving them by the expectation values of the global transformation (5.3) on the corresponding Schmidt vectors. This symmetry replaces the particle number symmetry of the Bose-Hubbard model. The expectation values of a global transformation on the Schmidt vectors can be computed from the block-uniform MPS as described Section 1.3.7. We find clear evidence of parabolic structures which, in contrast to the Bose-Hubbard case in [161], appear to wrap around the (finite) spectrum of V . We plot two examples in Figure 5.9, fitting the lowest-lying points (corresponding to the most significant Schmidt coefficients) using quadratic functions. We find the lower-lying points are well-described by the quadratic fits, suggesting that the entanglement spectrum also reflects a $c = 1$ compactified free boson

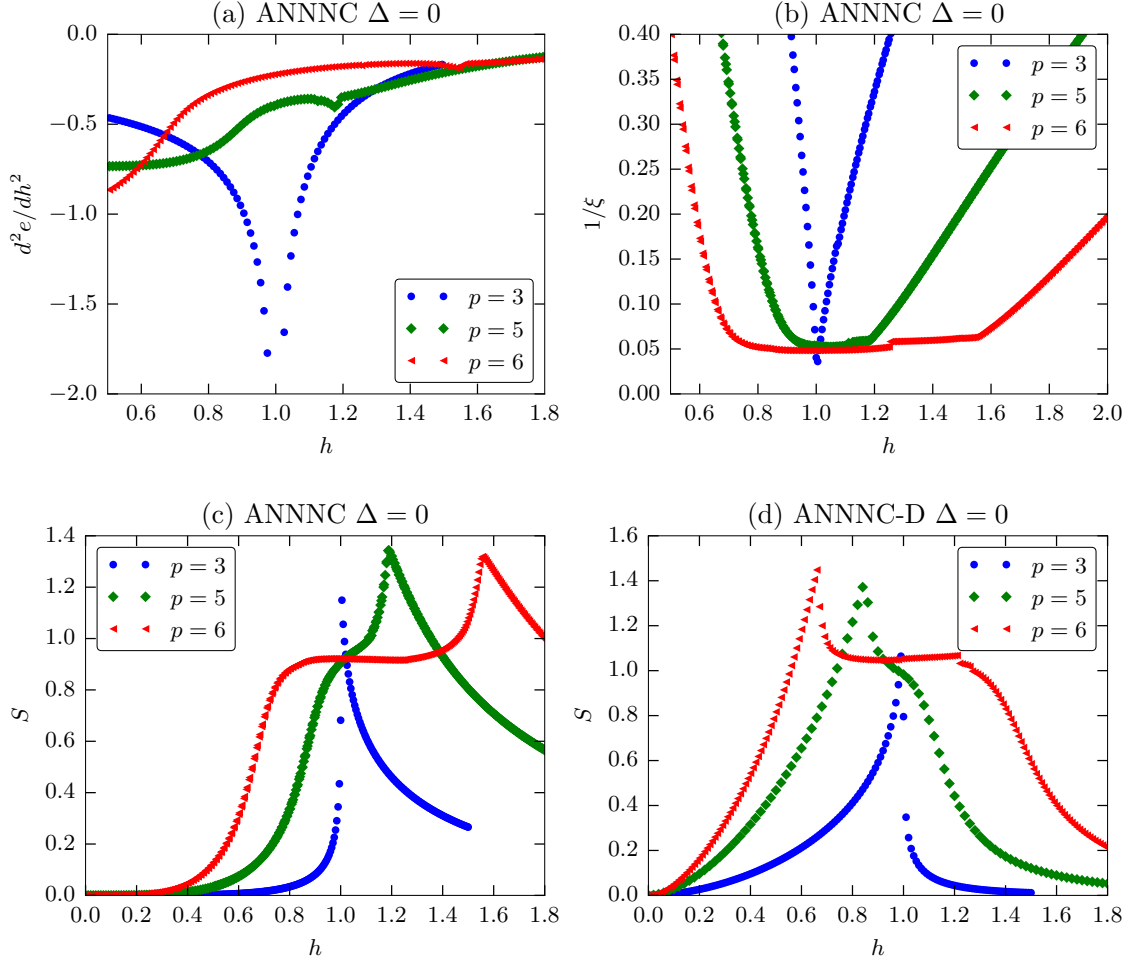


Figure 5.7: Phase transition indicators for the clock model ($\Delta = 0$). **(a)** The second derivative of the energy density, showing a clear signature of a second-order transition for $p = 3$, but showing mostly smooth behaviour for the known BKT transition cases of $p = 5, 6$. **(b)** The inverse correlation length $1/\xi$ suggesting a critical point for $p = 3$ and showing extended regions of long-range correlations for $p = 5, 6$, consistent with the critical phases expected. **(c)** The entanglement entropy S , showing a clear cusp maximum for all p . For $p = 5, 6$, we use this pseudo-transition as an estimate of the location of the high h BKT transition. **(d)** Entanglement entropy for the ANNNC-D model, showing a cusp maximum corresponding to the low h transition for the $p = 5, 6$ models. We find the maxima in the entropy correspond to a symmetry-breaking pseudo-transition in the MPS ground states, which occurs at the high h transition for the ANNNC model and at the low h transition for the ANNNC-D case. Note that the symmetry-breaking inside the critical phase may be a finite-entanglement artifact. Plots **(a),(b),(c)** use data from $D = 16$ approximate ground states of the ANNNC model. Plot **(d)** uses ANNNC-D data with $D = 24$ for $p = 3, 6$ and $D = 20$ for $p = 5$.

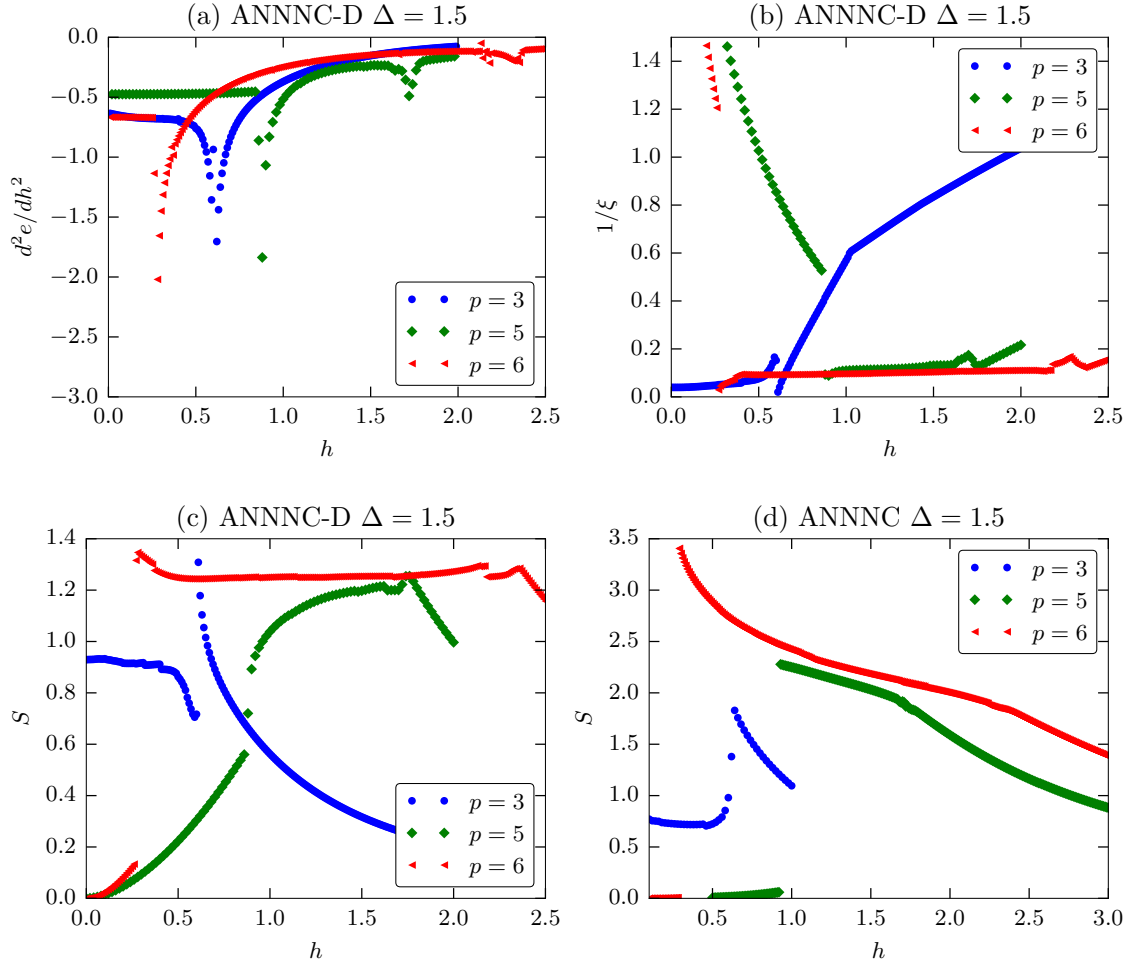


Figure 5.8: Phase transition indicators with frustration ($\Delta = 1.5$) from the ANNNC-D model (except plot **(d)**). **(a)** Second derivative of the energy density, showing clear signatures of one second order transition for $p = 3, 5, 6$. For $p = 5, 6$ there are also indications of a second transition at higher h . This transition may be a higher order one, such as a BKT transition. **(b)** Inverse correlation length $1/\xi$ indicating critical regions for all plotted p . In the case of $p = 3$, the region extends down to $h = 0$, whereas it gives way to a low h region with small correlation lengths for $p = 5, 6$, suggesting a gapped phase. **(c)** Entanglement entropy S showing cusp maxima, which suggests a phase transition. There is a clear signature of a high h transition for $p = 5, 6$. **(d)** S for the ANNNC model, showing different cusp maxima, this time suggesting a low h transition for $p = 5, 6$. Combined with **(c)**, we might use this data to estimate the location of the upper and lower transitions. Plots **(a)**, **(b)** and **(c)** use MPS ground states at $D = 24$ for $p = 3, 6$ and $D = 20$ for $p = 5$. Plot **(d)** uses $D = 16$ for all p .

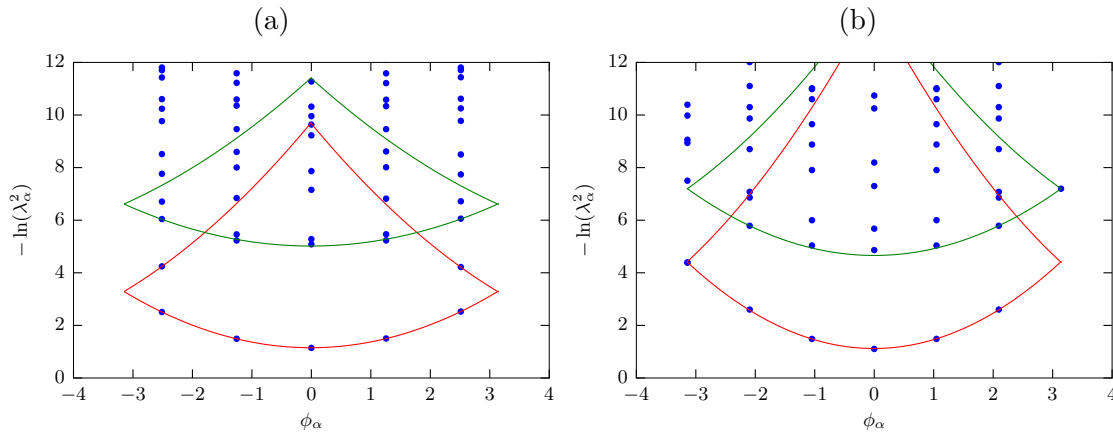


Figure 5.9: Entanglement spectra organised by the expectations values of the global symmetry transformation on the corresponding Schmidt vector $e^{i\phi_\alpha} = \langle \prod_{k=0}^{\infty} V_k \rangle_{R,\alpha}$. The Schmidt coefficients are λ_α . **(a)**: $p = 5$, $D = 80$, $L = 1$, $\Delta = 1.5$, $h = 1.2$. **(b)**: $p = 6$, $D = 60$, $L = 4$, $\Delta = 1.5$, $h = 1.5$. These points are within the floating phases of the $p = 5$ and $p = 6$ ANNNC models. The red and green lines are quadratic fits to the lowest and second-lowest points in each column, excluding wrapped points. Both clearly exhibit parabolic behaviour of the most significant Schmidt coefficients, suggesting that the interpretation of [161] can be applied and used to extract the scaling dimension.

CFT in the ANNNC case. As well as the cases illustrated in Figure 5.9, we also find that the entanglement spectrum, although it always appears to be symmetric about a certain angle, does not always have a point at the minimum of the lowest parabola.

We also use the procedure described in [161] to estimate the scaling dimension η of the first non-identity primary field, which determines the exponent of the algebraic decay of order-parameter correlations. We plot the values of η_{ES} obtained from the entanglement spectrum alongside η_C , the algebraic decay coefficient of the $U - U^\dagger$ correlation function, for $p = 5$ and $p = 6$ in Figure 5.10. For these plots, we only make use of data from entanglement spectra that include among their values the minimum of the parabola of best fit to the lowest-lying points. We plot η_C and $\eta_{C,D}$ obtained from simulations using the ANNNC model (5.1) and its dual (5.10) using a fixed bond dimension. We find good agreement between η_{ES} and the $\eta_{C,D}$, whereas the η_C results are qualitatively similar, but shifted to higher values. The good agreement in the former case is further evidence that the entanglement spectrum contains information about the CFT of the critical phase, which should have the same large-scale behaviour in the ANNNC-D and ANNNC models. The shift in the η_C results may be a result of a more complicated short range entanglement structure in the ANNNC model compared to the ANNNC-D model, leading to a poorer approximation of the ground state for a given value of D .

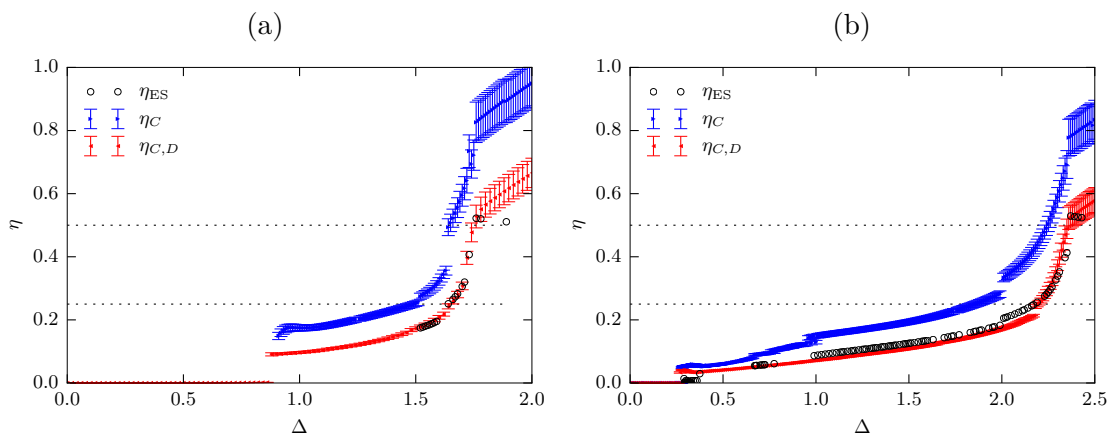


Figure 5.10: Numerical estimates of the scaling dimension η of the first non-identity primary field of the CFT describing the critical floating phases of the $p = 5$ and $p = 6$ ANNNC models. **(a)**: $p = 5$, $D = 20$. **(b)**: $p = 6$, $D = 24$. For comparison, we plot the value obtained from the V -resolved entanglement spectrum of the ANNNC model η_{ES} , as well as values obtained as the algebraic decay exponent for order parameter correlator of the ANNNC model η_C and of the ANNNC-D model $\eta_{C,D}$. We observe good quantitative agreement between η_{ES} and $\eta_{C,D}$ within the floating phases, as well as good qualitative agreement with η_C . We interpret this result in the main text.

5.4 Discussion and conclusions

We have shown that incommensurate order appears for all studied p as the strength of the next-nearest-neighbour interaction term in (5.1) is increased. Our approximate phase diagrams have a similar form to that of the known $p = 2$ ANNNI case [90], with the differences in the cases $p = 5$ and $p = 6$ being limited to the size of the floating phase and the form of the low-field phase(s). Since the $p = 6$ case is relevant for the experimental setup discussed in Section 5.2.3, our results lead to a wide range of interesting experimental predictions. To more precisely determine how the system behaves in experiments, particularly in the incommensurate phases due to the restrictions on the wavevector imposed by a finite length, numerical studies on finite systems may be helpful.

Perhaps the most interesting finding in our study is the appearance for $p = 3$, at $\Delta > 0.5$, of a commensurate gapless phase with central charge $c = 1$ extending all the way down to the classical $h = 0$ line. In the other cases studied, as well as in the ANNNI model, the low- h phase is gapped and the gapless phase(s) at intermediate h are incommensurate floating phases. In searching for an explanation, we note that the $h = 0$ ground state of the $p = 3$ model differs from the $p = 2, 5, 6$ cases in an interesting way. In all cases, for small Δ the configuration is ferromagnetic and for larger Δ it becomes energetically more favourable to build a commensurate, modulated structure. However, despite the possibility of a “helical” structure as formed for $p = 5$ and $p = 6$, an antiphase-type configuration similar to those of the $p = 2$ and the high- Δ $p = 6$ models, has lower energy. In contrast to $p = 2$ and $p = 6$, however, the antiferromagnetic term ($+U_i U_j^\dagger + h.c.$) has an additional ground state degeneracy due to p being odd: If we fix spin i to have value 1 then the ground space is

spanned by $|1\rangle_i|\omega\rangle_j$ and $|1\rangle_i|\omega^2\rangle_j$. As such, the overall ground state has the form

$$|\psi_0\rangle = |\dots aa bb cc dd \dots\rangle, \quad a, b, c, d \in \{1, \omega, \omega^2\}, \quad (5.20)$$

where neighbouring pairs differ in spin ($a \neq b$, $b \neq c$, $c \neq d$, and so on). The number of such states grows exponentially with the chain length N , so that the infinite system has an infinitely degenerate ground state. This is a typical feature of classically frustrated systems, and sets the $p = 3$ case apart from $p = 2, 5, 6$, which maintain a small, finite degeneracy corresponding to a global symmetry at $h = 0$ for all investigated Δ . It is possible that the low- h commensurate gapless phase of the $p = 3$ model exists as a result of this difference at $h = 0$. We may speculate that the gapless phase is a quantum spin liquid (QSL) [44], a type of phase that can arise when adding quantum fluctuations to a frustrated system. A feature of QSL states is, however, that the magnetisation vanishes. In our case, the MPS ground states have a small average magnetisation $\langle U \rangle$ (where the average is taken over a block of size L). Nevertheless, this does not rule out the hypothesis, since the symmetry-breaking may be a nonphysical finite-entanglement effect (see Section 2.3). Indeed, a preliminary analysis shows that the average magnetisation approaches zero as D increases.

We have also seen that the entanglement spectrum of the ANNNC model in the incommensurate floating phase shows structure consistent with a free bosonic CFT [161], extracting a value for the scaling dimension that shows good agreement with fits to correlation functions. This also constitutes evidence that quantum fluctuations lead to an emergent $U(1)$ symmetry in critical phases, despite the discrete \mathbb{Z}_p symmetry of the underlying clock degrees of freedom [37].

Chapter 6

Lattice gauge theory

6.1 Introduction

In this chapter we present the tools needed to understand Hamiltonian lattice gauge theory. Beginning with an introduction to gauge theories, we cover some basic group theory before setting the scene for Hamiltonian lattice gauge theory by describing its Hilbert space and a number of important operators. We then define the theory, following Kogut and Susskind [164], ultimately describing how the graph on which a lattice gauge theory is defined can be manipulated using unitary “parallel transport” operations. The contents of this chapter is intended to motivate and set up the theory for the study of the nonabelian quantum rotor model in Chapter 7.

Most of this chapter follows [165], which makes use of the same mathematical framework, initially developed for that project by Tobias Osborne. A novel addition is the derivation of important operators in terms of a Fourier basis, which was necessary for the numerical implementation of Chapter 7. The concepts of manipulating graphs in lattice gauge theory using parallel transport operations is not new, and is also described in slightly different language in [166].

6.2 Gauge theories

Gauge theories are quantum field theories whose physics is invariant under local *gauge transformations*. Such theories arise often in physics, and are connected to a relativity principle: We wish to avoid physical predictions that depend on an arbitrary (local) choice of reference system: In general relativity, a crucial feature is the invariance of physics under a local choice of basis for spacetime [167]. Similarly, in a quantum gauge theory the quantum field has an “internal” degree of freedom whose absolute value at any point in spacetime is not physically observable, while its changing value along a path in spacetime, for example around a loop, can be.

Gauge fields are central to the Standard Model of particle physics [81]: Together with corresponding *matter fields*, such as the Dirac field of fermions, they are responsible for the electroweak interaction as well as the strong interaction. Here, the particle excitations of

the gauge field obey bosonic statistics and are known as *gauge bosons*, of which the best known example is the *photon*, which is the gauge boson of quantum electrodynamics (QED).

Intriguingly, one is *forced* to include a gauge field with its own dynamics if one wishes to construct a quantum field theory of matter that is invariant under local transformations. For example, say we have a complex quantum field $\psi(x)$ whose dynamics are governed by quadratic terms such as $\overline{\psi(x)}\psi(x)$, or $\overline{\psi(x)}\partial_\mu\psi(x)$, and where all physical observables also involve quadratic, or even-power terms in the field. Clearly, all physical predictions of this theory are independent of an overall phase factor

$$\psi(x) \mapsto e^{i\theta}\psi(x). \quad (6.1)$$

This is a *global* transformation (θ is not a function of x). However, we may also consider theories whose predictions are invariant under *local* transformations

$$\psi(x) \mapsto e^{i\theta(x)}\psi(x). \quad (6.2)$$

We can think of a local phase shift as a local change of coordinates — we are shifting the “zero” in our reference system of phases. If we now consider the terms governing the dynamics of the theory, we quickly find that any derivative terms, such as $\overline{\psi(x)}\partial_\mu\psi(x)$, will need to be modified to keep track of these local phase choices, since they will otherwise pick up a dependence on them from

$$\partial_x e^{i\theta(x)} \neq 0. \quad (6.3)$$

One way to do this is to introduce an extra field A_μ , whose job it is to translate between these local “coordinate systems” so that distant phases can be compared properly. If we require that the new field transform as

$$A_\mu \mapsto A_\mu + \partial_\mu\theta(x), \quad (6.4)$$

we can then swap the derivative in the equations of motion for the *covariant derivative*

$$D_\mu \equiv \partial_\mu - iA_\mu(x), \quad (6.5)$$

giving

$$\overline{\psi(x)}D_\mu\psi(x) = \overline{\psi(x)}[\partial_\mu - iA_\mu(x)]\psi(x), \quad (6.6)$$

which, a little calculation shows, is invariant under transformations of the field and gauge field, (6.2) and (6.4). This procedure is well known in differential geometry, in which context the field A_μ is called the *connection* [81]. Now, in addition to restoring gauge invariance, the gauge field A_μ can have consequences for the dynamics of the $\psi(x)$ field. Indeed, in some cases it is “forced”, if we require certain symmetries to be maintained, to have its own physics [81]! For instance, if we let $\psi(x)$ be the Dirac field of spinors in four spacetime dimensions, we find that the corresponding gauge field A_μ cannot be neglected in calculating physical observables and is thus physically relevant. Further, one of the simplest forms for the dynamics of A_μ is equivalent to Maxwell’s equations, where we recognise A_μ as the “vector potential” from classical, Lorentz-invariant electrodynamics. The resulting gauge theory is QED.

Associated with each gauge theory is a *gauge group* G describing the local symmetry. The gauge field takes values in the Lie algebra associated with G . In the case of QED, G is the group of phases $U(1)$, which is abelian, and whose Lie algebra is the real numbers so that $A_\mu \in \mathbb{R}$. Naturally, one could consider matter fields that transform under the actions of other groups. Indeed, Yang and Mills generalised gauge theories to nonabelian gauge groups, such as $SU(N)$ in 1954 [168]. Although these Yang-Mills theories were initially seen as a curiosity, today they make up the fundamental gauge theories of the Standard Model, with the abelian theory of QED emerging from the nonabelian electroweak theory, which has $G \cong SU(2)$, as a result of *symmetry breaking* [81].

Importantly, nonabelian gauge theories can exhibit very different physics to abelian theories like electrodynamics. Crucially for the strong interaction, described by a gauge theory with $G \cong SU(3)$, called quantum chromodynamics (QCD) [81, 169], the gauge field potential for separated charges *grows* linearly with distance, explaining the confinement of quarks [170]. Unfortunately, despite its simple formulation and large gauge symmetry group, Yang-Mills theory has not been exactly solved. Indeed, a prize is available for anyone who is able to prove rigorously that it has a mass gap [171], which would be the case if it is confining at all energy scales.

Predictions in Yang-Mills theory can be made using perturbative scattering theory for high energies, where the effective coupling becomes small (asymptotic freedom), and using strong coupling expansions together with a lattice discretisation for low energy, long distance behaviour [45]. It is also possible to perform numerical simulations on the lattice using Monte Carlo sampling techniques, which has provided excellent confirmation of the spectrum of light hadrons [172], for example.

Working with the theory on a lattice has the natural advantage of imposing a momentum cutoff, albeit at the expense of abandoning Lorentz invariance. This is convenient since in a quantum field theory objects typically become well-defined only with the use of a so-called *regularisation* scheme [80, 81], of which a momentum cutoff is one example. The reason is that certain integrals representing physical quantities diverge, an obvious risk when they are carried out over the continuous and infinite space in which a quantum field is supposed to live. Although a cause for much head-scratching in the early days of quantum field theory, today this phenomenon is usually seen as an indication that the theory at hand breaks down at some point, typically as we consider ever higher energies. Such an “ultraviolet” divergence tells us that our theory cannot describe physics at all energies. However, this does not prevent it from being a good *effective* theory at lower energies, and indeed we have every reason to expect the highly successful quantum field theory of the Standard Model to break down at sufficiently high energies since gravity, usually neglected in particle physics, must eventually play a role.

A lattice discretisation not only regularises the theory, it also brings it into a form convenient for the application of known discrete numerical and analytical methods, such as those of tensor network states (see Chapter 1). For these reasons, we work in the following with lattice-discretised Yang-Mills theory. In particular we make space discrete, leaving time continuous, working with the Hamiltonian formulation due to Kogut and Susskind [164].

Lattice gauge theory associates a Hilbert space \mathcal{H} , a Hamiltonian H , and a subspace

of physical (gauge invariant) states $\mathcal{H}_{\text{phys}}$, with a lattice or, more generally, a *graph*. The Hilbert space is composed of spaces associated with the *edges* of the graph

$$\mathcal{H} = \bigotimes_{e \in E} L^2(G), \quad (6.7)$$

where $L^2(G)$ denotes the space of square-integrable functions of the gauge group G . Before we examine the Kogut-Susskind Hamiltonian, we review some results of group theory and set up some useful operators on $L^2(G)$.

6.3 Some group theory

A group G is a set of elements $g \in G$ together with a product operation, under which the set is *closed*, meaning that taking the product of two elements of the set can only ever produce other elements of the set $gh \in G \quad \forall g, h \in G$. Groups are also required to have an *identity* element \mathbb{I} , such that $g\mathbb{I} = g \quad \forall g \in G$, and an *inverse element* g^{-1} for each element g such that $gg^{-1} = \mathbb{I}$. For more, see for example [173].

In the following, we deal with “matrix groups”, which are sets of matrices closed under the usual matrix multiplication operation. In particular, we consider compact Lie groups G [174]. A Lie group is a continuous group that is also a differentiable manifold, implying that one can define a *tangent space* associated with each element. We focus in particular on two Lie groups relevant for gauge theories: $U(1)$ and $SU(2)$ [174]. The former may be defined as

$$U(1) \equiv \left\{ e^{i\theta} \mid \theta \in [0, 2\pi) \right\} \cong \left\{ z \mid z \in \mathbb{C}, |z|^2 = 1 \right\}, \quad (6.8)$$

where the first definition is in terms of positions on a unit circle, clarifying why $U(1)$ is also called the “circle group”, and the second explains the name “ $U(1)$ ”: It is the group of 1×1 unitary matrices. This group is clearly abelian (its elements commute). The simplest relevant nonabelian group is $SU(2)$, which we define as

$$SU(2) \equiv \left\{ \begin{pmatrix} \alpha & -\bar{\beta} \\ \beta & \bar{\alpha} \end{pmatrix} \mid \alpha, \beta \in \mathbb{C}, |\alpha|^2 + |\beta|^2 = 1 \right\}. \quad (6.9)$$

This is the group of unitary 2×2 matrices with determinant 1. It is interesting to note that $SU(2)$ is diffeomorphic to the 3-sphere S^3 [174], which can be seen in the following way. If we define a basis for 2×2 matrices

$$\tau^0 = \begin{pmatrix} 1 & 0 \\ 0 & 1 \end{pmatrix}, \quad \tau^1 = i \begin{pmatrix} 0 & 1 \\ 1 & 0 \end{pmatrix}, \quad \tau^2 = i \begin{pmatrix} 0 & -i \\ i & 0 \end{pmatrix}, \quad \text{and} \quad \tau^3 = i \begin{pmatrix} 1 & 0 \\ 0 & -1 \end{pmatrix}, \quad (6.10)$$

where we can verify that $\text{tr}(\tau^{\mu\dagger}\tau^\nu) = 2\delta^{\mu\nu}$, every 2×2 unitary matrix of determinant 1 can be uniquely represented as

$$\begin{pmatrix} \alpha & -\bar{\beta} \\ \beta & \bar{\alpha} \end{pmatrix} = \sum_{\mu=0}^3 n_\mu \tau^\mu \quad (6.11)$$

by setting

$$n^T = (\operatorname{Re}(\alpha), \operatorname{Im}(\beta), -\operatorname{Re}(\beta), \operatorname{Im}(\alpha)), \quad (6.12)$$

where $|\alpha|^2 + |\beta|^2 = 1$ implies $|n|^2 = 1$. In other words, elements of $SU(2)$ are in one-to-one correspondence with vectors in \mathbb{R}^4 of modulus 1, which lie on the unit hypersphere of \mathbb{R}^4 . Furthermore, we find that the product $SU(2) \times SU(2)$ (also known as $\operatorname{Spin}(4)$) can be mapped to the group $SO(4)$ of rotations in \mathbb{R}^4 . To see this, take any element $g \in SU(2)$, which represents a point on the unit hypersphere, and act on it with an element $(h_1, h_2) \in SU(2) \times SU(2)$ from the left and right

$$g \mapsto h_1 g h_2^{-1}. \quad (6.13)$$

This gives us a new element of $SU(2)$, and therefore a new point on the unit hypersphere. Hence each element of $SU(2) \times SU(2)$ is a rotation in \mathbb{R}^4 . However, there are two elements in $SU(2) \times SU(2)$ for each such rotation, since we can do $h_1 \mapsto -h_1$ together with $h_2 \mapsto -h_2$ without changing the rotation $h_1 g h_2^{-1}$: $SU(2) \times SU(2)$ is the *double cover* of $SO(4)$ [175].

6.3.1 Irreducible representations and the Peter-Weyl theorem

It is possible to represent a group on different vector spaces with an appropriate choice of linear operation implementing the group product. We work with compact Lie groups G , which have nontrivial finite-dimensional matrix representations [174], meaning there are functions $r : G \rightarrow M_d$, with d finite, such that $r(g)r(h) = r(gh)$ for all $g, h \in G$. $r(g)$ that are *not* the trivial representation $r(g) = \mathbb{I}_d \quad \forall g \in G$. We restrict ourselves to *unitary* representations $r(g)r^\dagger(g) = r^\dagger(g)r(g) = \mathbb{I}$, which exist for all compact Lie groups [174]. A representation may be *reducible*, meaning we can find a basis for the matrices $r(g)$ such that $r(g)$ has the same nontrivial block-diagonal structure for all $g \in G$, or it may be *irreducible* [174]. An irreducible representation, or *irrep*, cannot be block-diagonalised in this way. This implies that any reducible representation can be decomposed into a direct sum of irreducible representations which can itself be decomposed no further.

Given that all representations can be written in terms of irreps, one might suspect that the irreps form a useful “basis” for more general purposes. In fact, the Peter-Weyl theorem [175, 176] tells us that the irreps form an orthonormal basis for square-integrable functions of G :

$$L^2(G) \cong \bigoplus_{l \in \text{irreps}} V_l \otimes V_l^*, \quad (6.14)$$

where V_l is a d_l -dimensional vector space associated on which the matrix irrep l acts and V_l^* is its dual. Integration over the group G is performed using the left and right translation-invariant Haar measure dg [175], which is invariant under group multiplication from the left and right:

$$\int_G dg f(g) = \int_G dg f(gh) = \int_G dg f(hg). \quad (6.15)$$

The Peter-Weyl theorem can be stated more precisely as:

Theorem 6.3.1 (Peter-Weyl). *Let G be a compact group. Let the matrix coefficients be the matrix elements, as functions $G \rightarrow \mathbb{C}$, of an irreducible finite-dimensional matrix representation of G in a chosen basis.*

1. *The set of matrix coefficients of all finite-dimensional irreps is dense in $L^2(G)$.*
2. *Let $\{t^l\}_l$ denote a set of mutually inequivalent unitary irreps of G and let $\{t^l_{jk}(g)\}_{jk}$ be the matrix coefficients of irrep l . Then $\{\sqrt{d_l} t^l_{jk}\}_{ljk}$ is an orthonormal basis for $L^2(G)$, where d_l is the dimension of irrep t^l .*

In the case of $G = U(1)$, (6.14) is just the Fourier decomposition of functions on the circle: All irreps of $U(1)$ are one-dimensional, and a canonical choice is $t^n(\theta) = e^{in\theta}$, for $\theta \in [-\pi, \pi)$ and $n \in \mathbb{Z}$. The irreps of $SU(2)$ are familiar in physics as the set of possible *spins* assigned to particles. Spin-0 particles transform under the $l = 0$ (trivial) representation of $SU(2)$, spin- $\frac{1}{2}$ under the $l = \frac{1}{2}$ irrep, and so on. The Peter-Weyl theorem proves a way of generalising the Fourier series to functions of compact groups.

6.3.2 Lie algebra and generators of a Lie group

Another important property of Lie groups is that they are locally *generated* by a Lie algebra [174], which is the tangent space of the group at the identity element. In particular, the irreducible representation of any element in the matrix Lie groups $U(1)$ and $SU(2)$ can be written using the matrix exponential [174] as

$$t^l(g) = \exp\left(i \sum_{\alpha} \theta_{\alpha} \lambda_{\alpha}^l\right), \quad (6.16)$$

where $\theta_{\alpha} \in \mathbb{R}$ and λ_{α}^l are the $d_l \times d_l$ Hermitian *generators* for irrep l . These satisfy commutation relations

$$[\lambda_{\alpha}^l, \lambda_{\beta}^l] = i \sum_{\gamma} f_{\alpha\beta\gamma} \lambda_{\gamma}^l, \quad (6.17)$$

where $f_{\alpha\beta\gamma}$ are called the structure constants [174]. In the case of the spin-half representation of $SU(2)$, the generators are the Pauli matrices $\lambda_{\alpha}^{1/2} = \frac{1}{2}\sigma_{\alpha}$ ($\alpha = 1 \dots 3$) and the structure constants are $f_{\alpha\beta\gamma} = \frac{1}{2}\epsilon_{\alpha\beta\gamma}$, where ϵ is the Levi-Civita symbol. In the case of $U(1)$, the generator of irrep n is the integer n (a 1×1 Hermitian matrix): $\lambda^n = n$.

6.4 Bases for $L^2(G)$

The Fourier basis for the Hilbert space $L^2(G)$ is invaluable for numerical applications, as it is countable for compact groups. In the following we use the Dirac bra-ket notation, denoting Fourier basis elements as

$$|jk\rangle_l \cong \sqrt{d_l} t^l_{jk}, \quad (6.18)$$

with l denoting the irrep and j, k referring to a particular matrix element. With this notation the orthogonality property reads

$${}_{l'} \langle j' k' | j k \rangle_l = \delta_{ll'} \delta_{jj'} \delta_{kk'}. \quad (6.19)$$

In the case of $G \cong U(1)$, where all irreps are one-dimensional, we use a more compact notation

$$|n\rangle \cong t^n = e^{in}, \quad (6.20)$$

where $\langle n | m \rangle = \delta_{nm}$ and we have used n instead of l to denote the irrep because there is an irrep for every $n \in \mathbb{Z}$. We may also define a ‘‘position basis’’ $|g\rangle$ such that

$$\int_G dg dh \langle g | h \rangle = \int_G dg dh \delta(g - h) = 1, \quad (6.21)$$

where $\delta(g - h)$ is a Dirac delta on G defined such that

$$\int_G dg f(g) \delta(g - h) = f(h). \quad (6.22)$$

In the sequel, we drop the subscript G on the integration symbol.

The Fourier basis elements can be written in terms of the position basis as

$$|jk\rangle_l = \sqrt{d_l} \int dg t_{jk}^l(g) |g\rangle, \quad (6.23)$$

where we can check that, due to the orthogonality of the basis $\{\sqrt{d_l} t_{jk}^l\}_{ljk}$,

$${}_{l'} \langle j' k' | j k \rangle_l = \sqrt{d_l d_{l'}} \int dg \overline{t_{j'k'}^{l'}(g)} t_{jk}^l(g) = \delta_{ll'} \delta_{jj'} \delta_{kk'}. \quad (6.24)$$

6.5 Operators on $L^2(G)$

Here we define the operators on $L^2(G)$ that are needed to discuss lattice gauge theory. To implement left and right multiplication, we define unitary *rotation* operators \widehat{L} and \widehat{R} acting on the position basis as

$$\widehat{L}_h |g\rangle = |hg\rangle \quad \text{and} \quad \widehat{R}_h |g\rangle = |gh^{-1}\rangle. \quad (6.25)$$

These fulfil

$$[\widehat{L}_g, \widehat{R}_h] = 0, \quad \widehat{L}_g^\dagger = \widehat{L}_{g^{-1}}, \quad \widehat{R}_g^\dagger = \widehat{R}_{g^{-1}}, \quad \widehat{L}_g \widehat{L}_h = \widehat{L}_{gh}, \quad \widehat{R}_g \widehat{R}_h = \widehat{R}_{gh}. \quad (6.26)$$

We also define a position operators \widehat{u}_{jk}^l , each diagonal in the position basis, with eigenvalues corresponding to the matrix entry i, j of the l th irrep of G :

$$\widehat{u}_{jk}^l |g\rangle := t_{jk}^l(g) |g\rangle. \quad (6.27)$$

Where we do not specify the irrep on objects such as \widehat{u}_{jk} and $t_{jk}(g)$, we assume the fundamental, or defining irrep of the group. For $U(1)$ this is the $n = 1$ irrep $e^{i\theta}$ used in (6.8)

and for $SU(2)$ it is the spin-half representation of 2×2 unitary matrices used in (6.9). We further define $\hat{\mathbf{u}}$ to denote the matrix of operators

$$\hat{\mathbf{u}}_{jk} \equiv [\hat{u}_{jk}]_{jk}, \quad \hat{\mathbf{u}}_{jk}^\dagger \equiv [\hat{u}_{kj}^\dagger]_{jk}, \quad (6.28)$$

with standard matrix multiplication implying, for example, that

$$[\hat{\mathbf{u}}_1 \hat{\mathbf{u}}_2]_{jk} = \sum_{k'} \hat{u}_{1,jk'} \hat{u}_{2,k'k} \quad \text{and} \quad (6.29)$$

$$[\hat{\mathbf{u}}_1^\dagger \hat{\mathbf{u}}_2]_{jk} = \sum_{k'} \hat{u}_{1,k'j}^\dagger \hat{u}_{2,k'k}, \quad (6.30)$$

where the counterintuitive ordering of indices on line two is a consequence of the transpose in $\hat{\mathbf{u}}^\dagger$. The $\hat{\mathbf{u}}$ operator interacts with rotations as

$$\begin{aligned} L_g^\dagger \hat{\mathbf{u}} L_g &= t(g) \hat{\mathbf{u}} \quad \text{and} \\ R_g^\dagger \hat{\mathbf{u}} R_g &= \hat{\mathbf{u}} t(g^{-1}), \end{aligned} \quad (6.31)$$

where $t(g)$ undergoes matrix multiplication with $\hat{\mathbf{u}}$. Also, we have the identity

$$[\hat{\mathbf{u}}^\dagger \hat{\mathbf{u}}]_{jk} = \hat{\mathbb{I}} \delta_{jk}, \quad (6.32)$$

as can be verified by acting on position basis states.

We may define ‘‘momentum’’ operators, corresponding to the generators of the group, as infinitesimal rotations from the left and right:

$$\hat{p}_\alpha^L \equiv i \left. \frac{d}{d\epsilon} \hat{L}_{e^{i\epsilon\lambda_\alpha}} \right|_{\epsilon=0}, \quad \hat{p}_\alpha^R \equiv i \left. \frac{d}{d\epsilon} \hat{R}_{e^{i\epsilon\lambda_\alpha}} \right|_{\epsilon=0}. \quad (6.33)$$

Unless otherwise noted, λ_α generate the defining representation of G . With these we can implement the quadratic Casimir operator

$$\hat{p}^2 \equiv \sum_\alpha (\hat{p}_\alpha^L)^2 \equiv \sum_\alpha (\hat{p}_\alpha^R)^2. \quad (6.34)$$

We may now compute the commutator for \hat{u}_{jk}^l and \hat{p}_α^L . We find

$$\begin{aligned} \hat{p}_\alpha^L \hat{u}_{jk}^l &= i \int dg \left. \frac{d}{d\epsilon} t_{jk}^l(g) |e^{i\epsilon\lambda_\alpha} g\rangle \langle g| \right|_{\epsilon=0} \\ &= i \int dg \left. \frac{d}{d\epsilon} \sum_{j'} t_{jj'}^l(e^{-i\epsilon\lambda_\alpha}) t_{j'k}^l(g) |g\rangle \langle e^{-i\epsilon\lambda_\alpha} g| \right|_{\epsilon=0} \\ &= \sum_{j'} \left. \frac{d}{d\epsilon} t_{jj'}^l(e^{-i\epsilon\lambda_\alpha}) \right|_{\epsilon=0} \hat{u}_{j'k} + \hat{u}_{jk} \hat{p}_\alpha^L, \\ &= \sum_{j'} [\lambda_\alpha^l]_{jj'} \hat{u}_{j'k}^l + \hat{u}_{jk} \hat{p}_\alpha^L, \end{aligned} \quad (6.35)$$

where we have written out \hat{u}_{jk}^l in the position basis and used (6.33) for the first line. We then exploit the invariance of the Haar measure and apply the product rule. Rearranging, we have

$$[\hat{p}_\alpha^L, \hat{u}_{jk}^l] = \sum_{j'} [\lambda_\alpha^l]_{jj'} \hat{u}_{j'k}^l. \quad (6.36)$$

6.6 Operators in the momentum basis

We can also write the above operators in terms of the momentum basis (6.18). For $\widehat{p}_\alpha^L, \widehat{p}_\alpha^R$ and \widehat{p}^2 , this is relatively straightforward. For \widehat{p}_α^L we have

$$\begin{aligned}
{}_\nu \langle j'k' | \widehat{p}_\alpha^L | jk \rangle_l &= i\sqrt{d_l d_{l'}} \int dg dh \overline{t_{j'k'}^l(h)} t_{jk}^l(g) \frac{d}{d\epsilon} \langle h | e^{i\epsilon\lambda_\alpha} g \rangle \Big|_{\epsilon=0} \\
&= i\sqrt{d_l d_{l'}} \int dg \overline{t_{j'k'}^l(g)} \frac{d}{d\epsilon} t_{jk}^l(e^{-i\epsilon\lambda_\alpha} g) \Big|_{\epsilon=0} \\
&= i\sqrt{d_l d_{l'}} \int dg \overline{t_{j'k'}^l(g)} \sum_m \frac{d}{d\epsilon} t_{jm}^l(e^{-i\epsilon\lambda_\alpha}) t_{mk}^l(g) \Big|_{\epsilon=0} \\
&= i \delta_{ll'} \delta_{kk'} \frac{d}{d\epsilon} t_{jj'}^l(e^{-i\epsilon\lambda_\alpha}) \Big|_{\epsilon=0} \\
&= \delta_{ll'} \delta_{kk'} \left[\lambda_\alpha^l \right]_{jj'},
\end{aligned} \tag{6.37}$$

where we have exploited the invariance of the Haar measure. Similarly,

$${}_\nu \langle j'k' | \widehat{p}_\alpha^R | jk \rangle_l = -\delta_{ll'} \delta_{jj'} \left[\lambda_\alpha^l \right]_{k'k}. \tag{6.38}$$

In the abelian case of $G \cong U(1)$ we have the particularly simple form

$$\langle n | \widehat{p}^L | m \rangle = -\langle n | \widehat{p}^R | m \rangle = n \delta_{nm}. \tag{6.39}$$

Inserting the more general forms (6.37) and (6.38) into the definition of \widehat{p}^2 (6.34) yields

$${}_\nu \langle j'k' | \widehat{p}^2 | jk \rangle_l = \sum_\alpha \delta_{ll'} \delta_{kk'} \left[(\lambda_\alpha^l)^2 \right]_{jj'} = \sum_\alpha \delta_{ll'} \delta_{jj'} \left[(\lambda_\alpha^l)^2 \right]_{k'k}, \tag{6.40}$$

where we identify $\sum_\alpha (\lambda_\alpha^l)^2$ as the Casimir element of the Lie algebra, which is proportional to the identity for each irrep l . We find

$${}_\nu \langle j'k' | \widehat{p}^2 | jk \rangle_l = \delta_{ll'} \delta_{jj'} \delta_{kk'} l(l+1) \quad \text{for } G \cong SU(2), \tag{6.41}$$

$$\langle n | \widehat{p}^2 | m \rangle = \delta_{nm} n^2 \quad \text{for } G \cong U(1), \tag{6.42}$$

where the $SU(2)$ result comes from $\sum_\alpha (\lambda_\alpha^l)^2 = l(l+1)\mathbb{I}$. Similar calculations to that of (6.37) provide the matrix elements of \widehat{L} and \widehat{R} :

$$\begin{aligned}
{}_\nu \langle j'k' | \widehat{L}_g | jk \rangle_l &= {}_\nu \langle j'k' | \sqrt{d_l} \int dh t_{jk}^l(h) | gh \rangle \\
&= {}_\nu \langle j'k' | \sqrt{d_l} \int dh \sum_m t_{jm}^l(g^{-1}) t_{mk}^l(h) | h \rangle \\
&= {}_\nu \langle j'k' | \sum_m t_{jm}^l(g^{-1}) | mk \rangle_l \\
&= \delta_{ll'} \delta_{kk'} t_{jj'}^l(g^{-1}),
\end{aligned} \tag{6.43}$$

$${}_\nu \langle j'k' | \widehat{R}_g | jk \rangle_l = \delta_{ll'} \delta_{jj'} t_{k'k}^l(g). \tag{6.44}$$

From this it is clear that $[\widehat{p}^2, \widehat{L}_g] = [\widehat{p}^2, \widehat{R}_g] = 0$, since \widehat{L} and \widehat{R} are block-diagonal and \widehat{p}^2 is proportional to the identity in each of the l -blocks.

The position operator \widehat{u}_{jk}^l has a more complicated form in the momentum basis, as we should expect. Let us first handle the abelian case $G \cong U(1)$, where we have

$$\begin{aligned}\widehat{u}^k |n\rangle &= \widehat{u}^k \int dz z^n |z\rangle \\ &= \int dz z^n z^k |z\rangle \\ &= |n+k\rangle,\end{aligned}\tag{6.45}$$

where $z \in \mathbb{C}$, $|z|^2 = 1$ and dz is the Haar measure. Hence \widehat{u} and \widehat{u}^\dagger are ladder operators

$$\langle m | \widehat{u}^k | n \rangle = \delta_{n+k, m},\tag{6.46}$$

and \widehat{u}^k can be read as the k th power of \widehat{u} .

For the nonabelian group $SU(2)$ the position operator plays an analogous role, however the raising and lowering rules are more complicated, accounting for example for the higher dimensionality of the irreps. Proceeding the same way as for $U(1)$, we first examine

$$\widehat{u}_{mn}^s |jk\rangle_l = \sqrt{d_l} \int dg t_{jk}^l(g) t_{mn}^s(g) |g\rangle.\tag{6.47}$$

We note that the RHS has the form of a tensor product of two irreps $(V_l \otimes V_l^*) \otimes (V_s \otimes V_s^*)$ which, itself being a (reducible) representation of G , can always be decomposed into a direct sum of irreps $\bigoplus_{l'} (V_{l'} \otimes V_{l'}^*)$. The coefficients for this decomposition are known within physics as Clebsch-Gordan (CG) coefficients [174, 177], which we define (ignoring multiple occurrences of each irrep in a decomposition, which never happens for $SU(2)$) as

$$C_{l,j;s,n}^{l',j'} \equiv \nu \langle j' | (|j\rangle_l \otimes |n\rangle_s),\tag{6.48}$$

where $|j\rangle_l$ are the same basis elements for V_l used in Theorem 6.3.1 for the definition of t_{jk}^l . With the CG coefficients, we have

$$\begin{aligned}\widehat{u}_{mn}^s |jk\rangle_l &= \sqrt{d_l} \sum_{l',j'k'} (C_{l,j;s,n}^{l',j'})^* C_{l,k;s,m}^{l',k'} \int dg t_{j'k'}^{l'}(g) |g\rangle \\ &= \sum_{l',j'k'} \sqrt{\frac{d_l}{d_{l'}}} (C_{l,j;s,n}^{l',j'})^* C_{l,k;s,m}^{l',k'} |j'k'\rangle_{l'}.\end{aligned}\tag{6.49}$$

The CG coefficients, which can be assumed real without loss of generality, can be computed efficiently for $SU(N)$ [177]. For $SU(2)$, and the special case of $s = \frac{1}{2}$, which is the only case we later implement, $C_{l,j;1/2,n}^{l',j'}$ is non-zero only for $l' = l \pm 1/2$.

6.7 Hamiltonian lattice gauge theory

An elegant discretisation of Yang-Mills theory, with the key feature of maintaining gauge invariance on the lattice, was provided by Wilson in 1974 [178]. He imagined a lattice where the vertices represent points in spacetime, but it is equally possible to discretise only space, keeping time continuous. This was done by Kogut and Susskind [164], who developed a Hamiltonian, quantum formulation of lattice gauge theory. It is this latter approach that we follow here, explicitly breaking Lorentz-invariance in order to work directly with a quantum lattice system.

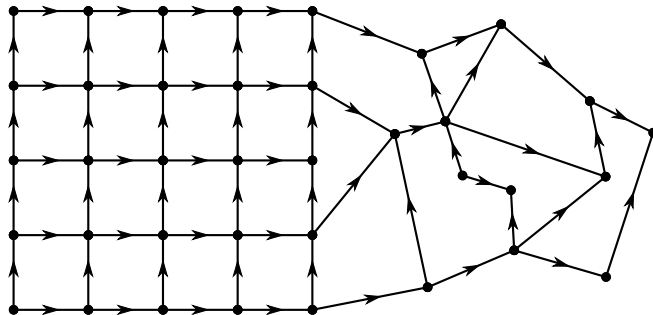


Figure 6.1: A directed graph. Lattice gauge theory is usually considered on regular lattices, such as the left part of this graph, but can be formulated on any directed graph, which we may imagine to be a particular discretisation of spacetime.

In general, we can imagine discretising space by embedding an arbitrary graph in it, with edges \mathcal{E} and vertices \mathcal{V} (see Figure 6.1). The gauge field degrees of freedom in lattice gauge theory, are assigned to the *edges* of the graph. This makes sense, because the spatial gauge connection $A_j(x)$ of the continuum theory, which takes values in the Lie algebra of the gauge group, assigns an element of the gauge group $U_\gamma \in G$ to any path γ in space via the *parallel transporter*

$$U_\gamma = \mathcal{P} \exp \left(ig_0 \int_{\gamma(x,y)} dx'_j A_j(x') \right), \quad (6.50)$$

where \mathcal{P} indicates path ordering of the matrices $A_j(x')$ in the expanded expression and $g_0 \in \mathbb{R}$ is a constant. Since the edges in the graph represent paths between the points in space corresponding to each vertex, (6.50) gives us an element of the gauge group $U_{\gamma(e)}$ for each edge $e \in \mathcal{E}$ in our graph. The direction of the edge determines the direction in which the path $\gamma(e)$ along it is traversed. Switching the direction of an edge is the same as inverting $U_{\gamma(e)}$.

A gauge transformation \mathcal{G} assigns an element $g \in G$ to each *point* in space. In the continuum, it acts on the gauge field as [81]

$$A_j(x) \mapsto g(x)^{-1} A_j(x) g(x) + \frac{i}{g_0} g(x)^{-1} \partial_j(x) g(x). \quad (6.51)$$

From (6.50), path ordering implies that $U_\gamma \mapsto g(\gamma_i)^{-1} U_\gamma g(\gamma_f)$, where γ_i and γ_f are the points at the start and end of the path. We can thus think of a gauge transformation

as assigning an element $g_v \in G$ to each *vertex* v of the graph. This element acts on the adjoining edge variables $U_{\gamma(e)}$ as $g_v^{-1}U_{\gamma(e)}$ if the e *begins* on v , and as $U_{\gamma(e)}g_v$ if e *ends* on v . We illustrate this in Figure 6.2.

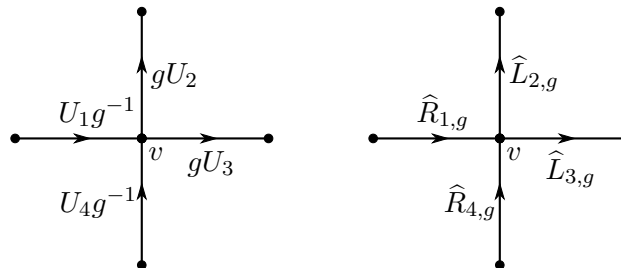


Figure 6.2: Illustration of a gauge transformation in lattice gauge theory. A gauge transformation assigns an element $g \in G$ to the vertex v , which acts on the adjoining edges 1...4 by multiplying from the left or right, depending on whether the edge is directed toward or away from the vertex. On the left we show the action in terms of classical variables, with the Hilbert space implementation on the right.

So far we have considered the gauge field in classical terms. We now quantise by assigning the Hilbert space $L^2(G)$ to each edge of the spatial graph, instead of single gauge group element, allowing superpositions of gauge field configurations. Kogut and Susskind determined an appropriate choice of Hamiltonian in [164]. Using the operators defined in Section 6.5, we define the Kogut-Susskind Hamiltonian as

$$H_{\text{KS}} = \frac{g^2}{2a} \sum_{e \in \mathcal{E}} \hat{p}_e^2 - \frac{2}{g^2 a} \sum_{p \in P} \text{Re}(\text{tr}(\hat{\mathbf{u}}_p)), \quad (6.52)$$

where g is the coupling strength parameter and a is the lattice spacing, which in general could be different for each edge in the graph. Note that, for a regular lattice, the lattice spacing appears as an overall factor on H and thus has no effect on the spectrum of the theory beyond scaling. In the sums, \mathcal{E} is the set of edges of the spatial lattice, or graph, and P is the set of *plaquettes*. Plaquettes are two-dimensional surfaces defined by the shortest closed paths, or loops, along edges. We choose P to be a set of non-overlapping, non-intersecting surfaces. On a 2D square lattice, for example, the plaquettes are the squares.

We define the plaquette position operator

$$\hat{\mathbf{u}}_p \equiv \dots \hat{\mathbf{u}}(\gamma_p^2) \hat{\mathbf{u}}(\gamma_p^1), \quad (6.53)$$

where γ_p is a directed path around plaquette p and γ_p^n is the n th edge along the path. We also use the abbreviation

$$\hat{\mathbf{u}}(\gamma_p^n) \equiv \hat{\mathbf{u}}_{\gamma_p^n}^{-\text{sign}(\gamma_p^n)}, \quad (6.54)$$

where $\text{sign}(\gamma^n)$ equals 1 if the path γ traverses its n th edge in the *same* direction as the edge itself, and -1 otherwise. Taking the trace of $\hat{\mathbf{u}}_p$, which is performed on the matrix indices (see (6.28)) so that the result is still an operator, completes a loop of position observables, called a Wilson loop, around the plaquette. Wilson loops have the property of being invariant under gauge transformations, as we explain in the following.

6.7.1 Gauge transformations

Gauge transformations are implemented on the full Hilbert space $\mathcal{H} = \bigotimes_{e \in E} L^2(G)$ using the left and right rotation operators \widehat{L} and \widehat{R} (defined in (6.25)) as illustrated on the right hand side of Figure 6.2. A general gauge transformation has the form

$$\mathcal{G}[g_v] : |\psi\rangle \mapsto \prod_{v \in \mathcal{V}} \left(\prod_{e \in \mathcal{E}_{v-}} \widehat{L}_{g_v;e} \right) \left(\prod_{f \in \mathcal{E}_{v+}} \widehat{R}_{g_v;f} \right) |\psi\rangle, \quad (6.55)$$

where the square brackets in $\mathcal{G}[g_v]$ indicate dependence on the set of gauge group elements $g_v \in G$ and $\mathcal{E}_{v-} \subset \mathcal{E}$ and $\mathcal{E}_{v+} \subset \mathcal{E}$ denote the subsets of edges that begin and end on vertex v , respectively. The invariance of a loop of position operators $\text{tr}(\widehat{\mathbf{u}}_\gamma)$ follows from (6.31). For example, using (6.31) in (6.53) we see that $\widehat{\mathbf{u}}_p$ only receives contributions under a gauge transformation from the $\widehat{\mathbf{u}}$ operators at the start and end of the loop and these contributions cancel under the trace:

$$\begin{aligned} \widehat{\mathbf{u}}_p &\mapsto t(g)\widehat{\mathbf{u}}_p t(g^{-1}) \\ \implies \text{tr}(\widehat{\mathbf{u}}_p) &\mapsto \text{tr}(\widehat{\mathbf{u}}_p). \end{aligned} \quad (6.56)$$

As well as Wilson loops, we also know that \widehat{p}^2 is gauge invariant since it commutes with all rotations, as shown in Section 6.6. We can thus confirm that the Hamiltonian (6.52) is invariant under gauge transformations \mathcal{G} , which is to say it commutes with the projector onto the gauge invariant subspace of physical states

$$\widehat{P}_{\text{phys}} = \int \left(\prod_{v \in \mathcal{V}} dg_v \right) \widehat{U}_{\mathcal{G}[g_v]}, \quad (6.57)$$

which applies all possible gauge transformations, where $\widehat{U}_{\mathcal{G}[g_v]}$ is the unitary implementation of the gauge transformation $\mathcal{G}[g_v]$. We can divide the full Hilbert space into a physical, gauge-invariant part and a nonphysical part as

$$\mathcal{H} = \mathcal{H}_{\text{phys}} \oplus \mathcal{H}_{\text{nonphys}}, \quad (6.58)$$

where $\widehat{P}_{\text{phys}}$ projects onto $\mathcal{H}_{\text{phys}}$.

It is interesting to realise that the physical subspace $\mathcal{H}_{\text{phys}}$, in contrast to \mathcal{H} , does not have an obvious tensor product decomposition in terms of the edges of the graph. This is ultimately due to the nature of local gauge transformations, which affect all edges joined to a particular vertex. The transformations corresponding to different vertices overlap in terms of the edges they affect, with the result that applying $\widehat{P}_{\text{phys}}$ to some state generally creates entanglement between the edges. Even if the original state $|\psi\rangle$ was a product state under the decomposition $\mathcal{H} = \bigotimes_{e \in \mathcal{E}} L^2(G)$, the state $\widehat{P}_{\text{phys}}|\psi\rangle$ is not in general.

6.7.2 Graph manipulation

The Hilbert space $\mathcal{H} = \bigotimes_{e \in \mathcal{E}} L^2(G)$ in which the Hamiltonian (6.52) acts is clearly dependent only on the number of edges in the graph on which the lattice gauge theory is

defined. $\mathcal{H}_{\text{phys}}$, on the other hand, is determined by the gauge transformations, which in turn depend on the *connectivity* of the graph, since they act on edges according to which vertex they are connected to. Indeed, specifying the set of possible gauge transformations on \mathcal{H} is *equivalent* to defining the connectivity of the edges in the graph.

In this section we consider unitary transformations

$$\widehat{V} : \mathcal{H} \rightarrow \mathcal{H} \quad (6.59)$$

that *modify* the set of gauge transformations, thus changing the connectivity of the graph and altering the physical subspace

$$\widehat{V} : \mathcal{H}_{\text{phys}} \rightarrow \mathcal{H}'_{\text{phys}}. \quad (6.60)$$

Such transformations can be used to relate the physics of differently connected graphs. In Chapter 7, we use them to relate numerical results for a particularly simple graph, for which the Hamiltonian is easy to implement, to a more complicated graph.

In the following we show how to construct \widehat{V} from simple building blocks, exploring the transformation of the operators used in the Hamiltonian (6.52) in order to determine how the physics of one physical subspace translates into another.

Parallel transport and controlled rotations

Graph-manipulating unitaries can be constructed from the quantum analogue of *parallel transport* operations. Parallel transport specifies how to compare objects, such as values of a matter field, at distant points in the presence of a connection such as the gauge connection [167, 179]. To do this, one must account for the local gauge choices.

The classical parallel transporter in a continuum gauge theory is given by (6.50), which Wilson used as the basis for his gauge-invariant discretisation. To compare objects at distant vertices on a graph, we can build a parallel transporter U_γ for a connecting path γ using the parallel transporters $U_{\gamma(e)}$ of the edges along the path:

$$U_\gamma = \dots U_{\gamma^2}^{-\text{sign}(\gamma^2)} U_{\gamma^1}^{-\text{sign}(\gamma^1)}, \quad (6.61)$$

where γ^n refers to the n th edge in the path and the sign function is defined as for (6.54). U_γ is the gauge group element representing the transformation needed to compare an object at the beginning of γ with another object at the end.

In the quantised Hamiltonian theory (6.52), edges can be in superpositions of group elements and there can be entanglement between different edges. Performing parallel transport in the quantum setting may be viewed as integrating over the weighted classical configurations in the quantum wavefunction, performing classical parallel transport for each of them. We can implement this using *controlled* rotations

$$\widehat{C}U_{c,t} = \int dg |g\rangle\langle g|_c \otimes \widehat{U}_{g,t}, \quad (6.62)$$

where $\widehat{U}_{t,g}$ is a representation on a *target* Hilbert space of a rotation by the element $g \in G$. If the target system lives in $L^2(G)$, we may use $\widehat{L}_{g;t}$ or $\widehat{R}_{g;t}$. Which rotation to perform

is “chosen” by the *control* system c , which is always an edge of the graph in the case of parallel transport. Chaining these together along a path we can build up a quantum parallel transporter, for example

$$\widehat{CL}_{\gamma,t} = \prod_n \widehat{CL}_{\gamma^n,t}, \quad (6.63)$$

with

$$\begin{aligned} \widehat{CL}_{c,t} &= \int dg |g\rangle\langle g|_c \otimes \widehat{L}_{g;t} \quad \text{and} \\ \widehat{CR}_{c,t} &= \int dg |g\rangle\langle g|_c \otimes \widehat{R}_{g;t}. \end{aligned} \quad (6.64)$$

We began with the claim that these operations can be used to manipulate the connectivity of the graph on which the lattice gauge theory lives. This is the case if we apply quantum parallel transport operations with an *edge of the graph* as the target system, which serves to transport the edge, or at least one end of it, around the graph!

Quantum parallel transport of edges

That controlled rotations can be used to move edges around the graph can be seen by examining their action on gauge transformations. First, we derive the action of controlled rotations on the individual rotation operators \widehat{L} and \widehat{R} that make up the gauge transformations. We find for \widehat{CL} and \widehat{L}

$$\begin{aligned} \widehat{CL}(\widehat{L}_h \otimes \widehat{\mathbb{I}}) &= \int dg |g\rangle\langle h^{-1}g| \otimes \widehat{L}_g \\ &= \int dg |hg\rangle\langle g| \otimes \widehat{L}_{hg} \\ &= (\widehat{L}_h \otimes \widehat{L}_h)\widehat{CL}, \end{aligned} \quad (6.65)$$

where we have simply used the invariance of the Haar measure. Similarly

$$(\widehat{R}_h \otimes \widehat{\mathbb{I}})\widehat{CL} = \widehat{CL}(\widehat{R}_h \otimes \widehat{L}_h), \quad (6.66)$$

and, since $[L_g, R_h] = 0$,

$$\widehat{CL}(\widehat{\mathbb{I}} \otimes \widehat{R}_h) = (\widehat{\mathbb{I}} \otimes \widehat{R}_h)\widehat{CL}. \quad (6.67)$$

Results for \widehat{CR} are similarly straightforward to derive.

We can already use these results to manipulate a simple section of a graph consisting of two vertices joined by two edges:



An arbitrary gauge transformation has the form

$$\widehat{U}_{\mathcal{G}(g_v,g_w)} = \widehat{L}_{g_v;e} \widehat{R}_{g_w;e} \otimes \widehat{L}_{g_v;f} \widehat{R}_{g_w;f}, \quad (6.69)$$

with group elements g_v and g_w acting at vertices v and w respectively. We now apply $\widehat{CL}_{f,e}$, where f is the control system and e the target. We find, using (6.65), (6.66) and (6.67), that the gauge transformation transforms as

$$\widehat{CL}_{f,e}^\dagger \widehat{U}_{\mathcal{G}(g_v, g_w)} \widehat{CL}_{f,e} = \widehat{L}_{g_w;e} \widehat{R}_{g_w;e} \otimes \widehat{L}_{g_v;f} \widehat{R}_{g_w;f}, \quad (6.70)$$

which is the gauge transformation we would expect for the graph



which results from transporting the *beginning* of edge e along edge f , as indicated by the orange dotted arrow. If we wish to transport the *end* of edge e instead, we need only replace \widehat{CL} by \widehat{CR} . We see that, as for the gauge transformations, we use \widehat{L} to address the beginning of an edge and \widehat{R} to address the end.

It should be plain that we can build up unitary operators \widehat{V} that perform more sophisticated graph manipulations using the same controlled rotations used here. We can indeed use them to change the connectivity of graphs, thus changing the physical, gauge-invariant subspace. However, it is also clear that we cannot change the number of loops in the graph. This is clear in the above example: Although we can move the loop around, there is no operation in our repertoire that can open up the single-edge loop remaining, since we can only parallel transport ends of edges along *other* edges.

Dangling edges

Another observation we can make from the graph manipulation operations seen so far is that we cannot disconnect edges from a vertex to create a new, disconnected sub-graph. This is because we can only move the ends of edges along other edges. That is not, however, the whole story. Let us consider a graph with a “dangling” edge e



in which we only label the vertices v and w shared by e . The vertex w is not shared by any other edge in the graph. We now consider the effect of gauge transformations acting at w . Part of the projector onto the physical subspace of this graph is given by

$$\widehat{P}_{\text{phys},w} = \int dg R_{e,g}, \quad (6.73)$$

where, for any gauge group, we find

$$\widehat{P}_{\text{phys},w} = \int dg dh |g\rangle\langle h| = |00\rangle_0\langle 00|_0, \quad (6.74)$$

where $|00\rangle_0$, the equal superposition of all group elements, is the “zero kinetic energy” state in the Fourier basis: $\widehat{p}^2|00\rangle_0 = 0$. We must conclude that any dangling edge must, for states in the physical subspace, be uncorrelated from the rest of the system and occupy the state $|00\rangle_0$ (or simply $|0\rangle$ in the $U(1)$ notation).

These considerations imply that there is a set of equivalent graphs describing the same physical subspace: Since any dangling edge, having one unshared vertex w , must be in the state $|00\rangle_0$, and since this state is invariant under all rotations, \widehat{L} or \widehat{R} , the position of the edge, and the connectivity of the remaining vertex v has no effect on the physical subspace — the edge can even be completely disconnected from the rest of the graph, with both its vertices unshared:

$$\text{Diagram (6.75)} \quad (6.75)$$

Note that a dangling edge not only has zero kinetic energy, it also cannot participate in a plaquette in the Hamiltonian (6.52), since it can only be part of a closed path in a trivial sense: A closed path that traverses a dangling leg must immediately double back on itself, leading to $\widehat{\mathbf{u}}_e \widehat{\mathbf{u}}_e^\dagger$ in the plaquette term, which by (6.32) is equal to the identity. As such, dangling legs are not only fixed in one state, but are completely invisible to the Kogut-Susskind Hamiltonian. We can thus understand the freedom to move dangling legs around the graph as being due to their unphysical nature: Moving them does not change the physical subspace because they are completely nonphysical anyway.

Transformation of Hamiltonian operators

As well as determining the set of gauge transformations, the graph also determines how we may define the Kogut-Susskind Hamiltonian (6.52) for the system, since it puts constraints on the possible plaquettes. It would be extremely convenient if the graph manipulation maps \widehat{V} we can construct between physical subspaces of different graphs would also transform the Hamiltonian of one system into a natural Hamiltonian for the other, where by “natural” we mean that the plaquette operators are again mapped to plaquette operators on the fundamental plaquettes and that the \widehat{p}^2 operators acting on each edge remain in place. Unfortunately, only the former is generally the case.

To find the action of graph manipulation on plaquettes, we first examine the action of controlled rotations on the position operator, finding

$$\widehat{CL}(\widehat{u}_{jk}^l \otimes \widehat{\mathbb{I}}) = \int dg |g\rangle\langle g| t_{jk}^l(g) \otimes \widehat{L}_g = (\widehat{u}_{jk}^l \otimes \widehat{\mathbb{I}})\widehat{CL}, \quad \text{and} \quad (6.76)$$

$$\begin{aligned} \widehat{CL}^\dagger(\widehat{\mathbb{I}} \otimes \widehat{u}_{jk}^l) &= \int dg |g\rangle\langle g| \otimes \sum_{j'} t_{jj'}^l(g) \widehat{u}_{j'k}^l \widehat{L}_g^\dagger \\ &= \sum_{j'} (\widehat{u}_{jj'}^l \otimes \widehat{u}_{j'k}^l) \widehat{CL}^\dagger, \end{aligned} \quad (6.77)$$

where on the second line we use (6.31). Analogous results exist for \widehat{CR} . We may now again

consider the example of moving between the graphs

$$(6.78)$$

this time transforming the plaquette operator $\text{tr}(\hat{\mathbf{u}}_e \hat{\mathbf{u}}_f^\dagger) = \sum_{jk} \hat{u}_{jk;f}^\dagger \otimes \hat{u}_{jk;e}$, we find

$$\widehat{CL}_{f,e}^\dagger \text{tr}(\hat{\mathbf{u}}_e \hat{\mathbf{u}}_f^\dagger) \widehat{CL}_{f,e} = \sum_{jj'k} (\hat{u}_{jk}^\dagger \otimes \hat{\mathbb{I}}) (\hat{u}_{jj'} \otimes \hat{u}_{j'k}) = \sum_k (\hat{\mathbb{I}} \otimes \hat{u}_{kk}) = \text{tr}(\hat{\mathbf{u}}_e), \quad (6.79)$$

where we have used (6.32): $\sum_j \hat{u}_{jk}^\dagger \hat{u}_{jj'} = [\hat{\mathbf{u}}^\dagger \hat{\mathbf{u}}]_{kj'} = \hat{\mathbb{I}} \delta_{kj'}$. The transformed operator is indeed the plaquette of the e loop in the new graph.

The effect of \widehat{CL} on the \hat{p}_α^L operator is

$$\widehat{CL}(\hat{\mathbb{I}} \otimes \hat{p}_\alpha^L) = (\hat{\mathbb{I}} \otimes \hat{p}_\alpha^L) \widehat{CL} \quad \text{and} \quad (6.80)$$

$$\begin{aligned} \widehat{CL}(\hat{p}_\alpha^L \otimes \hat{\mathbb{I}}) &= i \int dg |g\rangle \langle g| \frac{d}{d\epsilon} L_{e^{i\epsilon\lambda_\alpha}}|_{\epsilon=0} \otimes L_g \\ &= i \frac{d}{d\epsilon} \int dg |e^{i\epsilon\lambda_\alpha} g\rangle \langle g| \otimes L_{e^{i\epsilon\lambda_\alpha} g} \Big|_{\epsilon=0} \\ &= i \frac{d}{d\epsilon} \int dg L_{e^{i\epsilon\lambda_\alpha}} |g\rangle \langle g| \otimes L_{e^{i\epsilon\lambda_\alpha}} L_g \Big|_{\epsilon=0} \\ &= (\hat{p}_\alpha^L \otimes \hat{\mathbb{I}} + \hat{\mathbb{I}} \otimes \hat{p}_\alpha^L) \widehat{CL}, \end{aligned} \quad (6.81)$$

where we have utilised the Haar measure as well as the product rule. Similarly

$$\widehat{CL}^\dagger(\hat{p}_\alpha^R \otimes \hat{\mathbb{I}}) = (\hat{p}_\alpha^R \otimes \hat{\mathbb{I}} + \hat{\mathbb{I}} \otimes \hat{p}_\alpha^L) \widehat{CL}^\dagger. \quad (6.82)$$

Using the definition of \hat{p}^2 from (6.34) we then find

$$\widehat{CL}(\hat{\mathbb{I}} \otimes \hat{p}^2) = (\hat{\mathbb{I}} \otimes \hat{p}^2) \widehat{CL}, \quad (6.83)$$

$$\widehat{CL}(\hat{p}^2 \otimes \hat{\mathbb{I}}) = (\hat{p}^2 \otimes \hat{\mathbb{I}} + \hat{\mathbb{I}} \otimes \hat{p}^2 + 2 \sum_\alpha \hat{p}_\alpha^L \otimes \hat{p}_\alpha^L) \widehat{CL} \quad \text{and} \quad (6.84)$$

$$\widehat{CL}^\dagger(\hat{p}^2 \otimes \hat{\mathbb{I}}) = (\hat{p}^2 \otimes \hat{\mathbb{I}} + \hat{\mathbb{I}} \otimes \hat{p}^2 + 2 \sum_\alpha \hat{p}_\alpha^L \otimes \hat{p}_\alpha^R) \widehat{CL}^\dagger, \quad (6.85)$$

where we use (6.82) for the last line. We see that \hat{p}^2 transforms trivially only if it acts on the target system of the controlled rotation. Otherwise additional coupling terms are introduced. This also applies to \widehat{CR} for exactly the same reasons.

The \hat{p}^2 terms on the edges in the above graph manipulation example transform as

$$\widehat{CL}_{f,e}^\dagger (\hat{p}_f^2 + \hat{p}_e^2) \widehat{CL}_{f,e} = \hat{p}_e^2 + \hat{p}_f^2 + \hat{p}_e^2 + 2 \sum_\alpha \hat{p}_{\alpha;f}^L \hat{p}_{\alpha;e}^R, \quad (6.86)$$

where we have omitted the explicit tensor products. Note that, since the \hat{p}^2 terms are individually gauge invariant, and because graph manipulation maps the physical, gauge-invariant subspace to a new gauge-invariant subspace, the term $2 \sum_\alpha \hat{p}_{\alpha;f}^L \hat{p}_{\alpha;e}^R$ must also be gauge invariant, and thus has a purely physical effect.

Thus it is not generally true that the kinetic \hat{p}^2 terms of the Hamiltonian (6.52) are left in place by a unitary mapping to a different graph.

Applications

In [165], graph manipulation operations are used to develop an *interpolation* operation for lattice gauge theories that adds new edges to the graph, creating a finer discretisation of space by interpolating the gauge field to build the new plaquettes. New edges are added by embedding the Hilbert space into a larger one consisting of more edges, putting them in gauge-invariant states, such as the “dangling edge” state $|00\rangle_0$ (see above), that allow them to be added to the existing graph.

We use graph manipulation in Chapter 7 when considering the (1+1)D quantum rotor model, which is equivalent to the Kogut-Susskind Hamiltonian (6.52) on a simple kind of graph, which we then relate to a more complicated one using graph manipulation operations.

6.7.3 Continuum limits and renormalisation

Since lattice gauge theory is intended as a discretisation of a continuum field theory, it had better be possible to take a continuum limit. However, we have seen that the lattice spacing parameter a , in the case of a regular lattice graph, goes into the Hamiltonian (6.52) as an overall factor, making the limit $a \rightarrow 0$ taken by adjusting only a trivial. In fact, we must generally adjust the other parameters of a discretised theory together with the lattice spacing in order to obtain the correct continuum limit. For more details, see [81]. The latter part of this discussion is also based on [180].

The operation of obtaining from a given theory, say a quantum field theory, an effective theory that is accurate only down to a certain minimum length scale, is known as *renormalisation*. In our case, the lattice spacing a represents the choice of minimum length scale, since the lattice theory can only hope to approximate the continuum field theory at lengths much greater than a . Equivalently, one can think of the lattice discretisation as implementing a momentum cutoff, since spatial Fourier modes can only be reproduced up to a maximum frequency proportional to $1/a$.

We wish to find a path of lattice theories that take us to the correct continuum theory so that we may compute limits of physical quantities. This requires each choice of lattice theory to represent a renormalised version of the continuum theory and, furthermore, it requires us to follow a *path* of lattice theories known as a renormalisation trajectory, or *flow*. If we limit our choice of lattice theory to the Kogut-Susskind Hamiltonian (6.52) on some regular lattice with lattice spacing a , our path is in the parameter space (a, g) . However, intriguingly, in the case where the Kogut-Susskind Hamiltonian has a mass gap, the lattice spacing a is *determined* by the choice of g , so that we need only adjust g to some value g_c corresponding to the continuum limit! In fact, this is generally the case for pure Yang-Mills theory (without matter) with a cutoff [45].

That g determines a for a theory with a mass gap can be seen by considering a natural length scale or, equivalently, an energy scale in the continuum theory. In a massive continuum theory the mass gap ΔE_c itself provides such an energy scale. In the lattice discretisation (6.52) the mass gap ΔE is proportional to $1/a$, so that we may write

$$\Delta E = \frac{1}{a} F(g), \tag{6.87}$$

which defines $F(g)$ to be the mass gap in “lattice energy units” $1/a$. If we want to match up the lattice and continuum theories, we need $\Delta E(a, g) = \Delta E_c$, where ΔE_c is a constant. For a path in (a, g) we thus require the mass gap, in physical units, to remain fixed as we change the lattice spacing

$$\frac{d}{da}(\Delta E) = 0, \quad (6.88)$$

which requires that g be dependent on a . Indeed, if we can determine $F(g)$ (for example numerically) we may find a by rearranging (6.87)

$$a = \frac{1}{\Delta E_c} F(g), \quad (6.89)$$

which implies that a continuum limit involves the mass gap in lattice units $F(g)$ vanishing. In other words, a continuum limit can only be found at a continuous phase transition of the lattice model (see Chapter 2). This means taking a continuum limit is as straightforward as adjusting g to some g_c with $F(g \rightarrow g_c) \rightarrow 0$. If (6.52) has multiple such limits, we can choose g_c to pick out the desired continuum theory.

We can also determine g as a function of the renormalisation length scale a . In this context, the flow of g with a is captured by the “beta function”

$$\beta(g) = -a \frac{dg}{da}, \quad (6.90)$$

where the minus sign is added to match the convention of defining the beta function as a derivative with respect to an *energy* scale, such as a mass, rather than a length scale, which has units of inverse energy. In this convention, a positive beta function means the coupling of the renormalised theory *grows* as we increase the energy scale at which the theory is a good approximation. A negative beta function means the coupling of the renormalised theory must *decrease* with the renormalisation energy scale or, equivalently, it must increase with the renormalisation length scale a .

The beta function thus indicates how the effective coupling changes at different length or energy scales. As an example, it is possible to compute the beta function of certain quantum field theories in certain regimes perturbatively [81]. It is found that QED has a positive beta function, meaning that the effective coupling becomes increasingly strong as energy increases. QCD, on the other hand, has a negative beta function at high energies, meaning that the effective coupling becomes weaker with increasing energy. This is consistent with observed “asymptotic freedom” of quarks — the phenomenon of quarks behaving as weakly-interacting particles at large scattering energies, despite them forming strongly coupled bound states (hadrons) at low energies.

The zeros of the beta function are also interesting. Substituting (6.87) into (6.88) gives us

$$\beta(g) = \frac{F(g)}{F'(g)}, \quad (6.91)$$

which implies that $\beta(g)$ goes to zero at a second order phase transition of the lattice model. This is because $F(g)$ obeys a power law in the vicinity of such a transition (see Chapter 2)

$$F(g) \stackrel{g \rightarrow g_c}{\approx} b(g_c - g)^\nu, \quad (6.92)$$

which gives us

$$\beta(g) \stackrel{g \rightarrow g_c}{\approx} \frac{g - g_c}{\nu}, \quad (6.93)$$

which goes to zero at $g = g_c$. $\beta(g_c) = 0$ implies we have reached a fixed point of the renormalisation flow, since changing the scale a no longer requires a change in g . This is consistent with the scale invariance of the lattice system at a critical point g_c .

Chapter 7

Lattice gauge theory on an earring and the $O(N)$ rotor model

7.1 Introduction

In this chapter we present a numerical study using matrix product states (MPS — see Chapter 1) of the $O(2)$ and $O(4)$ quantum rotor models in one spatial dimension, which are equivalent in formulation to Hamiltonian lattice gauge theory on a “Hawaiian earring” graph for the gauge groups $U(1) \cong O(2)$ and $SU(2)$ (owing to $SU(2) \times SU(2)$ being the double cover of $SO(4)$ — see Section 6.3). The only difference is that some states (but not the ground state) of the rotor model are excluded from the gauge theory in the nonabelian $SU(2)$ case as they violate the gauge symmetry, which is a *global* symmetry for the earring graph. The nonabelian $O(4)$ rotor has a second connection to lattice gauge theory, in that its phase diagram is similar to what is expected from (3+1)D nonabelian lattice gauge theory: They both have a mass gap for all nonzero values of the coupling g . In the gauge theory, this is consistent with the phenomenon of *confinement* [170].

We view this study as a proof of principle with regard to the more general application of tensor network state (TNS) methods to nonabelian gauge theories. As such it builds on previous work on using TNS to treat quantum field theories, including the use of DMRG and MPS to obtain ground states and simulate real-time evolution of ϕ^4 theory [19, 21], the Schwinger model [18, 22–26], $SU(2)$ lattice gauge theory on a line with matter [27], as well as quasi-one-dimensional abelian gauge theories [20]. There have also been general proposals for treating lattice gauge theories with continuous gauge groups using higher-dimensional TNS [165, 181, 182]. Our work is novel in that it numerically treats a nontrivial nonabelian gauge theory without matter, albeit with global instead of local gauge symmetry. It also constitutes the first study (to the author’s knowledge) of the full rotor model (rather than a model whose low-energy physics is approximately equivalent) using MPS or DMRG techniques. Previous numerical studies have used Monte Carlo simulation of the classical two-dimensional model, for example [183–187]. Since there are some exact results for the continuum limit of these models [188], we are also able to check our results to a good level of satisfaction.

In the following, we first define the model as a lattice gauge theory on the Hawaiian earring graph before showing its equivalence to the (1+1)D quantum rotor model. We also use the graph manipulation techniques of Section 6.7.2 to show how the model is related to lattice gauge theory on a cylinder, which has local gauge symmetry in the nonabelian case. We then summarise some known results for the rotor, both numerical and analytical, before presenting our MPS study. Using techniques described in Section 1.3, we obtain approximate ground states using MPS, as well as approximate excited states, allowing us to compute the mass gap and, in turn, the beta function. We compare these with existing strong and weak coupling results. Additionally, we identify low-lying excitations of the $O(4)$ model that are also physical states of the $SU(2)$ Hawaiian earring model (those which are invariant under gauge transformations).

This chapter represents independent work of the author and was published in [189].

7.2 Theory

7.2.1 Lattice gauge theory on a Hawaiian earring

The Kogut-Susskind Hamiltonian (see Section 6.7) on the “Hawaiian earring” graph is given by

$$H_{\text{KS}}(g) = \frac{\sqrt{\eta}g^2}{2a} \sum_{k=1}^N \hat{p}_k^2 - \frac{2\sqrt{\eta}}{g^2a} \sum_{k=1}^{N-1} \text{Re}(\text{tr}(\hat{\mathbf{u}}_k \hat{\mathbf{u}}_{k+1}^\dagger)), \quad (7.1)$$

where g is the coupling, a the lattice spacing, and η an anisotropy parameter required to ensure the renormalised theory is Lorentz-invariant in the continuum limit [190]. The Hilbert space, determined by the graph shown in Figure 7.1, and the operators used are as defined in Chapter 6. Since the model is effectively one-dimensional, we refer to edges by number $k = 1 \dots N$. The \hat{p}^2 term is the gauge group “kinetic energy” in $L^2(G)$ on a single edge, while the plaquette term involving $\hat{\mathbf{u}}$ measures the potential energy.

The gauge transformations (see Section 6.7.1) on the earring graph, which has only one vertex, act globally on the edges as $\hat{L}_g \hat{R}_g$ for $g \in G$. The physical Hilbert space $\mathcal{H}_{\text{phys}}$ thus corresponds to the image of the projector

$$\hat{P}_{\text{phys}} \equiv \int dg \prod_{k=1}^N \hat{L}_{g;k} \hat{R}_{g;k}, \quad (7.2)$$

in which the integral is over all gauge transformations. For definitions of the operators used, see Section 6.5. In the case of an abelian gauge group such as $U(1)$, where $\hat{R}_g = \hat{L}_g^\dagger$, the projector is trivial and $\mathcal{H}_{\text{phys}} = \mathcal{H}$. For nonabelian groups the gauge symmetric space is smaller than \mathcal{H} .

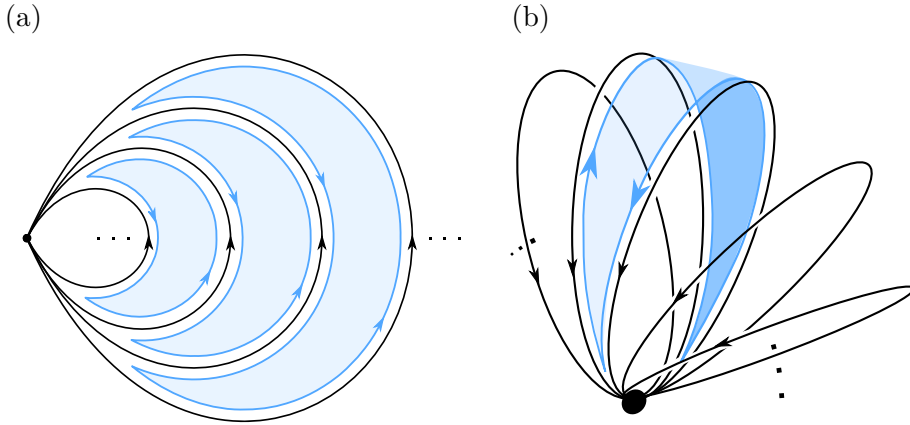


Figure 7.1: Illustration of lattice gauge theory (a) on a “Hawaiian earring” and (b) the same theory visualised differently as living on the surface of a 3D object. The Hamiltonian is the Kogut-Susskind [164] formulation of lattice gauge theory for a gauge group G — example plaquette operators are shown in blue. The Hilbert space \mathcal{H} (including nonphysical states) is made up of systems living on the (black) edges $\mathcal{H}_{\text{edge}} = L^2(G)$. For the gauge groups $G = U(1)$ and $G = SU(2)$ this model is equivalent to the (1+1)-dimensional quantum rotor model [76] for the rotation groups $O(2)$ and $O(4)$, respectively.

7.2.2 Connection to the cylinder

Hamiltonian Yang-Mills theory on a simple cylinder graph, which is illustrated in Figure 7.2 has the Kogut-Susskind Hamiltonian

$$H_{\text{KS, cyl}}(g) = \frac{\sqrt{\eta}g^2}{2a} \sum_{k=1}^N \hat{p}_k^2 - \frac{2\sqrt{\eta}}{g^2a} \sum_{k=1}^{N-1} \text{Re}(\text{tr}(\hat{\mathbf{u}}_k \hat{\mathbf{u}}_{k>} \hat{\mathbf{u}}_{k+1}^\dagger \hat{\mathbf{u}}_{k>}^\dagger)), \quad (7.3)$$

where k counts only the loops in the cylinder and $k>$ refers to the connecting edge between loops k and $k+1$. The plaquette operator is also illustrated in Figure 7.2.

Abelian case

The $U(1)$ Hawaiian earring model (7.1) is equivalent to the $U(1)$ cylinder model (7.3). To see this, we must examine the physical states of the cylinder model, which are those invariant under its gauge transformations (see Section 6.7.1).

The gauge transformations of the $U(1)$ cylinder act trivially on the loops k for an abelian group since $\hat{L}_x \hat{R}_x = \mathbb{I}$. However, they act nontrivially on the edges $k>$ joining the loops. We have

$$\hat{P}_{\text{phys, cyl}} \equiv \prod_{k=1}^N \int dg_k (\hat{L}_{g_k;k} \hat{R}_{g_k;k} \hat{L}_{g_k;(k-1)>} \hat{R}_{g_k;k>}), \quad (7.4)$$

where for $G = U(1)$ the term in brackets is trivial as in the earring case (7.2), and we define $\hat{L}_{g_1;0>} \equiv 1$ and $\hat{R}_{g_N;N>} \equiv 1$ to account for the lack of joining edges to the left of loop 1 and the right of loop N . Since the gauge transformations define the connectivity

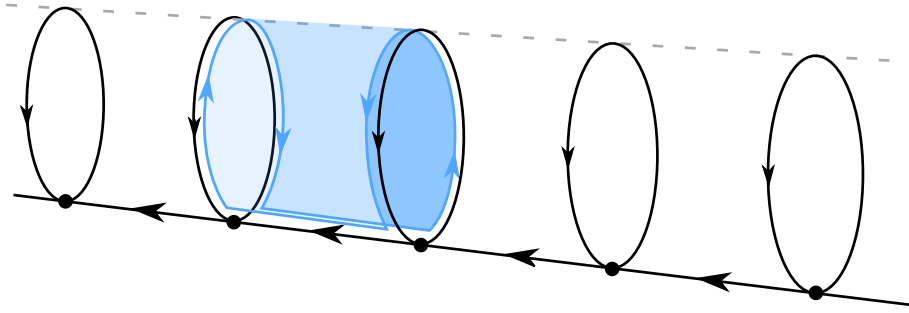


Figure 7.2: Lattice gauge theory on a simple cylinder graph. A plaquette operator is illustrated in blue. The Hilbert space is associated with the graph exactly as in Figure 7.1. As explained in Section 6.7.1, the graph defines the action of gauge transformations, since these act on the edges according to which vertices each edge is connected to.

of the graph (see Section 6.7.2), this means the $U(1)$ cylinder is equivalent to the earring graph, in which the loops are also unaffected by gauge transformations, with the addition of an extra component: A line consisting of all the joining edges $k_{>}$, disconnected from the earring. This is consistent with the Hamiltonian because the connecting edges drop out of the plaquette terms, which for $U(1)$ have the form $\text{Re}(\hat{u}_k \hat{u}_{k>} \hat{u}_{k+1}^\dagger \hat{u}_{k>}^\dagger)$. Since the \hat{u} commute and $\hat{u}_{k>} \hat{u}_{k>}^\dagger = \mathbb{I}$, only the loop edges remain.

We now consider how gauge transformations restrict physical states on the disconnected $k_{>}$ line. For open boundary conditions, gauge transformations can rotate the first or last edge in the line independently of the rest of the system. The corresponding terms in (7.4), neglecting the trivial loop terms, are

$$\hat{P}_{\text{phys, cyl},1} = \int dg_1 R_{g_1;1_{>}} \quad \text{and} \quad \hat{P}_{\text{phys, cyl},N} = \int dg_N L_{g_N;(N-1)_{>}}, \quad (7.5)$$

both of which, as we know from (6.74), project the edge they act on onto the equal superposition of all gauge group positions, otherwise known as the state of zero kinetic energy. For $U(1)$ the edges $1_{>}$ and $(N-1)_{>}$ are thus in the state $|0\rangle \equiv \int dg |g\rangle$ for all physical states, and are therefore decoupled from the rest of the system:

$$|\psi\rangle_{U(1),\text{cyl,phys}} = |0\rangle_{1_{>}} \otimes |0\rangle_{(N-1)_{>}} \otimes |\psi\rangle_{\text{rest}}. \quad (7.6)$$

They also contribute zero energy, since $\hat{p}^2|0\rangle = 0$ and we may therefore remove them from the graph, leaving a shorter line beginning with edge $2_{>}$ and ending with $(N-1)_{>}$. The same arguments now apply to these new beginning and end edges so that, by induction, we find physical states must be of the form

$$|\psi\rangle_{U(1),\text{cyl,phys}} = \left(\bigotimes_k |0\rangle_{k_{>}} \right) \otimes |\psi\rangle_{\text{loops}}, \quad (7.7)$$

making the disconnected line entirely nonphysical. The remaining physical theory is exactly that of $U(1)$ gauge theory on the Hawaiian earring graph.

Note again that the above assumes open boundary conditions, which we restrict to for the remainder of this chapter. In the case of periodic boundary conditions $k_1 \equiv k_{N+1}$, the $k_>$ edges still form a disconnected part of the graph and are thus decoupled from the loops. However, since they themselves then form a loop consisting of many edges, there are no longer any dangling edges that must be in the $|0\rangle$ state and they can have nontrivial physics. In fact, such a many-edge loop can be transformed, using the graph-manipulation moves of Section 6.7.2, into a single-edge loop plus a dangling line, whose edges must again occupy the $|0\rangle$ state. Any additional multi-edge terms involving \hat{p}^L and \hat{p}^R added by the graph manipulation are therefore trivial as they annihilate all physical states. The single loop takes part in no plaquettes in the Hamiltonian, and thus occupies a kinetic energy eigenstate $|n\rangle$ in all eigenstates of the Hamiltonian.

Nonabelian case

The above reasoning relating the cylinder to the earring does *not* go through for a nonabelian gauge group. Although in this case dangling edges must also be decoupled in physical states as described in Section 6.7.2, the nonabelian cylinder does not provide us with any dangling edges, since gauge transformations on loops do not act trivially and the connecting edges do not drop out of plaquettes.

Instead we can build a unitary graph-manipulation map \hat{V} that takes us from the physical Hilbert space of the earring to that of the cylinder. The first step is to enlarge the Hilbert space of the earring by adding dangling edges that will become the connecting edges $k_>$ of the cylinder. As shown in Section 6.7.2, we can always add dangling edges without altering the space of physical states, since they are forced to be in the zero-kinetic-energy state $|00\rangle_0$ (where we now use the nonabelian notation of Section 6.4). We modify the earring Hamiltonian (7.1) to act on this larger Hilbert space by adding \hat{p}^2 terms for the new edges that annihilate the physical states

$$H_{\text{KS} + \text{dangling}} \equiv H_{\text{KS}} + \sum_{k=1}^N \hat{p}_{k_>}^2, \quad (7.8)$$

where $k_>$ is the dangling edge corresponding to loop k , which will become the edge that connects loops k and $k+1$ in the cylinder.

We can now construct \hat{V} using the graph manipulation techniques of Section 6.7.2. We describe the two moves needed in Figure 7.3 and we build the complete map \hat{V} by applying the moves to each loop and dangling edge pair $k, k_>$ in turn.

That we can map between the two Hilbert spaces does not yet make the physics of the two models equivalent, however. To determine whether this is true, we must examine how the Hamiltonian (7.8) transforms under \hat{V} . As exemplified in Section 6.7.2, plaquette operators transform as expected (as illustrated in Figure 7.3). The \hat{p}^2 terms, however, behave in a more complicated way: Those acting on the dangling edges in (7.8), because these edges are the control systems of the controlled rotations in \hat{V} , transform nontrivially, resulting in sums of terms that couple edges locally, such as $\sum_{\alpha} \hat{p}_{\alpha}^L \otimes \hat{p}_{\alpha}^R$. This is shown in Section 6.7.2.

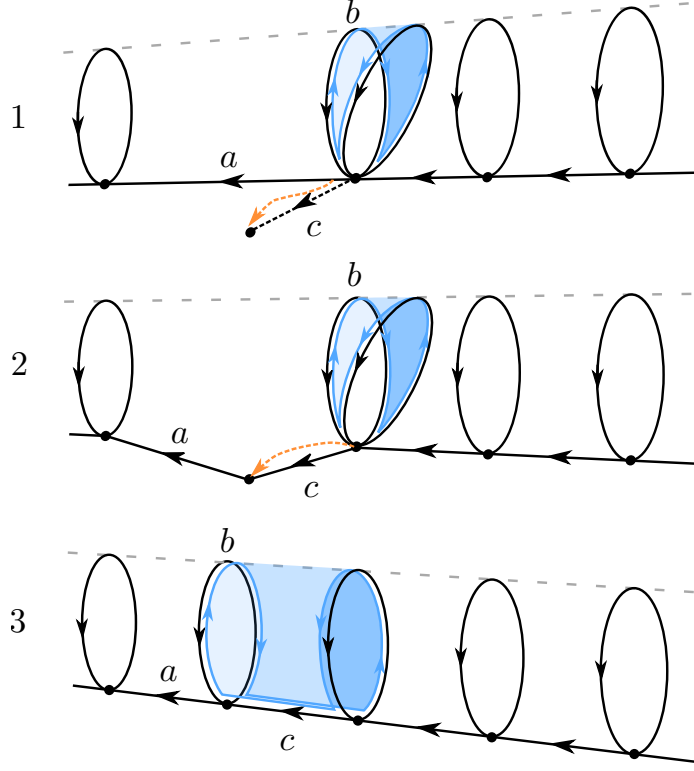


Figure 7.3: Illustration of the moves needed to map from the earring graph to the cylinder. We begin with a dangling edge c , where we initially need one per loop, which we integrate into the existing graph by transporting the beginning of edge a along it. This move, $1 \rightarrow 2$ is implemented by $\widehat{CL}_{c,a}$. In $2 \rightarrow 3$ we then move the loop b along the new connecting edge c using $\widehat{CL}_{c,b}\widehat{CR}_{c,b}$. The blue object illustrates a plaquette operator and shows how it transforms. See Section 6.7.2 for relevant definitions as well as a simple example.

However, any terms $\widehat{V}\widehat{p}_{k_{>}}^2\widehat{V}^\dagger$ in the cylinder arising from a $\widehat{p}_{k_{>}}^2$ term on a dangling edge of (7.8) must, taken together, act trivially on the physical subspace. We know this because any gauge-invariant state must have any dangling edges decoupled and in the rotation-invariant state $|00\rangle_0$, which has $\widehat{p}^2|00\rangle_0 = 0$ and so for the earring plus dangling edges $k_{>}$,

$$\widehat{p}_{k_{>}}^2|\psi\rangle_{\text{phys}} = 0 \quad (7.9)$$

for $|\psi\rangle_{\text{phys}} \in \mathcal{H}_{\text{phys, KS} + \text{dangling}}$. It is now easy to see that the terms on the cylinder arising from the dangling edge terms $\widehat{V}\widehat{p}_{k_{>}}^2\widehat{V}^\dagger$ annihilate all physical states and can play no role in the dynamics, since on the transformed state we have

$$(\widehat{V}\widehat{p}_{k_{>}}^2\widehat{V}^\dagger)\widehat{V}|\psi\rangle_{\text{phys}} = 0, \quad (7.10)$$

where $\widehat{V}^\dagger\widehat{V} = \mathbb{I}$. But this means the resulting cylinder Hamiltonian $\widehat{V}H_{\text{KS} + \text{dangling}}\widehat{V}^\dagger$ contains no $\widehat{p}_{k_{>}}^2$ that are not cancelled out by (7.10) on the physical subspace: There is no other way new $\widehat{p}_{k_{>}}^2$ terms could be generated, since the graph manipulation moves of

Figure 7.3 act trivially on the remaining \hat{p}_k^2 in (7.8) and never produce \hat{p}^2 terms when acting on plaquettes (see Section 6.7.2).

For this reason, the nonabelian earring model is *not physically equivalent* to the nonabelian cylinder with its natural Kogut-Susskind Hamiltonian (7.3), but rather to the cylinder with the earring Hamiltonian (7.1) — which lacks the $\hat{p}_{k>}^2$ terms of (7.3). The latter model will have different physics to the usual cylinder due to the omission of these terms, since high kinetic energy is not penalised on the connecting edges.

7.2.3 The quantum rotor model

The Hawaiian earring model (7.1) is known to be equivalent to the $O(N)$ rotor model (see, for example, [190]) given by

$$H_R(\tilde{g}) = \frac{\sqrt{\tilde{\eta}\tilde{g}}}{2a} \sum_{k=1}^N \hat{J}_k^2 - \frac{\sqrt{\tilde{\eta}}}{\tilde{g}a} \sum_{k=1}^{N-1} \hat{n}_k \cdot \hat{n}_{k+1}, \quad (7.11)$$

where the N -component vector of operators \hat{n} represents a position on the unit sphere in \mathbb{R}^N and \hat{J}^2 is the corresponding kinetic energy. The $\hat{n}_k \cdot \hat{n}_{k+1}$ term couples nearest-neighbour rotors, energetically favouring alignment. The rotor model is clearly symmetric under global rotations, as well as reflections, and thus has the symmetry group $O(N)$. In contrast to the lattice gauge theory model, there is no notion of nonphysical states in the rotor context, where all states are considered physical.

The rotor model is equivalent to the lattice gauge theory model (7.1) in the sense that their Hamiltonians and their (full) Hilbert spaces are equivalent, ignoring additional restrictions to physical subspaces. As such, in the case where the gauge theory possesses nonphysical states the *physics* of the two models need *not* be equivalent. Nevertheless, the *ground states* of the models must be equivalent in the case of continuous gauge groups since continuous symmetries cannot be spontaneously broken in (1+1)-dimensional systems in the presence of fluctuations [84, 85], which occur here for any finite value of g since the order-parameter \hat{n} does not commute with the Hamiltonian due to the \hat{J}^2 term. However, excited states may indeed break the symmetry.

The precise relation between the rotor model (7.11) and the lattice gauge theory model (7.1) is given by $H_{KS}(g) = H_R(\tilde{g})$ for $G = SU(2)$ with $N = 4$ and for $G = U(1)$ with $N = 2$, using the relations listed in Table 7.1.

In the case of the $O(4)$ rotor, the equivalence of the models is ultimately due to $SU(2) \times SU(2)$ being the double cover of $SO(4)$, as pointed out in Section 6.3, where the action of $SU(2) \times SU(2)$ is implemented on $L^2(SU(2))$ as $(g_1, g_2) \mapsto \hat{L}_{g_1} \hat{R}_{g_2}$. Note that reflections do not play a role in the dynamics of the rotor model, so we may think of the $O(4)$ rotor as the $SO(4)$ rotor. As a result, the Lie algebra of $SO(4)$ (and of $O(4)$) is isomorphic to $su(2) \times su(2)$ and the two $su(2)$ factors correspond to are implemented as \hat{p}_α^L and \hat{p}_α^R , in our formulation (see Section 6.5). The quadratic Casimir operator \hat{p}^2 is thus also the Casimir operator for the rotor \hat{J}^2 , up to a factor. The four \hat{n}_μ “position” operators of the rotor model are related to the lattice $SU(2)$ position operators $\hat{u}_{j,k}^l$ via the isomorphism relating $SU(2)$ to the 3-sphere S^3 from Section 6.3, according to which $\frac{1}{2} \text{tr}(\tau^\mu \dagger U)$ extracts

$O(N)$ Rotor	KS: $G \cong U(1)$	KS: $G \cong SU(2)$
N	2	4
\tilde{g}	$g^2/\sqrt{2}$	$g^2/4$
\hat{J}_k^2	\hat{p}_k^2	$4\hat{p}_k^2$
\hat{n}_k^μ	$(\text{Re}(\hat{u}_k), \text{Im}(\hat{u}_k))^\mu,$ $\mu = 1, 2$	$\left[\frac{1}{2} \text{tr}(\tau^\mu \hat{\mathbf{u}}_k)\right]^\mu,$ $\mu = 0 \dots 3$

Table 7.1: This table shows how quantities in the rotor model (7.11) must be set to obtain equivalence to the Kogut-Susskind model (7.1) ($H_{\text{KS}}(g) = H_{\text{R}}(\tilde{g})$) for the gauge groups $G \cong U(1)$ and $G \cong SU(2)$. The matrices τ^μ are defined in (6.10). We choose the numerical factors on the rotor model operators and parameters to match the usual definitions (see, for example [40]).

the μ -component of the vector in \mathbb{R}^4 corresponding to $U \in SU(2)$. We may thus define

$$\hat{n}^\mu = \frac{1}{2} \text{tr}(\tau^\mu \hat{\mathbf{u}}), \quad (7.12)$$

where the matrices τ^μ are defined in (6.10). We can then verify the commutation relations [191]

$$[\hat{p}_\alpha^L, \hat{n}^\beta] = -\frac{i}{2} \left(\sum_\gamma \epsilon_{\alpha\beta\gamma} \hat{n}^\gamma + \delta_{\alpha\beta} \hat{n}^0 \right), \quad \alpha, \beta, \gamma = 1 \dots 3, \quad (7.13)$$

$$[\hat{p}_\alpha^L, \hat{n}^0] = \frac{i}{2} \hat{n}^\alpha, \quad \alpha = 1 \dots 3, \quad \text{and} \quad (7.14)$$

$$[\hat{n}^\alpha, \hat{n}^\beta] = 0, \quad (7.15)$$

where ϵ is the Levi-Civita symbol. It remains to be shown that the potential terms of H_{KS} and H_{R} are equivalent. Using $\hat{\mathbf{u}} = \sum_{\mu=0}^3 \hat{n}^\mu \tau^\mu$ we find

$$\text{tr}(\hat{\mathbf{u}}_k \hat{\mathbf{u}}_{k+1}^\dagger) = \sum_{\mu\nu} \hat{n}_k^\mu \hat{n}_{k+1}^\nu \text{tr}(\tau^\mu \tau^{\nu\dagger}) = 2\hat{n}_k \cdot \hat{n}_{k+1}, \quad (7.16)$$

where we have also used that \hat{n}^μ is Hermitian.

The relationship between the $O(2)$ rotor and the $U(1)$ lattice gauge theory is simpler, since the groups are isomorphic: $U(1) \cong SO(2)$. The kinetic terms are just the same and \hat{n} is just the Cartesian vector corresponding to the element of the unit circle in the complex plane $\hat{n} = (\text{Re}(\hat{u}), \text{Im}(\hat{u}))$.

There are at least two broad reasons to study the quantum rotor model in (1+1) dimensions: Its importance in condensed matter physics, and its connection to gauge theories in higher spatial dimension.

Connections to condensed matter systems

The rotor model is related to a number of more physically motivated models in condensed matter physics [76], making its physics relevant to the description of a large number of systems.

To briefly summarise: For $N = 1$ the rotor “spins” are restricted to being “up” or “down” and we recover the Ising model. For $N = 2$ spins take values on the circle and we have a quantum (1+1)D model related to the classical XY model via a quantum-classical mapping (see Chapter 2). The classical XY model is the $p \rightarrow \infty$ limit of the clock models described in Chapter 3. The $O(2)$ rotor also describes interacting bosons, where the countably infinite set of Fourier modes of each rotor can be thought of as a boson occupation number and the alignment term serves as a nearest-neighbour hopping interaction. The $N = 3$ case describes the low-energy physics of antiferromagnetic Heisenberg spin ladders, with pairs of spins mapping onto $O(3)$ rotors.

Connections to gauge theory

The rotor model is connected to gauge theory not only in the formal sense described in Section 7.2.3, but also in terms of its physics. Although the Hamiltonian (7.1) in (1+1) dimensions possesses a global gauge-group symmetry, rather than a local gauge symmetry, it nevertheless has a lot in common with Yang-Mills theory on more sophisticated graphs. Most importantly, the $O(N > 2)$ models are known to possess a single, gapped phase ending at the weak-coupling limit $g \rightarrow 0$ [76]. This is also expected of (3 + 1)D lattice QCD [170], which at strong coupling is known to be in a massive, confining phase that is believed to persist into the weak-coupling regime, thus explaining the observed confinement of quarks. In contrast, the $O(2)$ model has a phase transition (of Berezinskii-Kosterlitz-Thouless type [87], see Chapter 2) at finite coupling, transitioning into a deconfined, gapless phase at weaker couplings.

7.2.4 Previous studies

The continuum limit of the rotor models, the so-called $O(N)$ nonlinear sigma model [76], can be solved using the Bethe ansatz for $N > 2$ [188]. Continuum limits of quantum lattice models are taken by moving to a point of diverging lattice correlation length $\xi \rightarrow \infty$ (see Section 6.7.3 and [45]). Since the correlation length is finite for $N > 2$ at all nonzero values of the coupling, and only diverges as $g \rightarrow 0$, the continuum limit of the quantum rotor model is also the weak-coupling limit. The Bethe ansatz results for the nonlinear sigma model thus provide information about the weak-coupling scaling of the quantum rotor model [40].

The lattice $O(N)$ rotor model has also been thoroughly investigated using strong-coupling expansions [180, 192] of the (1+1)D quantum Hamiltonian model, high-temperature expansions (for example [193, 194]) and Monte Carlo numerics ([183–187] is an incomplete selection) of the 2D classical model, as well as using other methods, such as Lanczos diagonalisation with finite-size-scaling [195].

So far, however, numerical simulations of the *quantum* Hamiltonian model have not, to the best of the author’s knowledge, been performed. In the following section, we fill this gap using MPS simulations.

7.3 Numerical methods

We use uniform MPS (see Section 1.3) with local Hilbert space dimension d and bond dimension D , and with full translation invariance, as our variational class of states. The continuous position basis $|g\rangle$ of group elements $g \in G$ does not lend itself to use with MPS numerics, for which we require a discrete, finite basis $\simeq \mathbb{C}^d$. Instead we use the Fourier basis given by Theorem 6.3.1 (Peter-Weyl) and described in Section 6.4, where we denote the Fourier modes $|jk\rangle_l$ for $SU(2)$, with j and k enumerating a basis for the l th irrep, and $|n\rangle$, $n \in \mathbb{Z}$ for $U(1)$. In the strong coupling regime $g^2 \gg 1$, the kinetic \hat{p}^2 term of (7.1) strongly penalises higher irreps, so we can neglect them to good approximation at larger g^2 . We expect them to become more relevant as we near the weak coupling regime.

We set d to accommodate the basis states for all irreps up to a cutoff. For $U(1)$, all irreps are one-dimensional and labelled by $n \in \mathbb{Z}$, so a cutoff is defined via $|n| \leq n_{\max}$, giving us

$$d = 2n_{\max} + 1. \quad (7.17)$$

For $SU(2)$ we must sum up the dimensions of the irreps we wish to include

$$d = \sum_{l=0}^{l_{\max}} \dim(V_l)^2 = \sum_{l=0}^{l_{\max}} (2l+1)^2, \quad (7.18)$$

where $\dim(V_l)^2$ is the number of parameters in the matrices of irrep l , and $l = 0, \frac{1}{2}, 1, \frac{3}{2}, 2, \dots$ so that $d = 1, 5, 14, 30, 55, \dots$. Importantly, truncating the basis at a certain irrep level does not prevent representation of gauge-invariant states. To see this, observe that the rotations that implement the gauge transformations \hat{L} and \hat{R} , which we express in the Fourier basis in (6.43) and (6.44) respectively, do not mix irreps.

In this study, we use values of n_{\max} up to 10 and l_{\max} up to 2. The former requires $d = 21$, while the latter implies $d = 55$, which is unusually high for MPS numerics. We use algorithms with optimisations for high d described in Section 1.4.2, applying the nonlinear conjugate gradient (CG) method from Section 1.4.3 to obtain ground states. We converge all states up to an effective energy gradient norm (1.83) of $\leq 10^{-8}$. We then obtain low-lying excited states using the method of Section 1.4.5, always operating directly in the space of infinite, uniform MPS.

7.4 Results of numerical study

In this section we generally use the rotor model parameter \tilde{g} of (7.11) for better comparison with known results for the rotor model. It is related to g from the lattice gauge theory Hamiltonian (7.1) by Table 7.1.

7.4.1 Symmetry breaking

Since our choice of truncated basis is most appropriate at strong coupling, we study the system starting at strong coupling $1/\tilde{g} \rightarrow 0$ and then approaching weak-coupling as far

as possible whilst maintaining accuracy. We find, for both the $O(2)$ and the $O(4)$ rotor, that the MPS approximate ground state, for any fixed, finite D , breaks the global $O(N)$ symmetry at small values of the coupling \tilde{g} . As function of D , the location \tilde{g}_{SB} of the symmetry-breaking transition is confined to a relatively narrow region of parameter space, as shown in Figure 7.4. Since the breaking of a continuous symmetry is forbidden by the Mermin-Wagner theorem [84, 85], this must be a symptom of finite-entanglement effects [91–93]: The bond dimension needed to accurately represent the symmetric state must suddenly grow as we approach weak coupling. It is likely that $\tilde{g}_{\text{SB}}(D)$ is also affected by the irrep truncation, although it is not clear what the effect would be since it is possible to represent symmetric states regardless of the truncation level. We leave this question to be treated in future work.

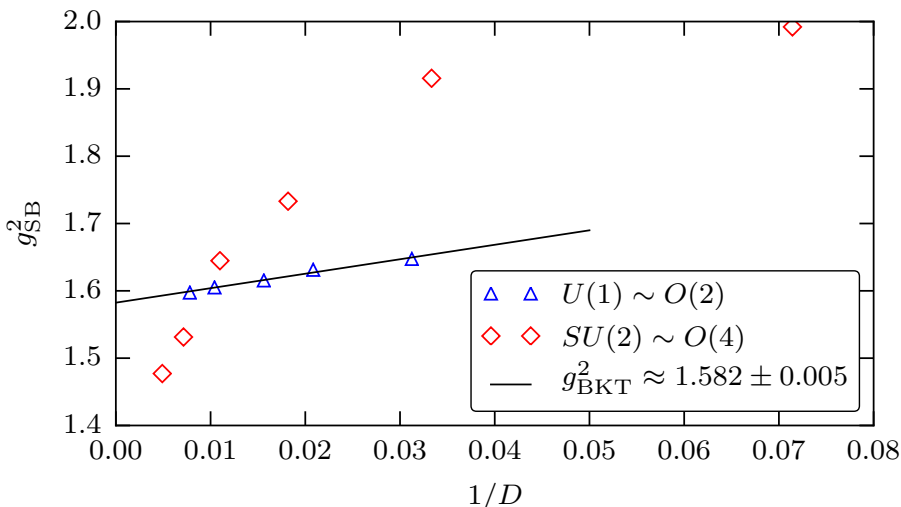


Figure 7.4: The location g_{SB}^2 of MPS ground state symmetry-breaking (SB) as a function of the MPS bond dimension D . We plot g_{SB}^2 for the Kogut-Susskind Hamiltonian rather than the rotor-model parameter \tilde{g}_{SB} as the scaling then favours plotting the results for $G = U(1)$ ($O(2)$ rotor) and $G = SU(2)$ ($O(4)$ rotor) on the same axes. Values of g_{SB}^2 were found using bisection up to a precision in g^{-2} of ± 0.005 . For $G = U(1)$, g_{SB}^2 tends towards a finite value. This value should correspond to the location g_{BKT}^2 of the BKT transition known to exist for the model [76]. The straight-line fit shown predicts a transition at $\tilde{g}_{\text{BKT}} = 1.119 \pm 0.004$ in terms of the $O(2)$ rotor parameter \tilde{g} . For $G = SU(2)$, the transition does not converge for the data available. This is consistent with it occurring at $g = \tilde{g} = 0$.

The $O(2)$ rotor is known to possess a gapless phase at weak coupling, characterised by algebraically decaying correlations such that the correlation length is infinite [76]. As shown in Section 1.3.5, a uniform MPS would require $D \rightarrow \infty$ to accurately represent such a ground state, thus explaining nonphysical symmetry-breaking in the MPS as an artifact of the significant approximation coming from working at finite D (see Section 2.3 for more details).

The existence of a phase transition at finite \tilde{g} also explains the narrowness of the region where symmetry-breaking begins. We expect the symmetry-breaking location $\tilde{g}_{\text{SB}}(D)$ to

converge to the location of the phase transition as $D \rightarrow \infty$ and indeed this convergence can be seen in Figure 7.4, where the extrapolated transition point agrees well with known estimates from strong-coupling expansions of β functions (and less well with results from other methods) [196]. Despite the impossibility of representing the ground state precisely in the gapless phase at weak coupling, the scaling of von Neumann entropy and correlation length in MPS ground states with a range of finite D can be used to estimate the central charge c of the conformal field theory (CFT) describing the phase (see Section 2.3.2). We fit data for $D = 22, 28, 34, \dots, 80$ at $1/(\tilde{g}\sqrt{2}) = 0.75, 0.8, 0.85, 0.9$ and find $c = 0.992 \pm 0.009$, matching the known result of $c = 1$ for the 2D classical XY model [78], which is identical with the 2D classical $O(2)$ rotor.

We now turn to the $O(4)$ rotor, which is known to exist in a single, gapped phase down to the weak-coupling limit $\tilde{g} \rightarrow 0$ [76]. We expect irrep truncation to become increasingly relevant as we approach weak-coupling due to the occupation of higher irrep modes. We also expect greater entanglement in the exact ground state at weaker couplings, as the potential term coupling nearest-neighbour edges begins to dominate, and the lattice correlation length grows. This is not enough, however, to explain the *suddenness* of the occurrence of nonphysical symmetry-breaking. This is likely due to the “crossover” phenomenon, a property of the $O(N > 2)$ models and of nonabelian gauge theories [45, 197], referring to persistence of strong-coupling behaviour up to a certain region of parameter space, where weak-coupling behaviour rapidly takes over. Despite the sudden change, the crossover phenomenon is not a phase transition in the sense of Chapter 2, as it is not accompanied by nonanalyticities in the ground state energy density. As such, we still expect the nonphysical symmetry-breaking transition to disappear as $D \rightarrow \infty$, as is indeed consistent with Figure 7.4.

7.4.2 Mass gap

Our next source of information is the mass gap, calculated using the MPS excitations ansatz described in Section 1.4.5. As explained in Chapter 2, the mass gap must vanish as we approach second or first-order transitions. Thus, if the mass gap does not approach zero in a region of parameter space, a phase transition cannot occur in that region. In the MPS approximation, the computed mass gap will generally be nonzero even if the true mass gap vanishes due to finite entanglement effects. However, as for the inverse of the correlation length (see Section 2.3), we expect signatures of the mass gap’s vanishing to be visible in the MPS approximation. Furthermore, errors due to finite entanglement should decrease with D , such that comparing data from MPS with various D is normally sufficient to detect them. The quantum rotor model mass gap can also be computed using strong-coupling series expansions [180], which we compare to our numerical results.

We find excellent agreement for both models up to the vicinity of the $O(2)$ phase transition and the $O(4)$ crossover region. Moving closer, Figure 7.5 shows that the mass gap descends towards zero at a finite coupling for $O(2)$, whereas for $O(4)$ the log-linear plot shows linear behaviour, indicating a finite mass gap for all finite couplings. For comparison, we plot the exact asymptotic weak-coupling scaling for $O(4)$ [188], taking into account speed-of-light renormalisation effects due to the stark space-time asymmetry of the Hamiltonian

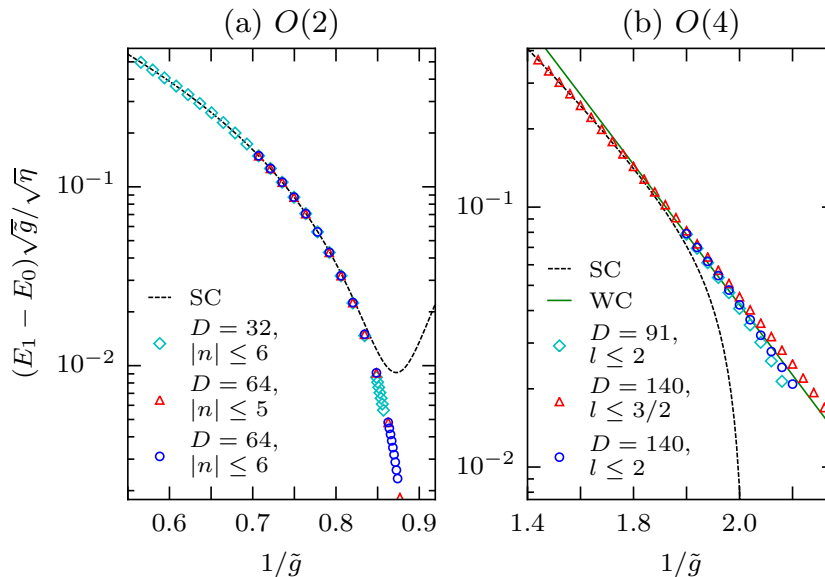


Figure 7.5: The MPS mass gap for (a) the $O(2)$ rotor and (b) the $O(4)$ rotor for bond dimensions D and irrep cutoffs in $|n|$ and l respectively. The strong coupling expansion of [180] is shown (SC), as is the weak coupling result (WC) for the $O(4)$ case, which is known exactly [188]. In (b), the curves are adjusted by an anisotropy parameter $\sqrt{\eta}$ to account for the renormalisation of the speed of light [190] (for $O(2)$, η is set to one). Near the phase transition for $O(2)$, and as we enter the weak coupling regime for $O(4)$, finite entanglement effects and, for $O(4)$, irrep cutoff effects become important.

discretisation [190].

We find very good agreement with the weak-coupling prediction, showing that we are successfully entering the asymptotic scaling regime. However, we also see from the plot that finite entanglement effects start to limit the accuracy: The $D = 140$ curve remains accurate further into the weak-coupling regime than the $D = 91$ curve, for fixed $l_{\max} = 2$. Furthermore, the irrep truncation level becomes significant: The $l_{\max} = 2$ curve is more accurate than the $l_{\max} = 3/2$ curve for fixed $D = 140$.

For this particular model, using a symmetric tensor network ansatz [198–200] would dramatically extend the range of accessible effective bond dimensions and so enable further penetration into the weak-coupling regime, although it would not allow access to the lowest-lying, symmetry-breaking excitations of the $O(4)$ model. Further, for a model with truly local gauge symmetry, methods such as that of [25] are required.

7.4.3 Low-lying excitations

We note in Section 7.2.3 that not all eigenstates of the rotor model (7.11) are physical states of the corresponding lattice gauge theory (7.1). In the case of the $U(1)$ gauge theory, gauge transformations are trivial and all eigenstates of the Hamiltonian (7.1) are physical. For $SU(2)$ this is not the case, and excited states may break the gauge symmetry.

We can test the gauge invariance of excited states by comparing states before and

after a gauge transformation using the overlap. To do this, we must use the general form $\langle \Phi[A, B] | \Phi[A', B'] \rangle = \langle \Phi[A, B] | \widehat{U}_{\mathcal{G}(g)} | \Phi[A, B] \rangle$ of the MPS tangent vector overlap. Compared to (1.89) we must add a second pseudo-inverse term to account for B_k , as well as B'_k , not satisfying any gauge fixing conditions for the case of comparing vectors from different tangent spaces. We must also replace all instances of the transfer matrix E_k by the overlap transfer matrix $E_{A'_k}^{A_k}$, defined in (1.28). The resulting overlap per lattice site is well-defined as long as $\langle \Psi[A] | \Psi[A'] \rangle = \langle \Psi[A] | \widehat{U}_{\mathcal{G}(g)} | \Psi[A] \rangle = 1$, which will be the case for a gauge-invariant ground state $|\Psi[A]\rangle$, and $\langle \Phi[A, B] | \Psi[A] \rangle = 0$, which we ensure by computing the excitations using the gauge-fixing parameterisation as described in Section 1.4.5.

Normalised states $|\Phi\rangle$ that are not gauge invariant satisfy

$$\langle \Phi | \widehat{P}_{\text{phys}} | \Phi \rangle \neq 1 \quad |\Phi\rangle \notin \mathcal{H}_{\text{phys}}, \quad (7.19)$$

with $\widehat{P}_{\text{phys}}$ as defined in (7.2), such that, for the $SU(2)$ earring model,

$$\exists g \in SU(2) : \text{Re}(\langle \Phi | \widehat{U}_{\mathcal{G}(g)} | \Phi \rangle) < 1 \quad |\Phi\rangle \notin \mathcal{H}_{\text{phys}}, \quad (7.20)$$

where $\widehat{U}_{\mathcal{G}(g)} = \bigotimes_k \widehat{L}_{g;k} \widehat{R}_{g;k}$. We can thus detect states that are not gauge invariant by sampling $\text{Re}(\langle \Phi | \widehat{U}_{\mathcal{G}(g)} | \Phi \rangle)$ over gauge transformations, choosing $g \in SU(2)$ uniformly with respect to the Haar measure. In Figure 7.6 we plot such results for the first 100 MPS tangent-space excitations for a particular value of \tilde{g} , sampling over a number of randomly-selected gauge transformations. We see that there are clear indications of gauge-invariant excitations, although the very lowest-lying energies are nonphysical. Indeed, the first gauge-invariant excitation occurs after three levels of degenerate, nonphysical excitations.

It is important to note that the MPS excitations ansatz does not capture all excited states — in particular, scattering states are excluded [201]. We expect, however, that the lowest-lying gauge-invariant excited state is a localised, single particle state, and can thus be captured by the MPS tangent-space ansatz [62]. If so, the energy relative to the ground state energy of the first gauge-invariant MPS excitation represents the mass gap of the $SU(2)$ Hawaiian earring model, which is larger than the $O(4)$ rotor mass gap represented by the lowest-lying, non-gauge-invariant excitation. In any case, assuming the lowest-lying $O(4)$ rotor excitation is particle-like, we may take the $O(4)$ rotor mass gap as a lower bound for the $SU(2)$ Hawaiian earring mass gap.

7.4.4 Beta functions

The beta function captures the rate of change of the coupling parameter \tilde{g} , needed to approximate the continuum field theory, with the lattice spacing a . See Section 6.7.3 for more details. In the case of the rotor model which, we have seen, is equivalent to a Kogut-Susskind lattice gauge theory, we may define the mass gap in “lattice energy units” as

$$F(\tilde{g}) \equiv 2a(E_1(\tilde{g}) - E_0(\tilde{g}))/\tilde{g}, \quad (7.21)$$

where E_1 is the energy of the first excitation and E_0 is the ground state energy, which allows us to write the beta function as

$$-\beta(\tilde{g})/\tilde{g} = \left(1 - \frac{4}{\tilde{g}^2} \frac{F'(\tilde{g})}{F(\tilde{g})}\right)^{-1}, \quad (7.22)$$

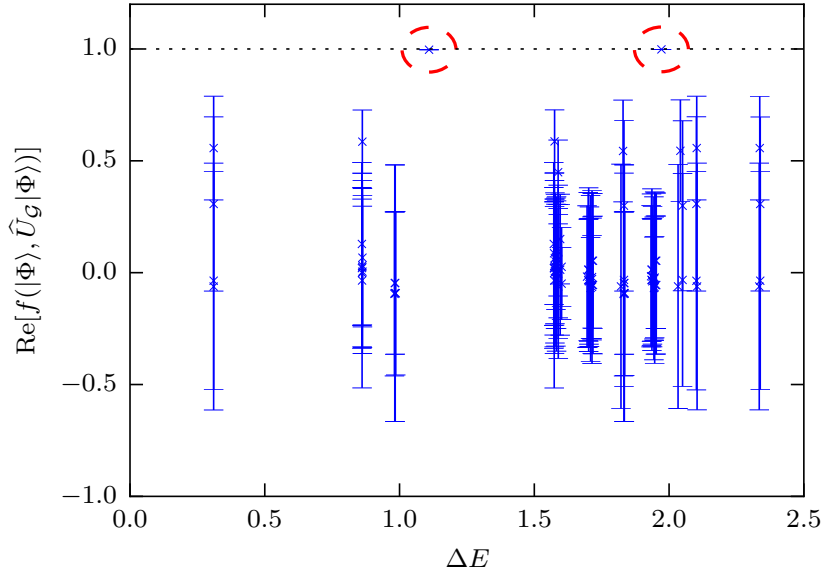


Figure 7.6: The real component of the fidelity f per site of MPS excitations $|\Phi\rangle$ under gauge transformations $\hat{U}_{\mathcal{G}(g)}$, plotted against the excitation energy $\Delta E \equiv E_n - E_0$ for excitation n , for the $SU(2)$ Hawaiian earring ($O(4)$ rotor model) at $1/g^2 = 0.4$ (or $1/\tilde{g} = 1.6$). We sample over $u \in SU(2)$ uniformly with respect to the Haar measure, averaging the result of 20 samples for this plot. The ground state is an MPS at $D = 30$ and we use $n_{\max} = 3$ as an irrep cutoff. The first 100 MPS tangent space excitations are plotted, where two of them (circled in red) appear to be approximately gauge invariant: They have a fidelity per site close to one and a variance (under the sampling) of nearly zero, in stark contrast to the other excitations.

where we use the same sign convention as in (6.90). Using our MPS results for the mass gap, we can thus compute the beta function, using finite differences to find $F'(\tilde{g})$.

The rotor model beta function can be computed perturbatively in the weak-coupling limit for $O(N > 2)$, and is given by (see, for example [180, 202])

$$-\beta(\tilde{g}) = (N - 2)\tilde{g}^2/2\pi + (N - 2)\tilde{g}^3/4\pi^2. \quad (7.23)$$

In [180], Hamer et al. use strong coupling expansions for $F(\tilde{g})$, combined with this perturbation-theory result, to construct a Padé approximant for the beta function intended to cover the full range of \tilde{g} . For the $O(2)$, where there is a phase transition at finite \tilde{g} , they rely solely on the strong coupling expansion for $F(\tilde{g})$.

We compare our MPS results with the Padé approximants of Hamer et al., as well as the weak-coupling result for $O(4)$ (7.23), in Figure 7.7, observing excellent agreement at stronger couplings, with the numerical results deviating from the approximate curve as we near weak coupling.

In the case of $O(2)$, where $\beta(\tilde{g})$ has a zero at the phase transition, the numerical data appears to predict a higher value for the transition location than the Padé approximant, in good agreement with our result from Figure 7.4.

The $O(4)$ our data ceases to follow the Padé curve as we enter the crossover region,

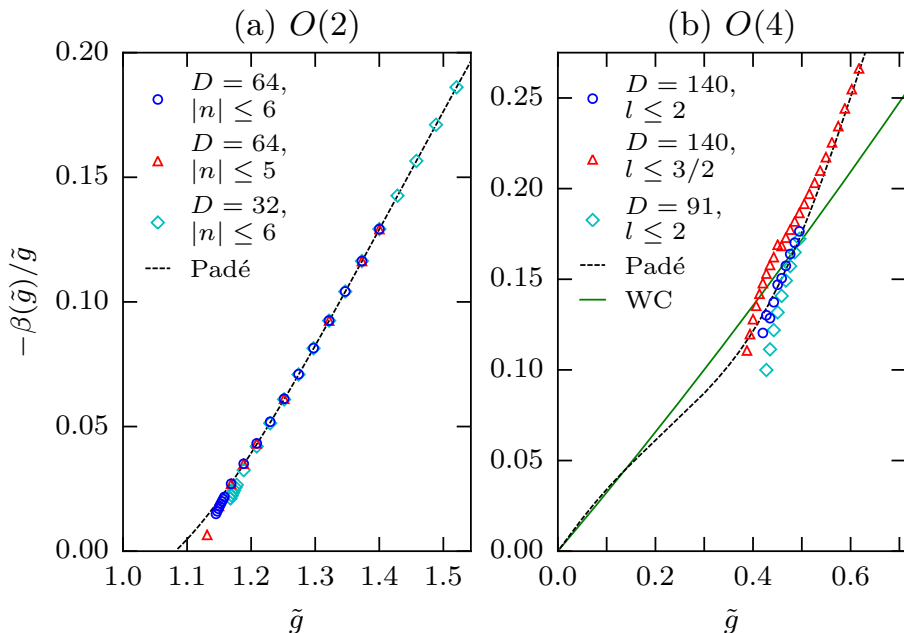


Figure 7.7: Beta functions determined from the MPS mass gap for (a) the $O(2)$ rotor and (b) the $O(4)$ rotor, together with a Padé approximant based on a strong-coupling expansion and the weak coupling result (WC) for the nonabelian case [180]. For $O(4)$ it is clear from the $D = 140$, $l_{\max} = 3/2$ curve that the numerical results begin to qualitatively follow the weak coupling behaviour. However, there are clearly systematic errors present. This is expected because the beta function involves the numerical derivative of the mass gap, making it sensitive to small inaccuracies due to finite entanglement and irrep truncation.

but does not succeed in following the weak-coupling result accurately either. This is not unexpected, as both approximations are likely inaccurate in the crossover region. It is clear however, that our results ultimately deviate from the exact behaviour, since we see large variations with D and l_{\max} , particularly as we near the nonphysical symmetry-breaking transition, as well as a tendency towards $\beta(\tilde{g}) = 0$ at finite values of \tilde{g} . Higher bond dimensions appear to mitigate this behaviour, suggesting it is largely a finite-entanglement artifact, which is consistent with Figure 7.4.

That errors are more visible for the β function than for the mass gap is expected since the numerical derivative amplifies small errors in the mass gap. We would need to reach higher bond dimensions and irrep cutoffs to achieve accurate results further into the weak-coupling regime. A further way of reducing noise would be to compute the derivative $F'(\tilde{g})$ analytically from the MPS excited state (see Section 2.3.1).

7.5 Discussion of results

We have seen that the two possible sources of error — finite-entanglement effects and local Fourier basis truncation — become especially important for the accurate reproduction of the mass gap and the beta function of the nonabelian rotor model. There are some obvious

ways of improving these results, such as increasing the MPS bond dimension and raising the irrep cutoff, as well as working with a symmetric MPS ansatz where appropriate to improve computational efficiency. Note, however, that the latter would not be appropriate for determining the rotor model mass gap, whose lowest-lying excitations break $O(N)$ symmetry (see Section 7.4.3).

Our numerical study demonstrates that tensor network state (TNS) methods, in this case uniform MPS, can successfully represent states of the nonabelian quantum rotor model into the weak-coupling regime. The use of a truncated local basis successfully and efficiently captures strong-coupling physics, but becomes a more severe limitation at weak couplings where, additionally, the spatial entanglement grows substantially.

This is promising for TNS approaches to pure nonabelian gauge theory which, as mentioned in Section 7.2.3, is believed to possess a very similar phase diagram to the $O(N)$ rotor models and, on the “Hawaiian earring” graph, is indeed equivalent to the rotor models studied here. Our study also suggests that high spatial entanglement is a feature of the theory from the crossover region onward, into weak-coupling. This may pose a challenge for numerical approaches if it carries over to higher dimensional nonabelian lattice gauge theory, since large bond dimensions may be needed to access the asymptotic scaling regime. It is possible that a symmetric TNS ansatz, or a different choice of basis, could be used to avoid this problem.

Concluding remarks and future directions

In Chapters 4 and 5 we have clearly demonstrated the utility of approximate tensor network state (TNS) techniques, in the form of variational algorithms for matrix product states (MPS), for the determination of phase diagrams of one-dimensional quantum lattice systems. The phase-diagram “sketching” methods of Chapter 2 allowed us to discover in Chapter 4 an apparently gapped phase in the interacting Kitaev edge model with repulsive interactions, as well as a floating incommensurate phase. This constitutes an example of the effect of interactions on a weak topological insulator that could be realised experimentally as a 2D array of Kitaev wires. A natural extension of this work would be to use two-dimensional TNS techniques, such as PEPS [9, 10], to characterise a more realistic model of the entire 2D setup, rather than just the edge. In Chapter 5 we used phase-diagram sketching extensively to characterise three different instances of the ANNC model, finding a rich variety of phases, including modulated commensurate and floating incommensurate phases. Of particular interest is the unexpected appearance of a commensurate critical phase of the $p = 3$ ANNC model, occurring at low external field strengths for larger values of the next-nearest-neighbour interaction strength. This phase may be better understood by further analytical and numerical analysis of the model. For example, the phase might be identical with the antiferromagnetic $p = 3$ clock model, with a connection in the J direction (strength of the nearest-neighbour coupling), which we have not yet explored.

We might imagine a more general application of phase-diagram sketching with MPS. At least for one-dimensional systems, they could be used to systematically explore a large subset of condensed matter models (in particular, those with short-range interactions), using an automated procedure to build up a higher-dimensional “mother phase diagram”, with a dimension for each interaction term (chosen from a catalogue of interesting or natural terms), locating and characterising gapless phases, using finite-entanglement scaling, as well as gapped phases. One could also extend this idea to higher-dimensional systems, using other TNS like PEPS [9, 10]. However, unlike MPS, even computing expectation values is a computationally intensive procedure in these higher-dimensional networks, making such a project significantly more difficult [203].

In our study of the quantum rotor model in Chapter 7, we have shown that TNS techniques are applicable to lattice gauge theory even in the case of a nonabelian continuous gauge group, where we used a movable local basis cutoff, defined in terms of gauge-group

Fourier modes, to make the local Hilbert space finite-dimensional. In contrast to Chapters 4 and 5, we made heavy use in Chapter 7 of the MPS tangent-space excitations ansatz of [60] in order to directly determine the mass gap and the beta function, as well as to identify gauge-invariant excitations of the nonabelian model. Although the rotor model studied does not have local gauge symmetry, the techniques used should easily extend to the more general case. Indeed, one logical next step would be to simulate a one-dimensional nonabelian model with local gauge symmetry, such as the cylinder described in Section 7.2.2. Isolating the physical states would be more challenging than for the rotor/earring case, where we sampled over the possible gauge transformations to test invariance of excitations, since the number of gauge group elements needed to specify a transformation grows linearly with the cylinder length. One might consider constructing the projector onto the physical subspace as a matrix product operator, as trialled in [57] in the context of anyon chains and proposed for PEPS in [181, 182] in the context of lattice gauge theory.

The usefulness of the graph-manipulation moves of Chapter 6, introduced for lattice gauge theory with continuous gauge groups in [165], has not yet been fully explored. It may be possible to find connections between lattice gauge theories on different graphs that could then be exploited to make the analytical or numerical treatment of interesting graphs more convenient. The application proposed in [165] — a scheme using graph manipulation to move to a finer graph-discretisation in such a way as to approach the continuum limit of Yang-Mills theory — could also be trialled using MPS simulations of the rotor model. The author has already begun this work.

Another related line of enquiry would be to investigate the discretisation of the gauge group in the nonabelian case as an alternative to a Fourier mode cutoff. Much as the clock model, with its \mathbb{Z}_p symmetry, becomes the $O(2)$ rotor model as $p \rightarrow \infty$, one could investigate, using discrete nonabelian groups, a limit leading to a nonabelian $O(N)$ rotor model. This limit could also be taken for the rotor model, or for a lattice gauge theory with local gauge symmetry, where it may represent a more efficient means of simulating such models numerically near the weak coupling limit, where the Fourier basis becomes less helpful. Discrete nonabelian gauge groups, such as the dihedral group D_3 , have been considered in the past in the context of models for quantum computation [204].

As numerical tools for treating quantum lattice systems, it is clear from the success of the studies of this thesis, and those of other publications, that tensor network states have the potential to significantly advance our understanding of a wide range of systems and states. While our studies have been limited to one-dimensional systems using MPS, other ansatzes like PEPS [9, 10] and the MERA [11, 12] allow the treatment of higher-dimensional systems, albeit at far higher computational cost. A key challenge to their use in numerics is the development of scalable, parallel algorithms that allow their use in large scale computations on super-computer architectures. This is likely to go hand in hand with developments in the theory of efficient (approximate) tensor network contraction.

Bibliography

- [1] S. R. White, ‘Density matrix formulation for quantum renormalization groups’, *Phys. Rev. Lett.* **69**, 2863 (1992).
- [2] U. Schollwöck, ‘The density-matrix renormalization group in the age of matrix product states’, *Ann. Phys.* **326**, 96 (2011).
- [3] M. Fannes, B. Nachtergaele and R. F. Werner, ‘Finitely correlated states on quantum spin chains’, *Commun. Math. Phys.* 1965-1997 **144**, 443 (1992).
- [4] S. Rommer and S. Östlund, ‘Class of ansatz wave functions for one-dimensional spin systems and their relation to the density matrix renormalization group’, *Phys. Rev. B* **55**, 2164 (1997).
- [5] G. Vidal, ‘Efficient Simulation of One-Dimensional Quantum Many-Body Systems’, *Phys. Rev. Lett.* **93**, 040502 (2004).
- [6] J. Haegeman, J. I. Cirac, T. J. Osborne, I. Pižorn, H. Verschelde and F. Verstraete, ‘Time-Dependent Variational Principle for Quantum Lattices’, *Phys. Rev. Lett.* **107**, 070601 (2011).
- [7] W. von der Linden, ‘A quantum Monte Carlo approach to many-body physics’, *Phys. Rep.* **220**, 53 (1992).
- [8] X. Chen, Z.-C. Gu and X.-G. Wen, ‘Classification of gapped symmetric phases in one-dimensional spin systems’, *Phys. Rev. B* **83**, 035107 (2011).
- [9] F. Verstraete and J. I. Cirac, ‘Renormalization algorithms for Quantum-Many Body Systems in two and higher dimensions’, (2004), [arXiv:cond-mat/0407066](https://arxiv.org/abs/cond-mat/0407066).
- [10] F. Verstraete, V. Murg and J. I. Cirac, ‘Matrix product states, projected entangled pair states, and variational renormalization group methods for quantum spin systems’, *Adv. Phys.* **57**, 143 (2008).
- [11] G. Vidal, ‘Entanglement Renormalization’, *Phys. Rev. Lett.* **99**, 220405 (2007).
- [12] G. Vidal, ‘Entanglement Renormalization: an introduction’, (2009), [arXiv:0912.1651](https://arxiv.org/abs/0912.1651).
- [13] M. Aguado and G. Vidal, ‘Entanglement Renormalization and Topological Order’, *Phys. Rev. Lett.* **100**, 070404 (2008).
- [14] N. Schuch, I. Cirac and D. Pérez-García, ‘PEPS as ground states: Degeneracy and topology’, *Annals of Physics* **325**, 2153 (2010).

- [15] M. B. Şahinoğlu, D. Williamson, N. Bultinck, M. Mariën, J. Haegeman, N. Schuch and F. Verstraete, ‘Characterizing Topological Order with Matrix Product Operators’, (2014), arXiv:1409.2150.
- [16] J. Maldacena, ‘The Large-N Limit of Superconformal Field Theories and Supergravity’, *International Journal of Theoretical Physics* **38**, 1113 (1999).
- [17] B. Swingle, ‘Entanglement renormalization and holography’, *Phys. Rev. D* **86**, 065007 (2012).
- [18] T. M. R. Byrnes, P. Sriganesh, R. J. Bursill and C. J. Hamer, ‘Density matrix renormalization group approach to the massive Schwinger model’, *Phys. Rev. D* **66**, 013002 (2002).
- [19] T. Sugihara, ‘Density matrix renormalization group in a two-dimensional $\lambda\phi^4$ Hamiltonian lattice model’, *J. High Energy Phys.* **2004**, 007 (2004).
- [20] T. Sugihara, ‘Matrix product representation of gauge invariant states in a \mathbb{Z}_2 lattice gauge theory’, *J. High Energy Phys.* **2005**, 022 (2005).
- [21] A. Milsted, J. Haegeman and T. J. Osborne, ‘Matrix product states and variational methods applied to critical quantum field theory’, *Phys. Rev. D* **88**, 085030 (2013).
- [22] M. C. Bañuls, K. Cichy, J. I. Cirac, K. Jansen and H. Saito, ‘Matrix Product States for Lattice Field Theories’, in *PoS Lattice*, Vol. 332 (2013).
- [23] M. C. Bañuls, K. Cichy, J. I. Cirac and K. Jansen, ‘The mass spectrum of the Schwinger model with matrix product states’, *J. High Energ. Phys.* **2013**, 1 (2013).
- [24] E. Rico, T. Pichler, M. Dalmonte, P. Zoller and S. Montangero, ‘Tensor Networks for Lattice Gauge Theories and Atomic Quantum Simulation’, *Phys. Rev. Lett.* **112**, 201601 (2014).
- [25] B. Buyens, J. Haegeman, K. Van Acoleyen, H. Verschelde and F. Verstraete, ‘Matrix Product States for Gauge Field Theories’, *Phys. Rev. Lett.* **113**, 091601 (2014).
- [26] B. Buyens, K. Van Acoleyen, J. Haegeman and F. Verstraete, ‘Matrix product states for Hamiltonian lattice gauge theories’, in *PoS Lattice*, Vol. 308 (31st Oct. 2014).
- [27] S. Kühn, E. Zohar, J. I. Cirac and M. C. Bañuls, ‘Non-Abelian string breaking phenomena with matrix product states’, *J. High Energ. Phys.* **2015**, 1 (2015).
- [28] K. Nomura, S. Ryu, M. Koshino, C. Mudry and A. Furusaki, ‘Quantum Hall Effect of Massless Dirac Fermions in a Vanishing Magnetic Field’, *Phys. Rev. Lett.* **100**, 246806 (2008).
- [29] Z. Ringel, Y. E. Kraus and A. Stern, ‘The strong side of weak topological insulators’, *Phys. Rev. B* **86**, 045102 (2012).
- [30] R. S. K. Mong, J. H. Bardarson and J. E. Moore, ‘Quantum Transport and Two-Parameter Scaling at the Surface of a Weak Topological Insulator’, *Phys. Rev. Lett.* **108**, 076804 (2012).
- [31] L. Fu and C. L. Kane, ‘Topology, Delocalization via Average Symmetry and the Symplectic Anderson Transition’, *Phys. Rev. Lett.* **109**, 246605 (2012).

- [32] P. Baireuther, J. M. Edge, I. C. Fulga, C. W. J. Beenakker and J. Tworzydło, ‘Quantum phase transitions of a disordered antiferromagnetic topological insulator’, *Phys. Rev. B* **89**, 035410 (2014).
- [33] Y. Tanaka, Z. Ren, T. Sato, K. Nakayama, S. Souma, T. Takahashi, K. Segawa and Y. Ando, ‘Experimental realization of a topological crystalline insulator in SnTe’, *Nat. Phys.* **8**, 800 (2012).
- [34] P. Dziawa, B. J. Kowalski, K. Dybko, R. Buczko, A. Szczerbakow, M. Szot, E. Łusakowska, T. Balasubramanian, B. M. Wojek, M. H. Berntsen, O. Tjernberg and T. Story, ‘Topological crystalline insulator states in $\text{Pb}_{1-x}\text{Sn}_x\text{Se}$ ’, *Nat. Mater.* **11**, 1023 (2012).
- [35] S.-Y. Xu, C. Liu, N. Alidoust, M. Neupane, D. Qian, I. Belopolski, J. Denlinger, Y. Wang, H. Lin, L. Wray, G. Landolt, B. Slomski, J. H. Dil, A. Marcinkova, E. Morosan, Q. Gibson, R. Sankar, F. C. Chou, R. J. Cava, A. Bansil and M. Z. Hasan, ‘Observation of a topological crystalline insulator phase and topological phase transition in $\text{Pb}_{1-x}\text{Sn}_x\text{Te}$ ’, *Nat. Commun.* **3**, 1192 (2012).
- [36] S. Elitzur, R. B. Pearson and J. Shigemitsu, ‘Phase structure of discrete Abelian spin and gauge systems’, *Phys. Rev. D* **19**, 3698 (1979).
- [37] G. Ortiz, E. Cobanera and Z. Nussinov, ‘Dualities and the phase diagram of the p-clock model’, *Nucl. Phys. B* **854**, 780 (2012).
- [38] E. Fradkin and L. P. Kadanoff, ‘Disorder variables and para-fermions in two-dimensional statistical mechanics’, *Nucl. Phys. B* **170**, 1 (1980).
- [39] J. B. Kogut, ‘An introduction to lattice gauge theory and spin systems’, *Rev. Mod. Phys.* **51**, 659 (1979).
- [40] J. B. Kogut, ‘Progress in lattice gauge theory’, *Phys. Rep.* **67**, 67 (1980).
- [41] L. Tagliacozzo, T. R. de Oliveira, S. Iblisdir and J. I. Latorre, ‘Scaling of entanglement support for matrix product states’, *Phys. Rev. B* **78**, 024410 (2008).
- [42] V. Stojevic, J. Haegeman, I. P. McCulloch, L. Tagliacozzo and F. Verstraete, ‘Conformal data from finite entanglement scaling’, *Phys. Rev. B* **91**, 035120 (2015).
- [43] W. Selke, ‘The ANNNI model — Theoretical analysis and experimental application’, *Phys. Rep.* **170**, 213 (1988).
- [44] L. Balents, ‘Spin liquids in frustrated magnets’, *Nature* **464**, 199 (2010).
- [45] M. Creutz, *Quarks, Gluons and Lattices* (Cambridge University Press, 27th June 1985).
- [46] A. Milsted and M. Lewerenz, *evoMPS*, GitHub, (2015) <https://github.com/amilsted/evoMPS>.
- [47] M. B. Hastings and T. Koma, ‘Spectral Gap and Exponential Decay of Correlations’, *Commun. Math. Phys.* **265**, 781 (2006).
- [48] M. B. Hastings, ‘An area law for one-dimensional quantum systems’, *J. Stat. Mech. Theory Exp.* **2007**, P08024 (2007).

- [49] I. Arad, Z. Landau and U. Vazirani, ‘Improved one-dimensional area law for frustration-free systems’, *Phys. Rev. B* **85**, 195145 (2012).
- [50] M. B. Hastings, ‘Solving gapped Hamiltonians locally’, *Phys. Rev. B* **73**, 085115 (2006).
- [51] N. de Beaudrap, M. Ohliger, T. J. Osborne and J. Eisert, ‘Solving Frustration-Free Spin Systems’, *Phys. Rev. Lett.* **105**, 060504 (2010).
- [52] L. Masanes, ‘Area law for the entropy of low-energy states’, *Phys. Rev. A* **80**, 052104 (2009).
- [53] P. Calabrese and J. Cardy, ‘Entanglement entropy and quantum field theory’, *J. Stat. Mech. Theory Exp.* **2004**, P06002 (2004).
- [54] F. Verstraete and J. I. Cirac, ‘Matrix product states represent ground states faithfully’, *Phys. Rev. B* **73**, 094423 (2006).
- [55] R. Koenig and V. B. Scholz, ‘Matrix product approximations to conformal field theories’, (2015), arXiv:1509.07414.
- [56] U. Schollwöck, ‘The density-matrix renormalization group’, *Rev. Mod. Phys.* **77**, 259 (2005).
- [57] P. E. Finch, H. Frahm, M. Lewerenz, A. Milsted and T. J. Osborne, ‘Quantum phases of a chain of strongly interacting anyons’, *Phys. Rev. B* **90**, 081111 (2014).
- [58] F. W. G. Transchel, A. Milsted and T. J. Osborne, ‘A Monte Carlo Time-Dependent Variational Principle’, (2014), arXiv:1411.5546.
- [59] A. Milsted, J. Haegeman, T. J. Osborne and F. Verstraete, ‘Variational matrix product ansatz for nonuniform dynamics in the thermodynamic limit’, *Phys. Rev. B* **88**, 155116 (2013).
- [60] J. Haegeman, B. Pirvu, D. J. Weir, J. I. Cirac, T. J. Osborne, H. Verschelde and F. Verstraete, ‘Variational matrix product ansatz for dispersion relations’, *Phys. Rev. B* **85**, 100408 (2012).
- [61] J. Haegeman, T. J. Osborne and F. Verstraete, ‘Post-matrix product state methods: To tangent space and beyond’, *Phys. Rev. B* **88**, 075133 (2013).
- [62] J. Haegeman, S. Michalakis, B. Nachtergaele, T. J. Osborne, N. Schuch and F. Verstraete, ‘Elementary Excitations in Gapped Quantum Spin Systems’, *Phys. Rev. Lett.* **111**, 080401 (2013).
- [63] J. Haegeman, C. Lubich, I. Oseledets, B. Vandereycken and F. Verstraete, ‘Unifying time evolution and optimization with matrix product states’, (2014), arXiv:1408.5056.
- [64] R. Orús, ‘A practical introduction to tensor networks: Matrix product states and projected entangled pair states’, *Annals of Physics* **349**, 117 (2014).
- [65] W. Press, S. Teukolsky, W. Vetterling and B. Flannery, *Numerical Recipes: The Art of Scientific Computing*, 3rd (Cambridge University Press, New York, 2007).

- [66] J. Haegeman, M. Mariën, T. J. Osborne and F. Verstraete, ‘Geometry of Matrix Product States: metric, parallel transport and curvature’, (2012), arXiv:1210.7710.
- [67] M. A. Nielsen and I. L. Chuang, *Quantum Computation and Quantum Information* (Cambridge University Press, Cambridge, 2000).
- [68] J. Nocedal and S. Wright, *Numerical Optimization* (Springer Science & Business Media, 11th Dec. 2006).
- [69] R. P. Brent, *Algorithms for Minimization Without Derivatives* (Prentice-Hall, 1972).
- [70] T. E. Oliphant, ‘Python for Scientific Computing’, *Comput. Sci. Eng.* **9**, 10 (2007).
- [71] R. R. B. Lehoucq, D. D. C. Sorensen and C. Yang, *Arpack User’s Guide: Solution of Large-Scale Eigenvalue Problems With Implicitly Restarted Arnoldi Methods* (SIAM, 1998).
- [72] NVIDIA, *NVIDIA Kepler GK110 Architecture White Paper*, (2012) <https://www.nvidia.com/content/PDF/kepler/NVIDIA-Kepler-GK110-Architecture-Whitepaper.pdf>.
- [73] A. Kloeckner, *Pycuda*, (2015) <https://pypi.python.org/pypi/pycuda>.
- [74] L. Givon, *Scikit-cuda*, (2015) <https://github.com/lebedov/scikit-cuda>.
- [75] H. E. Stanley, *Introduction to Phase Transitions and Critical Phenomena* (Oxford University Press, 1971).
- [76] S. Sachdev, *Quantum Phase Transitions*, 2nd ed. (Cambridge University Press, 9th May 2011).
- [77] M. M. Wolf, G. Ortiz, F. Verstraete and J. I. Cirac, ‘Quantum Phase Transitions in Matrix Product Systems’, *Phys. Rev. Lett.* **97**, 110403 (2006).
- [78] P. Francesco, P. Mathieu and D. Senechal, *Conformal Field Theory* (Springer Science & Business Media, 6th Dec. 2012).
- [79] B. Nachtergaele and R. Sims, ‘Lieb-Robinson Bounds and the Exponential Clustering Theorem’, *Commun. Math. Phys.* **265**, 119 (2006).
- [80] A. Zee, *Quantum Field Theory in a Nutshell: (Second Edition)* (Princeton University Press, 1st Feb. 2010).
- [81] M. E. Peskin and D. V. Schroeder, *An Introduction To Quantum Field Theory* (Westview Press, 2nd Oct. 1995).
- [82] L. Landau, ‘On the Theory of Phase Transitions’, *Zh. Eksp. Teor. Fiz.* **7**, 19 (1937).
- [83] L. Landau, ‘On the Theory of Phase Transitions’, *Ukr. J. Phys.* **53**, 25 (2008).
- [84] N. D. Mermin and H. Wagner, ‘Absence of Ferromagnetism or Antiferromagnetism in One- or Two-Dimensional Isotropic Heisenberg Models’, *Phys. Rev. Lett.* **17**, 1133 (1966).
- [85] S. Coleman, ‘There are no Goldstone bosons in two dimensions’, *Commun. Math. Phys.* **31**, 259 (1973).

- [86] V. L. Berezinskii, ‘Destruction of Long-range Order in One-dimensional and Two-dimensional Systems having a Continuous Symmetry Group I. Classical Systems’, *Sov. J. Exp. Theor. Phys.* **32**, 493 (1971).
- [87] J. M. Kosterlitz and D. J. Thouless, ‘Ordering, metastability and phase transitions in two-dimensional systems’, *J. Phys. C: Solid State Phys.* **6**, 1181 (1973).
- [88] J. M. Kosterlitz, ‘The critical properties of the two-dimensional xy model’, *J. Phys. C: Solid State Phys.* **7**, 1046 (1974).
- [89] P. Bak, ‘Commensurate phases, incommensurate phases and the devil’s staircase’, *Rep. Prog. Phys.* **45**, 587 (1982).
- [90] M. Beccaria, M. Campostrini and A. Feo, ‘Evidence for a floating phase of the transverse ANNNI model at high frustration’, *Phys. Rev. B* **76**, 094410 (2007).
- [91] H.-L. Wang, J.-H. Zhao, B. Li and H.-Q. Zhou, ‘Kosterlitz–Thouless phase transition and ground state fidelity: a novel perspective from matrix product states’, *J. Stat. Mech.* **2011**, L10001 (2011).
- [92] D. Draxler, J. Haegeman, T. J. Osborne, V. Stojevic, L. Vanderstraeten and F. Verstraete, ‘Particles, Holes, and Solitons: A Matrix Product State Approach’, *Phys. Rev. Lett.* **111**, 020402 (2013).
- [93] V. Zauner, D. Draxler, L. Vanderstraeten, M. Degroote, J. Haegeman, M. M. Rams, V. Stojevic, N. Schuch and F. Verstraete, ‘Transfer matrices and excitations with matrix product states’, *New J. Phys.* **17**, 053002 (2015).
- [94] D. Carfi, ‘The pointwise Hellmann-Feynman theorem’, *AAPP Phys. Math. Nat. Sci.* **88** (2010) 10.1478/C1A1001004.
- [95] P. Calabrese and J. Cardy, ‘Entanglement entropy and quantum field theory: a non-technical introduction’, *Int. J. Quantum Inform.* **04**, 429 (2006).
- [96] J. Alicea, ‘New directions in the pursuit of Majorana fermions in solid state systems’, *Rep. Prog. Phys.* **75**, 076501 (2012).
- [97] C. W. J. Beenakker, ‘Search for Majorana Fermions in Superconductors’, *Annu. Rev. Condens. Matter Phys.* **4**, 113 (2013).
- [98] C. Nayak, S. H. Simon, A. Stern, M. Freedman and S. Das Sarma, ‘Non-Abelian anyons and topological quantum computation’, *Rev. Mod. Phys.* **80**, 1083 (2008).
- [99] A. Kitaev, ‘Unpaired Majorana fermions in quantum wires’, *Phys.-Uspekhi* **44**, 131 (2001).
- [100] V. Mourik, K. Zuo, S. M. Frolov, S. R. Plissard, E. P. A. M. Bakkers and L. P. Kouwenhoven, ‘Signatures of Majorana Fermions in Hybrid Superconductor-Semiconductor Nanowire Devices’, *Science* **336**, 1003 (2012).
- [101] M. T. Deng, C. L. Yu, G. Y. Huang, M. Larsson, P. Caroff and H. Q. Xu, ‘Anomalous Zero-Bias Conductance Peak in a Nb–InSb Nanowire–Nb Hybrid Device’, *Nano Lett.* **12**, 6414 (2012).

- [102] H. O. H. Churchill, V. Fatemi, K. Grove-Rasmussen, M. T. Deng, P. Caroff, H. Q. Xu and C. M. Marcus, ‘Superconductor-nanowire devices from tunneling to the multichannel regime: Zero-bias oscillations and magnetoconductance crossover’, *Phys. Rev. B* **87**, 241401 (2013).
- [103] M. T. Deng, C. L. Yu, G. Y. Huang, M. Larsson, P. Caroff and H. Q. Xu, ‘Parity independence of the zero-bias conductance peak in a nanowire based topological superconductor-quantum dot hybrid device’, *Sci. Rep.* **4**, 7261 (2014).
- [104] N. H. Lindner, E. Berg, G. Refael and A. Stern, ‘Fractionalizing Majorana Fermions: Non-Abelian Statistics on the Edges of Abelian Quantum Hall States’, *Phys. Rev. X* **2**, 041002 (2012).
- [105] M. Cheng, ‘Superconducting proximity effect on the edge of fractional topological insulators’, *Phys. Rev. B* **86**, 195126 (2012).
- [106] D. J. Clarke, J. Alicea and K. Shtengel, ‘Exotic non-Abelian anyons from conventional fractional quantum Hall states’, *Nat. Commun.* **4**, 1348 (2013).
- [107] A. Vaezi, ‘Fractional topological superconductor with fractionalized Majorana fermions’, *Phys. Rev. B* **87**, 035132 (2013).
- [108] P. A. M. Dirac, ‘The Quantum Theory of the Emission and Absorption of Radiation’, *Proc. R. Soc. Lond. Math. Phys. Eng. Sci.* **114**, 243 (1927).
- [109] V. Fock, ‘Konfigurationsraum und zweite Quantelung’, *Z. Physik* **75**, 622 (1932).
- [110] L. E. Ballentine, *Quantum Mechanics: A Modern Development* (World Scientific, 1st Jan. 1998).
- [111] P. Jordan and E. Wigner, ‘Über das Paulische äquivalenzverbot’, *Z. Physik* **47**, 631 (1928).
- [112] E. Majorana and L. Maiani, ‘A symmetric theory of electrons and positrons’, in *Ettore Majorana Scientific Papers*, edited by G. F. Bassani (Springer Berlin Heidelberg, 2006), pp. 201–233.
- [113] W. Rodejohann, ‘Neutrino-less double beta decay and particle physics’, *Int. J. Mod. Phys. E* **20**, 1833 (2011).
- [114] E. Cobanera and G. Ortiz, ‘Fock parafermions and self-dual representations of the braid group’, *Phys. Rev. A* **89**, 012328 (2014).
- [115] H. S. Green, ‘A Generalized Method of Field Quantization’, *Phys. Rev.* **90**, 270 (1953).
- [116] O. W. Greenberg and A. M. L. Messiah, ‘Selection Rules for Parafields and the Absence of Para Particles in Nature’, *Phys. Rev.* **138**, B1155 (1965).
- [117] T. D. Schultz, D. C. Mattis and E. H. Lieb, ‘Two-Dimensional Ising Model as a Soluble Problem of Many Fermions’, *Rev. Mod. Phys.* **36**, 856 (1964).
- [118] P. Fendley, ‘Parafermionic edge zero modes in Zn-invariant spin chains’, *J. Stat. Mech.* **2012**, P11020 (2012).

- [119] F. Y. Wu, ‘The Potts model’, *Rev. Mod. Phys.* **54**, 235 (1982).
- [120] R. Bondesan and T. Quella, ‘Topological and symmetry broken phases of ZN parafermions in one dimension’, *J. Stat. Mech.* **2013**, P10024 (2013).
- [121] J. Motruk, E. Berg, A. M. Turner and F. Pollmann, ‘Topological phases in gapped edges of fractionalized systems’, *Phys. Rev. B* **88**, 085115 (2013).
- [122] A. Das, Y. Ronen, Y. Most, Y. Oreg, M. Heiblum and H. Shtrikman, ‘Zero-bias peaks and splitting in an Al–InAs nanowire topological superconductor as a signature of Majorana fermions’, *Nat. Phys.* **8**, 887 (2012).
- [123] L. P. Rokhinson, X. Liu and J. K. Furdyna, ‘The fractional a.c. Josephson effect in a semiconductor–superconductor nanowire as a signature of Majorana particles’, *Nat. Phys.* **8**, 795 (2012).
- [124] S. Nadj-Perge, I. K. Drozdov, J. Li, H. Chen, S. Jeon, J. Seo, A. H. MacDonald, B. A. Bernevig and A. Yazdani, ‘Observation of Majorana fermions in ferromagnetic atomic chains on a superconductor’, *Science* **346**, 602 (2014).
- [125] D. Wang, Z. Huang and C. Wu, ‘Fate and remnants of Majorana zero modes in a quantum wire array’, *Phys. Rev. B* **89**, 174510 (2014).
- [126] R. Wakatsuki, M. Ezawa and N. Nagaosa, ‘Majorana fermions and multiple topological phase transition in Kitaev ladder topological superconductors’, *Phys. Rev. B* **89**, 174514 (2014).
- [127] I. Seroussi, E. Berg and Y. Oreg, ‘Topological superconducting phases of weakly coupled quantum wires’, *Phys. Rev. B* **89**, 104523 (2014).
- [128] I. C. Fulga, B. van Heck, J. M. Edge and A. R. Akhmerov, ‘Statistical topological insulators’, *Phys. Rev. B* **89**, 155424 (2014).
- [129] M. Diez, I. C. Fulga, D. I. Pikulin, J. Tworzydło and C. W. J. Beenakker, ‘Bimodal conductance distribution of Kitaev edge modes in topological superconductors’, *New J. Phys.* **16**, 063049 (2014).
- [130] M. Z. Hasan and C. L. Kane, ‘Colloquium: Topological insulators’, *Rev. Mod. Phys.* **82**, 3045 (2010).
- [131] X.-L. Qi and S.-C. Zhang, ‘Topological insulators and superconductors’, *Rev. Mod. Phys.* **83**, 1057 (2011).
- [132] K. v. Klitzing, G. Dorda and M. Pepper, ‘New Method for High-Accuracy Determination of the Fine-Structure Constant Based on Quantized Hall Resistance’, *Phys. Rev. Lett.* **45**, 494 (1980).
- [133] H. L. Stormer, D. C. Tsui and A. C. Gossard, ‘The fractional quantum Hall effect’, *Rev. Mod. Phys.* **71**, S298 (1999).
- [134] A. Kitaev, ‘Periodic table for topological insulators and superconductors’, in *AIP Conference Proceedings*, Vol. 1134 (14th May 2009), pp. 22–30.

- [135] A. P. Schnyder, S. Ryu, A. Furusaki and A. W. W. Ludwig, ‘Classification of Topological Insulators and Superconductors’, in AIP Conference Proceedings, Vol. 1134 (14th May 2009), pp. 10–21.
- [136] L. Fidkowski and A. Kitaev, ‘Topological phases of fermions in one dimension’, Phys. Rev. B **83**, 075103 (2011).
- [137] C.-X. Liu, X.-L. Qi and S.-C. Zhang, ‘Half quantum spin Hall effect on the surface of weak topological insulators’, Phys. E, SI:Topological Insulators **44**, 906 (2012).
- [138] X. Chen, Z.-C. Gu, Z.-X. Liu and X.-G. Wen, ‘Symmetry-Protected Topological Orders in Interacting Bosonic Systems’, Science **338**, 1604 (2012).
- [139] X. Chen, Z.-C. Gu, Z.-X. Liu and X.-G. Wen, ‘Symmetry protected topological orders and the group cohomology of their symmetry group’, Phys. Rev. B **87**, 155114 (2013).
- [140] B. van Heck, E. Cobanera, J. Ulrich and F. Hassler, ‘Thermal conductance as a probe of the nonlocal order parameter for a topological superconductor with gauge fluctuations’, Phys. Rev. B **89**, 165416 (2014).
- [141] T. Senthil, ‘Symmetry-Protected Topological Phases of Quantum Matter’, Annu. Rev. Condens. Matter Phys. **6**, 299 (2015).
- [142] A. Milsted, L. Seabra, I. C. Fulga, C. W. J. Beenakker and E. Cobanera, ‘Statistical translation invariance protects a topological insulator from interactions’, Phys. Rev. B **92**, 085139 (2015).
- [143] A. Rahmani, X. Zhu, M. Franz and I. Affleck, ‘Phase Diagram of the Interacting Majorana Chain Model’, (2015), arXiv:1505.03966.
- [144] A. Rahmani, X. Zhu, M. Franz and I. Affleck, ‘Emergent Supersymmetry from Strongly Interacting Majorana Zero Modes’, Phys. Rev. Lett. **115**, 166401 (2015).
- [145] F. Hassler and D. Schuricht, ‘Strongly interacting Majorana modes in an array of Josephson junctions’, New J. Phys. **14**, 125018 (2012).
- [146] R. Thomale, S. Rachel and P. Schmitteckert, ‘Tunneling spectra simulation of interacting Majorana wires’, Phys. Rev. B **88**, 161103 (2013).
- [147] E. Cobanera, G. Ortiz and Z. Nussinov, ‘Unified Approach to Quantum and Classical Dualities’, Phys. Rev. Lett. **104**, 020402 (2010).
- [148] H. A. Kramers and G. H. Wannier, ‘Statistics of the Two-Dimensional Ferromagnet. Part I’, Phys. Rev. **60**, 252 (1941).
- [149] M. Bhattacharya and M. Kleinert, ‘Chiral symmetries associated with angular momentum’, Eur. J. Phys. **35**, 025007 (2014).
- [150] T. Senthil and M. P. A. Fisher, ‘Quasiparticle localization in superconductors with spin-orbit scattering’, Phys. Rev. B **61**, 9690 (2000).
- [151] N. Read and D. Green, ‘Paired states of fermions in two dimensions with breaking of parity and time-reversal symmetries and the fractional quantum Hall effect’, Phys. Rev. B **61**, 10267 (2000).

- [152] A. Vishwanath, ‘Quantized Thermal Hall Effect in the Mixed State of d-Wave Superconductors’, *Phys. Rev. Lett.* **87**, 217004 (2001).
- [153] H. W. J. Blöte, J. L. Cardy and M. P. Nightingale, ‘Conformal invariance, the central charge, and universal finite-size amplitudes at criticality’, *Phys. Rev. Lett.* **56**, 742 (1986).
- [154] H. T. Diep, *Frustrated Spin Systems*, 2nd ed. (World Scientific, May 2013).
- [155] A. Milsted, E. Cobanera, M. Burrello and G. Ortiz, ‘Commensurate and incommensurate states of topological quantum matter’, *Phys. Rev. B* **90**, 195101 (2014).
- [156] J.-F. Sadoc and R. Mosseri, *Geometrical Frustration* (Cambridge University Press, 23rd Nov. 2006).
- [157] M. Burrello, B. van Heck and E. Cobanera, ‘Topological phases in two-dimensional arrays of parafermionic zero modes’, *Phys. Rev. B* **87**, 195422 (2013).
- [158] M. Levin and A. Stern, ‘Fractional Topological Insulators’, *Phys. Rev. Lett.* **103**, 196803 (2009).
- [159] L. Fu and C. L. Kane, ‘Josephson current and noise at a superconductor/quantum-spin-Hall-insulator/superconductor junction’, *Phys. Rev. B* **79**, 161408 (2009).
- [160] J. Stephenson, ‘Two one-dimensional Ising models with disorder points’, *Can. J. Phys.* **48**, 1724 (1970).
- [161] A. M. Läuchli, ‘Operator content of real-space entanglement spectra at conformal critical points’, (2013), arXiv:1303.0741.
- [162] N. Laflorencie and S. Rachel, ‘Spin-resolved entanglement spectroscopy of critical spin chains and Luttinger liquids’, *J. Stat. Mech.* **2014**, P11013 (2014).
- [163] B. Swingle, ‘Structure of entanglement in regulated Lorentz invariant field theories’, (2013), arXiv:1304.6402.
- [164] J. Kogut and L. Susskind, ‘Hamiltonian formulation of Wilson’s lattice gauge theories’, *Phys. Rev. D* **11**, 395 (1975).
- [165] A. Milsted and T. J. Osborne, *Lattice gauge theory and tensor networks*, GitHub, (2015) <https://github.com/tobiasosborne/Lattice-gauge-theory-and-tensor-networks>.
- [166] J. C. Baez, ‘Spin Networks in Gauge Theory’, *Adv. Math.* **117**, 253 (1996).
- [167] N. Straumann, *General Relativity*, Graduate Texts in Physics (Springer Netherlands, Dordrecht, 2013).
- [168] C. N. Yang and R. L. Mills, ‘Conservation of Isotopic Spin and Isotopic Gauge Invariance’, *Phys. Rev.* **96**, 191 (1954).

- [169] N. Brambilla, S. Eidelman, P. Foka, S. Gardner, A. S. Kronfeld, M. G. Alford, R. Alkofer, M. Butenschoen, T. D. Cohen, J. Erdmenger, L. Fabbietti, M. Faber, J. L. Goity, B. Ketzer, H. W. Lin, F. J. Llanes-Estrada, H. B. Meyer, P. Pakhlov, E. Pallante, M. I. Polikarpov, H. Sazdjian, A. Schmitt, W. M. Snow, A. Vairo, R. Vogt, A. Vuorinen, H. Wittig, P. Arnold, P. Christakoglou, P. D. Nezza, Z. Fodor, X. G. i Tormo, R. Höllwieser, M. A. Janik, A. Kalweit, D. Keane, E. Kiritsis, A. Mischke, R. Mizuk, G. Odyniec, K. Papadodimas, A. Pich, R. Pittau, J.-W. Qiu, G. Ricciardi, C. A. Salgado, K. Schwenzer, N. G. Stefanis, G. M. von Hippel and V. I. Zakharov, ‘QCD and strongly coupled gauge theories: challenges and perspectives’, *Eur. Phys. J. C* **74**, 1 (2014).
- [170] J. Greensite, *An Introduction to the Confinement Problem*, Vol. 821, Lecture Notes in Physics (Springer Berlin Heidelberg, Berlin, Heidelberg, 2011).
- [171] J. A. Carlson, A. Jaffe, A. Wiles, C. M. Institute and A. M. Society, *The Millennium Prize Problems* (American Mathematical Soc., Jan. 2006).
- [172] S. Dürr, Z. Fodor, J. Frison, C. Hoelbling, R. Hoffmann, S. D. Katz, S. Krieg, T. Kurth, L. Lellouch, T. Lippert, K. K. Szabo and G. Vulvert, ‘Ab Initio Determination of Light Hadron Masses’, *Science* **322**, 1224 (2008).
- [173] S. Lang, *Algebra*, red. by S. Axler, F. W. Gehring and K. A. Ribet, Vol. 211, Graduate Texts in Mathematics (Springer New York, New York, NY, 2002).
- [174] B. C. Hall, *Lie Groups, Lie Algebras, and Representations*, Vol. 222, Graduate Texts in Mathematics (Springer International Publishing, Cham, 2015).
- [175] D. Bump, *Lie Groups* (Springer Science & Business Media, 17th June 2004).
- [176] F. Peter and H. Weyl, ‘Die Vollständigkeit der primitiven Darstellungen einer geschlossenen kontinuierlichen Gruppe’, *Math. Ann.* **97**, 737 (1927).
- [177] A. Alex, M. Kalus, A. Huckleberry and J. von Delft, ‘A numerical algorithm for the explicit calculation of SU(N) and SL(N,C) Clebsch–Gordan coefficients’, *J. Math. Phys.* **52**, 023507 (2011).
- [178] K. G. Wilson, ‘Confinement of quarks’, *Phys. Rev. D* **10**, 2445 (1974).
- [179] T. Eguchi, P. B. Gilkey and A. J. Hanson, ‘Gravitation, gauge theories and differential geometry’, *Physics Reports* **66**, 213 (1980).
- [180] C. J. Hamer, J. B. Kogut and L. Susskind, ‘Strong-coupling expansions and phase diagrams for the O(2), O(3), and O(4) Heisenberg spin systems in two dimensions’, *Phys. Rev. D* **19**, 3091 (1979).
- [181] L. Tagliacozzo, A. Celi and M. Lewenstein, ‘Tensor Networks for Lattice Gauge Theories with Continuous Groups’, *Phys. Rev. X* **4**, 041024 (2014).
- [182] J. Haegeman, K. Van Acoleyen, N. Schuch, J. I. Cirac and F. Verstraete, ‘Gauging Quantum States: From Global to Local Symmetries in Many-Body Systems’, *Phys. Rev. X* **5**, 011024 (2015).
- [183] G. Fox, R. Gupta, O. Martin and S. Otto, ‘Monte Carlo estimates of the mass gap of the O(2) and O(3) spin models in 1+1 dimensions’, *Nucl. Phys. B* **205**, 188 (1982).

- [184] K. C. Wang and C. J. Hamer, ‘Finite-size scaling studies of the O(2) Heisenberg spin model in (D+1) dimensions’, *J. Phys. A: Math. Gen.* **26**, 5713 (1993).
- [185] P. Weisz, ‘Computations of $M/\Lambda_{\overline{MS}}$ in the 2-d O(N) Non-Linear σ -Model’, *Commun. Math. Phys.* **219**, 45 (2001).
- [186] F. Alet and E. S. Sørensen, ‘Cluster Monte Carlo algorithm for the quantum rotor model’, *Phys. Rev. E* **67**, 015701 (2003).
- [187] F. Alet and E. S. Sørensen, ‘Directed geometrical worm algorithm applied to the quantum rotor model’, *Phys. Rev. E* **68**, 026702 (2003).
- [188] P. Hasenfratz, M. Maggiore and F. Niedermayer, ‘The exact mass gap of the O(3) and O(4) non-linear σ -models in $d = 2$ ’, *Phys. Lett. B* **245**, 522 (1990).
- [189] A. Milsted, ‘Matrix product states and the nonabelian rotor model’, (2015), arXiv:1507.06624.
- [190] J. Shigemitsu and J. B. Kogut, ‘A study of Λ parameters and crossover phenomena in $SU(N) \times SU(N)$ sigma models in two dimensions’, *Nucl. Phys. B* **190**, 365 (1981).
- [191] B. Gruber, L. C. Biedenharn and H. D. Döbner, *Symmetries in Science V: Algebraic Systems, Their Representations, Realizations, and Physical Applications* (Springer Science & Business Media, 6th Dec. 2012).
- [192] P. G. Hornby and M. N. Barber, ‘Perturbation series for the mass gap of the (1+1)-dimensional O(2)-model’, *J. Phys. A: Math. Gen.* **18**, 827 (1985).
- [193] P. Butera and M. Comi, ‘Quantitative study of the Kosterlitz-Thouless phase transition in an XY model of two-dimensional plane rotators: High-temperature expansions to order β^{20} ’, *Phys. Rev. B* **47**, 11969 (1993).
- [194] P. Butera and M. Comi, ‘Perturbative renormalization group, exact results, and high-temperature series to order 21 for the N-vector spin models on the square lattice’, *Phys. Rev. B* **54**, 15828 (1996).
- [195] H. H. Roomany and H. W. Wyld, ‘Finite-lattice approach to the O(2) and O(3) models in 1 + 1 dimensions and the (2+1)-dimensional Ising model’, *Phys. Rev. D* **21**, 3341 (1980).
- [196] C. R. Allton and C. J. Hamer, ‘The (1+1)D O(2) model: a finite lattice analysis’, *J. Phys. A: Math. Gen.* **21**, 2417 (1988).
- [197] J. B. Kogut, ‘The lattice gauge theory approach to quantum chromodynamics’, *Rev. Mod. Phys.* **55**, 775 (1983).
- [198] I. P. McCulloch and M. Gulácsi, ‘The non-Abelian density matrix renormalization group algorithm’, *Europhys. Lett.* **57**, 852 (2002).
- [199] S. Singh, R. N. C. Pfeifer and G. Vidal, ‘Tensor network decompositions in the presence of a global symmetry’, *Phys. Rev. A* **82**, 050301 (2010).
- [200] A. Weichselbaum, ‘Non-abelian symmetries in tensor networks: a quantum symmetry space approach’, *Ann. Phys.* **327**, 2972 (2012).

- [201] L. Vanderstraeten, F. Verstraete and J. Haegeman, ‘Scattering particles in quantum spin chains’, *Phys. Rev. B* **92**, 125136 (2015).
- [202] E. Brézin and J. Zinn-Justin, ‘Spontaneous breakdown of continuous symmetries near two dimensions’, *Phys. Rev. B* **14**, 3110 (1976).
- [203] M. Lubasch, J. I. Cirac and M.-C. Bañuls, ‘Algorithms for finite projected entangled pair states’, *Phys. Rev. B* **90**, 064425 (2014).
- [204] B. Douçot, L. B. Ioffe and J. Vidal, ‘Discrete non-Abelian gauge theories in Josephson-junction arrays and quantum computation’, *Phys. Rev. B* **69**, 214501 (2004).

Ashley Milsted

curriculum vitae

University education

- 2010–2012 **Master of Science in Physics**, *Leibniz University*, Hanover, Germany, 1.2.
- 2004–2007 **Bachelor of Science in Philosophy and Physics**, *Durham University*, Durham, England, *1st Class with Honours*.

Employment

Vocational

- 2012–present **Graduate student**, *Leibniz University*, Hanover, Germany.
- 2009–2012 **Research assistant**, *Inst. for Solar Energy Research*, Hameln, Germany, *isfh.de*.